Ph.D. Dissertation of Physics

Single-shot detection based multi-electron and nuclear spin manipulation in GaAs

단발 측정 기반 GaAs 다중 전자 및 핵 스핀 제어

February 2023

Graduate School of Natural Sciences
Seoul National University
Physics Major

Wonjin Jang

Single-shot detection based multi-electron and nuclear spin manipulation in GaAs

Advisor: Prof. Dohun Kim

Submitting a Ph.D. Dissertation of
Physics

February 2023

Graduate School of Natural Sciences
Seoul National University
Physics Major

Wonjin Jang

Confirming the Ph.D. Dissertation written by
Wonjin Jang
February 2023

Chair	________________________	(Seal)
Vice Chair	________________________	(Seal)
Examiner	________________________	(Seal)
Examiner	________________________	(Seal)
Examiner	________________________	(Seal)

Abstract

Quantum computers are expected to outperform classical computers in solving certain sets of problems such as factorizations, the travelling salesman problem, and searching algorithms. This is because quantum bits (qubits), the building blocks of the quantum computer, enable quantum superposition and entanglement that have no classical counterpart. To achieve reliable large-scale quantum computers in practice, various platforms based on superconducting circuits, trapped ions, and semiconductor quantum dots (QDs) have been investigated both theoretically and experimentally.

Demonstrating the quantum supremacy with the superconducting qubits, recent progresses on the quantum information processing are shown to be promising. The semiconductor QD spin qubits are also actively studied for advanced quantum information processing. Some of the advantages of QD-spin-qubit-based platforms include long-lattice-relaxation time, highly-dense integrability, and compatibility with CMOS fabrication processes. Based on these, high-fidelity single- and two-qubit operations along with quantum error correction have been demonstrated recently. Moreover, coherent manipulation of the spin qubits have also been performed at high-temperatures (> 1 K), alleviating the need for ultra-low temperature. This allows the integration of the classical electronics near the qubit chip and supports the scalability as a result.

Fluctuating nuclear spins in a host material pose a great threat to the coherence of electron spins in semiconductor QDs. At the same time, it is also possible to investigate the interaction of an electron spin with surrounding nuclear spins which is known as the central-spin problem. While high electron mobility ($> 10^6$ cm^{2}V^{-1}s^{-1}) and low effective electron mass of the two-dimensional electron gas in GaAs-based heterostructures allow for simple fabrication process, the non-zero nuclear spins of Ga and As limit the coherence of the electron spins present in the GaAs QDs. This thesis illustrates the manipulation of multi-electron and nuclear spins in GaAs and suggests possible routes toward high-fidelity quantum operations under noisy environments via passive and active noise mitigation.

Chapter 1 briefly introduces the basics of the quantum computation including the concept of qubits and GaAs QD-spin qubits. It also describes the details of measurement techniques including dc transport measurement of the QDs, and the radio-frequency (rf) based real-time charge sensing technique. The rf-charge sensing is essential for single-shot detection of quantum states described in the following chapters.

QD is a versatile platform for studying various types of spin qubits in semiconductors. Chapter 2 briefly describes different types of spin qubits such as single-electron spin qubit, two-electron singlet-triplet qubit and three-electron hybrid qubit. The advantages of the multi-electron spin qubits are mainly discussed in this chapter.

Chapter 3 discusses the operation of two-electron single-triplet qubits in double quantum dots (DQDs) based on energy-selective-tunneling (EST) single-shot readout. The EST readout enables high-fidelity detection of spin states (> 90 %) under a large-magnetic-field difference across the DQD (> 85 mT), where the difference is known to limit the lifetime of a singlet-triplet qubit at the Pauli spin blockade. The high-fidelity EST is further applied to single-shot-based estimation of Hamiltonian parameters for real-time-feedback-based coherence extension of the qubit which is discussed in Chapter 4.

Coherent manipulation of three-electron spins as well as the control of nuclear spins with the three-electron spin are discussed in Chapter 5 and 6. Strong Coulomb interaction between the electrons within a single QD facilitates the formation of a Wigner molecule, the strongly-correlated electronic ground state with a spatially localized orbital wavefunction. One of the consequences of the localization is quenched-orbital splitting which allows for the realization of a three-electron hybrid qubit in GaAs within the typical experimental bandwidth (Chapter 5). Furthermore, efficient dynamic nuclear polarization with the Wigner molecule is described in Chapter 6.

EST-based multi-electron qubit operations and the dynamic nuclear polarization scheme presented here can also be realized with other host materials including silicon and germanium, which is expected to further boost the overall qubit control fidelities. In Chapter 7, I summarize the main results and discuss possible applications of semiconductor QDs in advanced quantum information processing.

Keyword: Quantum Information, Semiconductor quantum dot, Spin qubit, Quantum control, Quantum computer

Student Number: 2017-28980

Table of Contents

Chapter 1. Introduction

1.1. Quantum Computation

Quantum computers may provide significant speed-ups for solving certain sets of problems including factorization, and traveling salesman problem, which have been assumed to be unsolvable within a finite timescale with the classical computers [1–3]. This is because the quantum superposition, and entanglement, which have no counterpart in the classical world, enable the quantum parallelism for processing multiple inputs simultaneously. To facilitate such parallelism the building blocks of the quantum computers, the qubits, are purely quantum objects. Naturally, the quantum computers can also offer efficient routes for the quantum simulations [3,4].

1.1.1 Qubit

The qubit serves as the basic unit for quantum information processing, which is analogous to the bit of the classical computers. The qubit is a quantum two-level system where the ground and excited states are encoded as 0, and 1. Due to the quantumness the qubits allow the quantum superposition, and entanglement which in turn enable the quantum parallelism [3].

A qubit state $|\psi\rangle$ can be represented by the linear combination of two orthogonal eigenstates $|0\rangle$ and $|1\rangle$.

$$|\psi\rangle = a_0|0\rangle + a_1|1\rangle \quad \text{(Eq. 1.1)}$$

Here, the complex coefficient a_i corresponds to the probability amplitude (i = 0, 1), where the norm of the a_i is the probability of the qubit to be at the state $|i\rangle$, P_i .

$$P_i = |a_i|^2 \qquad \text{(Eq. 1.2)}$$

In the ideal case without any leakage state, the P_i sum up to 1 which serves as the normalization condition.

Together with the normalization condition, because global phase of the probability amplitudes a_0 and a_1 does not affect the physical observables, the a_i can be characterized by two independent variables θ and ϕ as shown in Eq. 1.3.

$$a_0 = \sin\left(\frac{\theta}{2}\right) \ , \ a_1 = e^{i\phi}\cos\left(\frac{\theta}{2}\right) \qquad \text{(Eq. 1.3)}$$

This implies that a qubit state can be represented by a single point on a sphere, which is referred to as the Bloch sphere [3] as shown in Fig. 1.1.

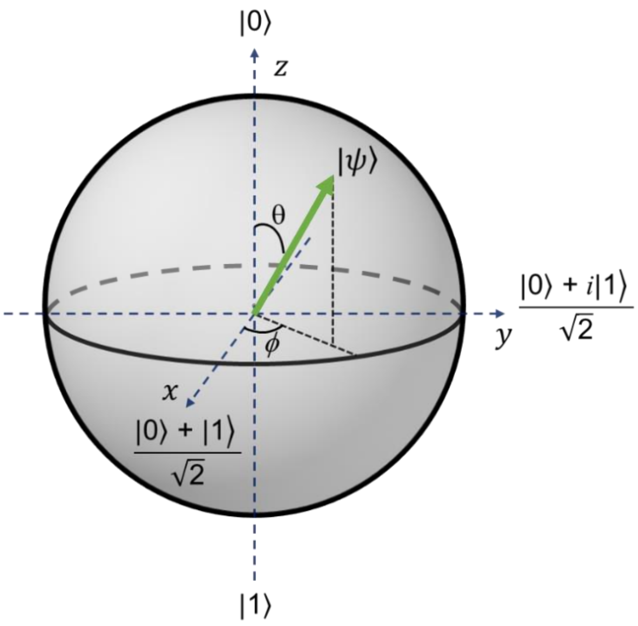

Figure 1.1: Qubit state on a Bloch sphere

For example, the $|0\rangle$ and $|1\rangle$ states sit on the north and south pole of the sphere respectively, where the eigenstates of the Pauli-x, σ_X (Pauli-y, σ_y) operator reside on the x- (y-) axis.

1.1.2 Decoherence

A pure quantum state can be described by a single state vector $|\psi\rangle$, which differs from the mere statistical mixture of certain states. For example, in a box one can prepare 100 electrons with spin $(|\uparrow\rangle + |\downarrow\rangle)/\sqrt{2}$ (+x axis on the Bloch sphere) which is an eigenstate of the σ_x operator, and in the other box, one can prepare random mixture of 50 spin $|\uparrow\rangle$ electrons, and 50 spin $|\downarrow\rangle$ electrons. While the average of the spin projection to z-axis in both boxes are equal to 0, there exist the qualitative difference between the two boxes. If we perform the famous Stern-Gerlach experiment with the measurement axis aligned to the x-axis, the 100 electrons in the former box would be projected to +1 states. However in case of the latter box, the projection would result in the random mixture of -1, and +1 states. The electron states in the former box are the pure states, whereas the electrons in the latter box are referred to as the mixed states. As can be inferred from the example, the purity of a quantum state is directly related to how much information is not lost about the state. Therefore, it is necessary for the qubits to be as ‘pure’ as possible to perform successful quantum computations.

Decoherence is the loss of purity, or the quantum coherence which is mainly caused by the interaction of the quantum state with the environment. While the interactions between the qubits and the surrounding systems are mandatory to enable quantum control, the interactions at the same time lead to decoherence inevitably.

The decoherence can be roughly categorized into the dephasing and lattice relaxation. The dephasing is the loss of the information about the quantum phase which is represented by ϕ in Fig. 1.1. This is mainly caused by the fluctuation of the qubit energy spacing because the change in the qubit energy splitting modulates the oscillating frequency of the quantum state about the z-axis on the Bloch sphere. The time scale which the dephasing takes place is called T_2^*. Secondly, the lattice relaxation is the relaxation of the qubit state from the excited state to the ground state where the characteristic time scale for the lattice relaxation time is often referred to as the T_1 time.

While the single quantum state vector is not capable of formulating the purity of the state, density matrix formalism can devise how pure the quantum state is. For instance, a superposition state $|\psi\rangle = (|\uparrow\rangle + |\downarrow\rangle)/\sqrt{2}$ can be expressed as following with the density matrix.

$$\rho_{\mathrm{pure}} = |\psi\rangle\langle\psi| = \frac{1}{2}\begin{bmatrix} 1 & 1 \\ 1 & 1 \end{bmatrix} \qquad \text{(Eq. 1.4)}$$

On the other hand, the completely mixed state of $|\uparrow\rangle$, and $|\downarrow\rangle$ can be expressed as following.

$$\rho_{\mathrm{mixed}} = \frac{1}{2}\rho_{\uparrow} + \frac{1}{2}\rho_{\downarrow} = \frac{1}{2}\begin{bmatrix} 1 & 0 \\ 0 & 1 \end{bmatrix} \qquad \text{(Eq. 1.5)}$$

The purity of a quantum state is represented by $\mathrm{tr}(\rho^2)$. The purity satisfies $1/d \leq \mathrm{tr}(\rho^2) \leq 1$, where d is the dimension of the Hilbert space. If the purity is 1, the quantum state is pure, and for mixed state the $\mathrm{tr}(\rho^2) < 1$, where the lower bound $1/d$ represents the completely mixed state. In the upper case, $\mathrm{tr}(\rho_{\mathrm{pure}}^2) = 1$, and $\mathrm{tr}(\rho_{\mathrm{mixed}}^2) = 1/2$. The details of the density matrix formalism including the time evolution, and the Lindblad equation which can describe the open system dynamics can be found in Ref. [3].

1.1.3 Quantum control

Precise quantum state control is required to realize the high-fidelity quantum gates for advanced quantum computations. This section describes the resonant ac-control of the qubits based on the rotating wave approximation.

The Hamiltonian of a simple two-level system can be represented by a Pauli-z operator.

$$H_0 = \frac{\varepsilon_0}{2}\sigma_Z \qquad \text{(Eq. 1.6)}$$

Here, the ground state and the excited state is assumed to have the energy $-\frac{\varepsilon_0}{2}$, and $+\frac{\varepsilon_0}{2}$ respectively. Note the overall shift in the energy of the ground and excited states only contributes to the global phase of the qubit, and thereby the above can represent all the quantum two-level systems without the loss of generality.

Recalling the Schrödinger equation, the quantum states acquire the phase proportional to its energy along time. This can be visualized by the rotation of a quantum state about the z-axis on the Bloch sphere with the angular frequency $\omega_0 = \varepsilon_0/\hbar$. The quantum states rotate about the eigen-axis on the Bloch sphere with the angular frequency defined by the eigen-energy difference.

Suppose a quantum state is initialized to $|0\rangle$ which corresponds to the north pole of the Bloch sphere. The $|0\rangle$ state then rotates about the z-axis with the angular frequency ω_0. Because the mere z-rotation cannot result in the finite population of $|1\rangle$, there must be other components that can generate the rotation about some other axis on the Bloch sphere. First assume that we introduce a small constant perturbative field Δ << ε_0 (it can be a small constant magnetic field if the qubit is encoded in the spin degree of freedom) about the x-axis in order to generate the x-rotation which can be written as below.

$$H = \frac{\varepsilon_0}{2}\sigma_Z + \Delta\sigma_X \quad \text{(Eq. 1.7)}$$

In this case, because the qubit state is continuously rotating about the z-axis, the perturbation is effectively cancelled out at the qubit's frame after the time-averaging. Thereby, constant perturbation cannot generate the rotation of the qubit state about some other axis.

Now suppose the perturbative field is also rotating about the z-axis with the angular frequency ω. Then the Hamiltonian is as follows. Here, the $\hbar = 1$ for simplicity, and $\omega_0 = \varepsilon_0$ holds.

$$H = \frac{\omega_0}{2}\sigma_Z + \Delta\,[\cos(\omega t)\,\sigma_X - \sin(\omega t)\sigma_Y] \quad \text{(Eq. 1.8)}$$

If we move onto the frame that is rotating with the angular frequency ω, the corresponding transformation matrix $U_{rf}(t)$ is as follows.

$$U_{rf}(t) = \int \frac{i\omega t}{2}\sigma_Z dt = \begin{bmatrix} e^{\frac{i\omega t}{2}} & 0 \\ 0 & e^{-\frac{i\omega t}{2}} \end{bmatrix} \quad \text{(Eq. 1.9)}$$

At the rotating frame, the Hamiltonian is transformed in according to the below formula.

$$H_{rf} = U_{rf}^{\dagger}(t) H U_{rf}(t) - i\dot{U}_{rf}^{\dagger}(t) U_{rf}(t) \quad \text{(Eq. 1.10)}$$

The transformation explicitly leads to

$$H_{rf} = (\omega_0 - \omega)\sigma_Z + \Delta\sigma_X \quad \text{(Eq. 1.11)}$$

It should be emphasized that if the $\omega = \omega_0$ holds (if the perturbation is oscillating resonant to the qubit splitting), H_{rf} is reduced to $\Delta\sigma_{\mathrm{X}}$, implying that the qubit state can now rotate about the x-axis in the rotating frame.

While it is complicated in practice to apply a circularly oscillating field for the qubit, a simple sinusoidal driving about a fixed direction can be enough for the qubit driving. This is called the rotating wave approximation. Because a simple sinusoidal function cos(ωt) can be described as the summation of $\mathrm{e}^{i\omega\mathrm{t}}$ and $\mathrm{e}^{-i\omega\mathrm{t}}$, which are the rotating and the counter-rotating term respectively, one can average out the counter-rotating terms. Assuming that a simple $\Delta\cos(\omega\mathrm{t})\sigma_{\mathrm{X}}$ field is applied with the same H_0, it can easily be shown with the Eq. 1.10 that the resulting Hamiltonian in the rotating frame is as follows.

$$H_{\mathrm{rf}} = (\omega_0 - \omega)\sigma_{\mathrm{Z}} + \frac{\Delta}{2}\sigma_X \qquad \text{(Eq. 1.12)}$$

1.2. Semiconductor Quantum Dots

Quantum dot (QD) is a 0-dimensional structure where the electrons or holes can be confined, and the semiconductor is one of the platforms to study various QD array structures [5–7]. The qubits can be defined by utilizing the various degrees of freedom of the particles confined in the QDs. While the large susceptibility of the QDs to the charge noise makes the charge qubit impractical for advanced quantum information processing protocols [8,9], semiconductor QDs provide a significant platform for the spin qubits owing to the extensive controllability, scalability, long lattice relaxation time and dephasing time [4,5,10,11].

1.2.1 Gate-defined Quantum Dots

There have been several approaches to define quantum dots in the semiconductor including gate-define (lateral) QDs, vertical QDs, and the nanowire QDs [5]. Among these, the gate-defined QD is a versatile platform to study various QD structures which is not only limited to the 1-dimensional QD arrays, but also the 2-dimensional QD arrays. Especially the 2-dimensional QD array can be beneficial for surface code based quantum error correction schemes [12]. Moreover, the gate-defined QD systems provide a wide range of control for the QD arrays such as the inter-dot tunnel coupling strengths, chemical potentials, and QD-reservoir tunnel coupling strengths.

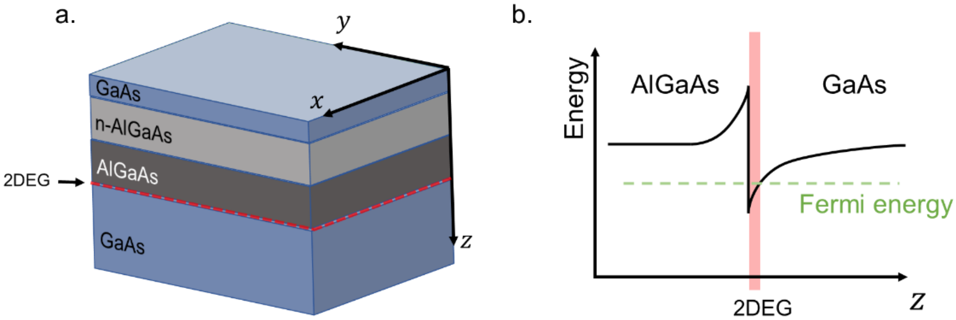

Figure 1.2: a. Schematic of the GaAs heterostructure for 2-dimensional electron gas (2DEG) formation. **b.** Conduction band energy diagram near the 2DEG.

To realize the gate-defined QDs in semiconductor, a substrate with two-dimensional electron (or hole) system is required. Possible candidates of such substrates include the simple silicon on insulator substrates [13], and certain types of semiconductor heterostructures which can host 2-dimensional electron gas (2DEG) or 2-dimensional hole gas (2DHG) at the interface [5,10]. This thesis will be mainly discussing the gate-defined QDs in 2DEG. Figure 1.2a shows the schematic of the

GaAs / AlGaAs heterostructure where the 2DEG resides at the interface of the GaAs and AlGaAs (red dashed line). Figure 1.2b is the conduction band energy diagram along the z-axis in Fig. 1.2a. The sharp band bending at the interface results in the narrow dip of the conduction band which is a quasi-two-dimensional quantum well. By engineering the Fermi level to reside above the dip, for example by adequate doping techniques, the quantum well can host the 2DEG.

By depositing metal gate structures as shown in Fig. 1.3a for example, and by applying negative voltages electrons underneath the gates can be depleted to form the QDs. Because the chemical potential of the QDs can be controlled via the gate voltages, the QDs can easily reach few electron regime by the electrical control. With the well-defined number of electrons, the various qubits can be implemented depending on the energy configurations, and the QD geometries [14–17]. Fig. 1.3b shows the scanning electron microscope (SEM) image of a GaAs QD device.

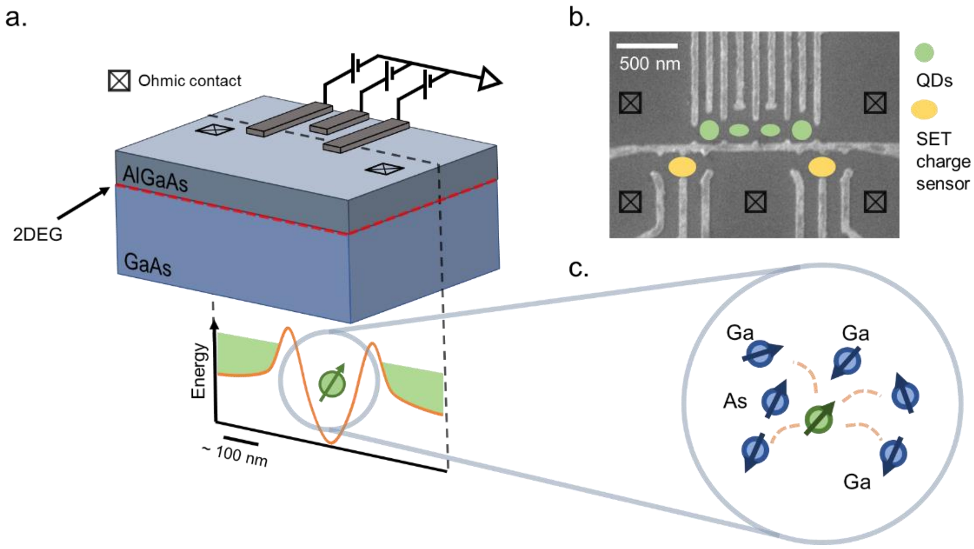

Figure 1.3: a. Schematic of a quantum dot device on a GaAs heterostructure. **b.** Scanning electron microscope (SEM) image of the gate structure. (Courtesy of

Jehyun Kim) **c.** Electron spin interacting with surrounding Ga and As nuclear spins.

1.2.2 GaAs Quantum Dots

As shown in the previous section, GaAs / AlGaAs is one of the heterosturctures that can host the 2DEG at the interface (Fig. 1.2). Based on the remarkable electron mobility, GaAs 2DEG has been widely exploited for various transport studies including the quantum hall measurements, and electron optics [18,19].

Small effective electron mass in GaAs alleviates the need for dense gate structures for QD formations, allowing a rather simple fabrication process [5,7]. Promoted by the simple fabrication and significant transport properties, initial studies on the QD qubits have been mostly demonstrated in GaAs [5]. However, because the electron in a GaAs QD is known to interact with ~ 10^6 surrounding Ga, and As nuclear spins (Fig. 1.2.2c), the fluctuations of the non-zero Ga and As nuclear spins pose a great threat to the coherence of the electron spin qubits [15]. Thereby, recent QD spin qubits are mainly studied in Si or Ge where the nuclear spin effect is not as significant [11,20].

Nonetheless, GaAs is still an interesting platform to study the interaction between a spin and the surrounding spin system which is known as the central-spin problem [21,22]. One of the applications of the central-spin problem is dynamic nuclear polarization where the electron spin is transferred to the nuclear spin to allow environmental field controls [23,24]. Furthermore because the nuclear spin fluctuation timescale is relatively slow, real-time Hamiltonian estimation based feedback loop control effectively eliminates the nuclear spin noise and allows highly coherent spin qubit operations [25]. Thereby, investigation of the spin qubits in GaAs may offer routes towards various noise mitigation techniques for high-fidelity quantum operations.

1.3 Electron Confinement in Quantum Dots

The number of electrons in the QDs must be well-defined to implement the desired qubit systems. This section introduces the signatures of the quantum dot formation which is related to the Coulomb blockade in cryogenic temperatures. Furthermore, I also describe measurement details required to reach the few electron regime, and to demonstrate real-time charge sensing.

1.3.1 Coulomb Blockade

The Coulomb repulsion between the electrons in a QD results in the energy cost for adding an extra electron to a QD, which is known as the charging energy (E_C, Fig. 1.4). If the energy scale of the charging energy is much larger than the thermal broadening of the electron reservoir, the electron number in the QD can be precisely defined. The number of electrons inside the QD, and thereby the chemical potential of the QD is tunable via the gate voltage, where the chemical potential has the linear dependence on the gate voltage [5]. As shown in the right panel in Fig. 1.4, if the chemical potential comes in between the Fermi level of the surrounding electron reservoir, the electron is allowed to freely tunnel across the QD to yield the finite current, and otherwise the current is blocked. Such is called the Coulomb blockade which is one signature of the QD formation. However, because the gate voltage also affects the tunneling barrier between the QD and the reservoir, as the gate voltage becomes more negative, the tunneling rate gets smaller. This implies the measurement of the current through the QD is challenging in the few electron regime, and calls for the charge sensing technique which is described below.

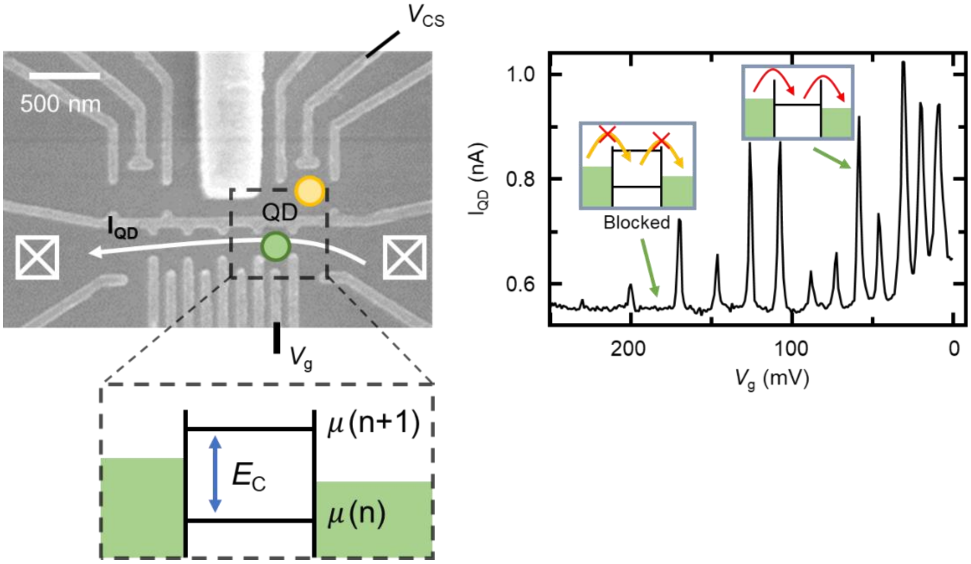

Figure 1.4: SEM image of a GaAs QD device with the QD energy schematic, and the corresponding Coulomb oscillation measured by the direct current through the QD.

1.3.2 Charge sensing

As mentioned in the previous section, the charge sensing technique is required to reach the few electron regime. In the SEM image shown in Fig. 1.4, the QD denoted in the yellow dot can function as a charge sensor. Due to the capacitive coupling between the yellow QD and the green QD, the conductance of the charge sensor QD can be modulated sensitively in according to the number of charges inside the green QD.

Figure 1.5a shows the Coulomb oscillation of the charge sensor QD, or the single-electron transistor (SET). If the V_{CS} is parked at the position with finite dI_{CS}/dV_{CS}, the change in the electron number inside the target QD can result in the modulation of the conductance. With the V_{CS} parked at the sensitive position (large dI_{CS}/dV_{CS}), the conductance is first modulated along the V_G because of the capacitive coupling between the V_G and the SET. However, when the electron tunnels out from the QD it effectively applies positive voltage to the SET, and there appear the kink in the conductance (Fig. 1.5b). By lowering the V_G until the kinks do not occur, one can fully deplete the QD and fill up the QD with the desired number of electrons by counting the kinks.

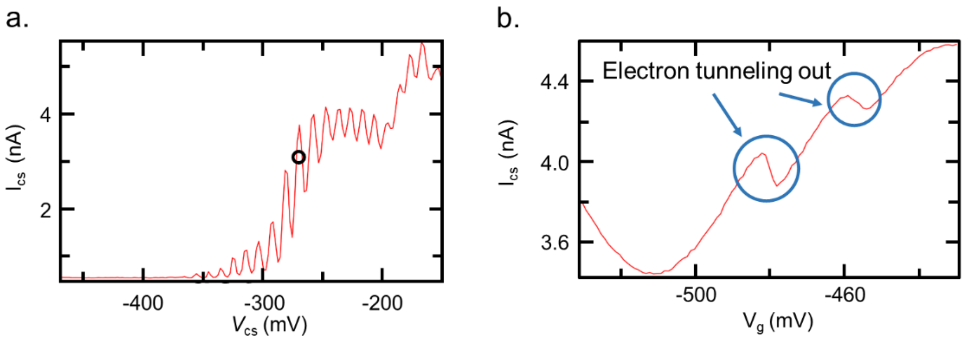

Figure 1.5: a. Coulomb oscillation of the charge sensor single-electron transistor **b.** Charge sensing signal.

Attaching a resonant LC circuit to the ohmic contact allows high-bandwidth rf charge sensing by the reduced $1/f$ noise [26]. The rf-reflectance of the circuit is modulated by the resistance (and thereby the conductance) of the sensor SET channel, the same charge sensing is possible with the rf. This further allows the real-time detection of the charge tunneling events which can be directly utilized for single-shot quantum state detection. For instance, when the chemical potential $\mu(n = 1)$ of a QD is tuned close to the Fermi level of the reservoir as shown in Fig. 1.6a, the last electron in the QD can tunnel in and out from the QD to reservoir due to the thermal tunneling events. Figure 1.6b. is showing the time-resolved measurement of the tunneling events via the rf-reflectometry with the measurement bandwidth > 1 MHz.

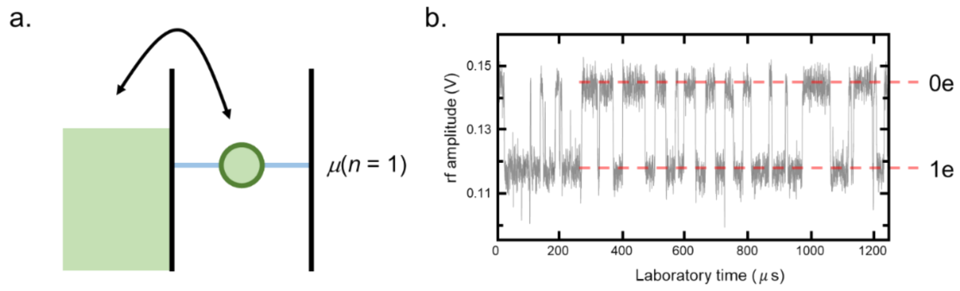

Figure 1.6: a. Schematic of the one electron tunneling in and out from the QD to the reservoir. **b.** Time-resolved measurement of the electron tunneling event with a rf charge sensor.

1.3.3 Charge stability diagram of a double quantum dot

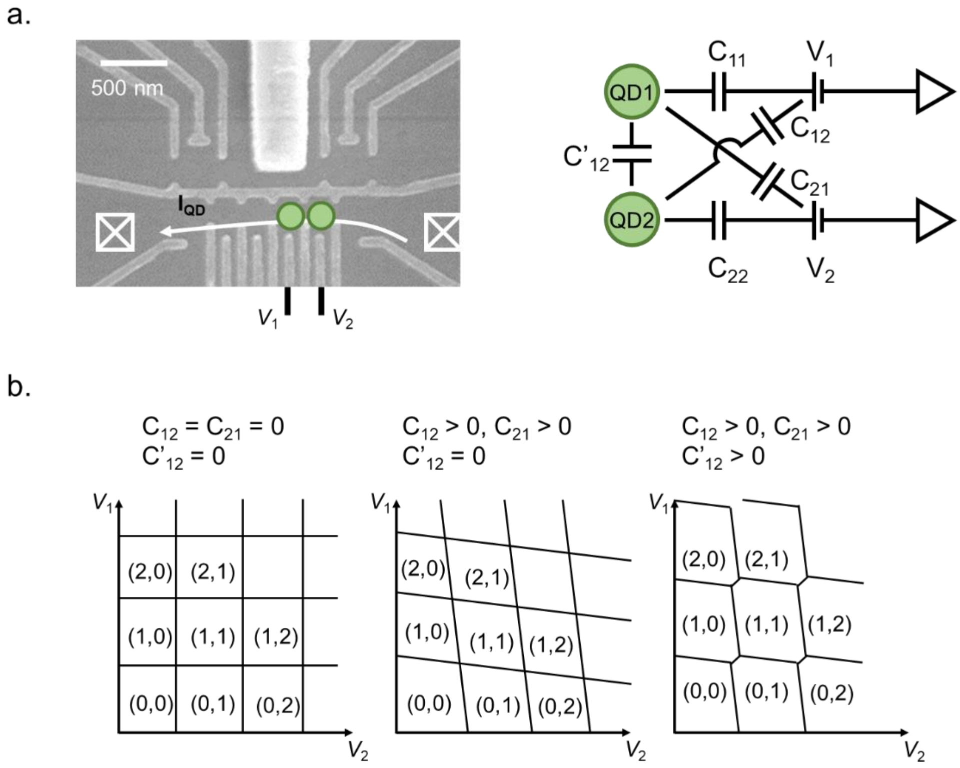

Figure 1.7: a. SEM image of a GaAs QD device. **b.** Schematic of the stability diagram of a DQD for different coupling strengths.

Assume two QDs labeled QD1 and QD2 are formed, where the chemical potential of the QDs are mainly controlled by V_1, and V_2 respectively (Fig. 1.7a). The current through the QDs, I_{QD}, as the function of V_1, and V_2 would resemble the checkerboard pattern as shown in the first panel in Fig. 1.7b. However, because the V_1 (V_2) capacitively couple not only with the QD1 (QD2) but also with QD2 (QD1) by C_{12} (C_{21}), the charging line of the QD1 (QD2) has finite slope about the V_2 (V_1) as shown in the second panel of Fig. 1.7b. Moreover, because the QD1, and QD2 are also coupled by the capacitive coupling (C'_{12}), the crossing between the charging lines becomes the anti-crossings and result in the honeycomb pattern as shown in the third panel of the Fig. 1.7b. Such plots are called the charge stability diagrams. Figure 1.8a is showing one example of the stability diagram where the current through the double QD (DQD) as the function of V_1, and V_2. Figure 1.8b is a stability diagram measured by the charge sensing technique near the single-electron regime. Such stability diagrams provide the information about the charge configuration of the multiple QD array, which serve as a basis for qubit operations.

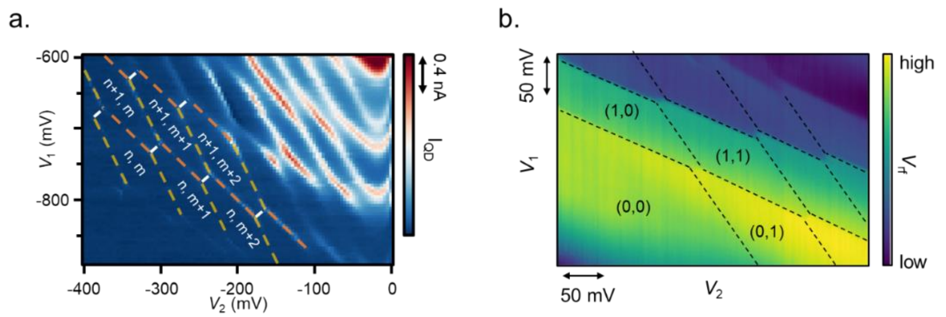

Figure 1.8: Stability diagram measured by **a.** the direct current through the double quantum dot and **b.** rf charge sensing.

References

[1] L. K. Grover, Quantum Mechanics Helps in Searching for a Needle in a Haystack, *Phys. Rev. Lett.* **79**, 325 (1997).

[2] P. Shor, Polynomial-Time Algorithms for Prime Factorization and Discrete Logarithms on a Quantum Computer, *SIAM Rev.* **41**, 303 (1999).

[3] M. A. Nielsen and I. L. Chuang, Quantum Computation and Quantum Information, 10th anniversary ed (Cambridge University Press, Cambridge ; New York, 2010).

[4] X. Xue, M. Russ, N. Samkharadze, B. Undseth, A. Sammak, G. Scappucci, and L. M. K. Vandersypen, Quantum Logic with Spin Qubits Crossing the Surface Code Threshold, *Nature* **601**, 7893 (2022).

[5] R. Hanson, L. P. Kouwenhoven, J. R. Petta, S. Tarucha, and L. M. K. Vandersypen, Spins in Few-Electron Quantum Dots, *Rev. Mod. Phys.* **79**, 1217 (2007).

[6] M. Seo, H. K. Choi, S.-Y. Lee, N. Kim, Y. Chung, H.-S. Sim, V. Umansky, and D. Mahalu, Charge Frustration in a Triangular Triple Quantum Dot, *Phys. Rev. Lett.* **110**, 046803 (2013).

[7] D. M. Zajac, T. M. Hazard, X. Mi, E. Nielsen, and J. R. Petta, Scalable Gate Architecture for a One-Dimensional Array of Semiconductor Spin Qubits, *Phys. Rev. Applied* **6**, 054013 (2016).

[8] D. Kim et al., Microwave-Driven Coherent Operation of a Semiconductor Quantum Dot Charge Qubit, *Nat. Nanotechnol.* **10**, 243 (2015).

[9] K. D. Petersson, J. R. Petta, H. Lu, and A. C. Gossard, Quantum Coherence in a One-Electron Semiconductor Charge Qubit, *Phys. Rev. Lett.* **105**, 246804 (2010).

[10] F. A. Zwanenburg, A. S. Dzurak, A. Morello, M. Y. Simmons, L. C. L.

Hollenberg, G. Klimeck, S. Rogge, S. N. Coppersmith, and M. A. Eriksson, Silicon Quantum Electronics, *Rev. Mod. Phys.* **85**, 961 (2013).

[11] J. Yoneda et al., A Quantum-Dot Spin Qubit with Coherence Limited by Charge Noise and Fidelity Higher than 99.9%, *Nat. Nanotechnol.* **13**, 102 (2018).

[12] A. G. Fowler, M. Mariantoni, J. M. Martinis, and A. N. Cleland, Surface Codes: Towards Practical Large-Scale Quantum Computation, *Phys. Rev. A* **86**, 032324 (2012).

[13] R. Maurand et al., A CMOS Silicon Spin Qubit, *Nat Commun.* **7**, 1 (2016).

[14] D. Loss and D. P. DiVincenzo, Quantum Computation with Quantum Dots, *Phys. Rev. A* **57**, 120 (1998).

[15] J. R. Petta, A. C. Johnson, J. M. Taylor, E. A. Laird, A. Yacoby, M. D. Lukin, C. M. Marcus, M. P. Hanson, and A. C. Gossard, Coherent Manipulation of Coupled Electron Spins in Semiconductor Quantum Dots, *Science* **309**, 2180 (2005).

[16] D. Kim et al., Quantum Control and Process Tomography of a Semiconductor Quantum Dot Hybrid Qubit, *Nature* **511**, 70 (2014).

[17] E. A. Laird, J. M. Taylor, D. P. DiVincenzo, C. M. Marcus, M. P. Hanson, and A. C. Gossard, Coherent Spin Manipulation in an Exchange-Only Qubit, *Phys. Rev. B* **82**, 075403 (2010).

[18] M. Carrega, L. Chirolli, S. Heun, and L. Sorba, Anyons in Quantum Hall Interferometry, *Nat. Rev. Phys.* **3**, 10 (2021).

[19] I. Neder, M. Heiblum, Y. Levinson, D. Mahalu, and V. Umansky, Unexpected Behavior in a Two-Path Electron Interferometer, *Phys. Rev. Lett.* **96**, 016804 (2006).

[20] N. W. Hendrickx, W. I. L. Lawrie, M. Russ, F. van Riggelen, S. L. de Snoo, R. N. Schouten, A. Sammak, G. Scappucci, and M. Veldhorst, A Four-Qubit

Germanium Quantum Processor, *Nature* **591**, 7851 (2021).

[21] J. H. Ardenkjær-Larsen, B. Fridlund, A. Gram, G. Hansson, L. Hansson, M. H. Lerche, R. Servin, M. Thaning, and K. Golman, Increase in Signal-to-Noise Ratio of > 10,000 Times in Liquid-State NMR, *Proc. Natl. Acad. Sci.* **100**, 10158 (2003).

[22] J. M. Nichol, S. P. Harvey, M. D. Shulman, A. Pal, V. Umansky, E. I. Rashba, B. I. Halperin, and A. Yacoby, Quenching of Dynamic Nuclear Polarization by Spin–Orbit Coupling in GaAs Quantum Dots, *Nat. Commun.* **6**, 1 (2015).

[23] J. R. Petta, J. M. Taylor, A. C. Johnson, A. Yacoby, M. D. Lukin, C. M. Marcus, M. P. Hanson, and A. C. Gossard, Dynamic Nuclear Polarization with Single Electron Spins, *Phys. Rev. Lett.* **100**, 067601 (2008).

[24] S. Foletti, H. Bluhm, D. Mahalu, V. Umansky, and A. Yacoby, Universal Quantum Control of Two-Electron Spin Quantum Bits Using Dynamic Nuclear Polarization, *Nat. Phys.* **5**, 903 (2009).

[25] M. D. Shulman, S. P. Harvey, J. M. Nichol, S. D. Bartlett, A. C. Doherty, V. Umansky, and A. Yacoby, Suppressing Qubit Dephasing Using Real-Time Hamiltonian Estimation, *Nat. Commun.* **5**, 5156 (2014).

[26] D. J. Reilly, C. M. Marcus, M. P. Hanson, and A. C. Gossard, Fast Single-Charge Sensing with a Rf Quantum Point Contact, *Appl. Phys. Lett.* **91**, 162101 (2007).

Chapter 2. Spin Qubits in Quantum Dots

Gate-defined semiconductor QD system is a versatile platform to study various types of spin qubits. Depending on the number of QDs, and on the number of the electrons (or holes) inside the QDs, different types of spin qubits can be defined. For instance, one electron inside a QD can define a simple Loss-DiVincenzo (LD) qubit where the qubit state is encoded in the spin-up, and spin-down subspace, and two-electron confined in a double QD (DQD) can define a singlet-triplet qubit where the qubit states are encoded in the spin-triplet zero (T_0), and spin-singlet (S) states. This section introduces several spin qubits in QD systems including the LD qubit, and multi-electron spin qubits.

2.1 Single-Electron Spin Qubit

First proposed by Loss and DiVincenzo [1], single-electron spin is the simplest form of the spin qubit feasible in QD systems. The single-electron spin qubit, or the LD qubit can be formed by confining an electron in a single QD. Because the electron is a spin-1/2 particle, the spin $|\uparrow\rangle$ and $|\downarrow\rangle$ states of the electron naturally form a quantum two-level system. Also, it should be emphasized the LD qubit is the only qubit that requires a single QD for the qubit operation, which can be beneficial at the scalability aspect.

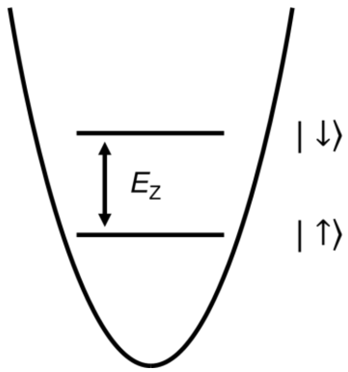

Figure 2.1: Schematic of the Zeeman split single-electron spin qubit in a QD.

The qubit energy splitting of the LD qubit can be given by the Zeeman splitting from an external magnetic field, B_{ext}. Explicitly, the energy of the $|\uparrow\rangle$ ($|\downarrow\rangle$) is $\frac{1}{2}g^*\mu_B B_{ext}$ ($-\frac{1}{2}g^*\mu_B B_{ext}$), where the resulting qubit splitting is $g^*\mu_B B_{ext}$. Here g^* is the Lande-g factor dependent on the materials, and μ_B is the Bohr magneton. Assuming the external field direction as the z-axis, an oscillating magnetic field transverse to the z-axis can drive the qubit state if the driving frequency is resonant to the qubit splitting.

One of the ways to implement the resonant driving is to apply an ac-current through a transmission line near the LD qubit which in turn generates the oscillating magnetic field [2]. However, fabrication of the transmission lines for sizable driving field strength is challenging which calls for alternative single-spin control techniques.

Micromagnet can generate slanting field for coherent single-spin manipulations [3,4]. Figure 2.2a shows an example of the QD device with the micromagnet, and Fig. 2.2b shows the schematic of the magnetic field along the direction shown in Fig. 2.2a. By applying the oscillating electric field to the gate (Fig. 2.2b), the electron wavefunction is expected to spatially oscillate. As a result, the electron experiences the oscillating field about the axis transverse to the quantization axis (z-axis) and allows the coherent qubit manipulations. Previous works have shown > 10 MHz Rabi frequency is achievable in Si with the well-designed micromagnet, where the micromagnet also generates spatial magnetic field gradient for individual qubit addressing [3,5,6].

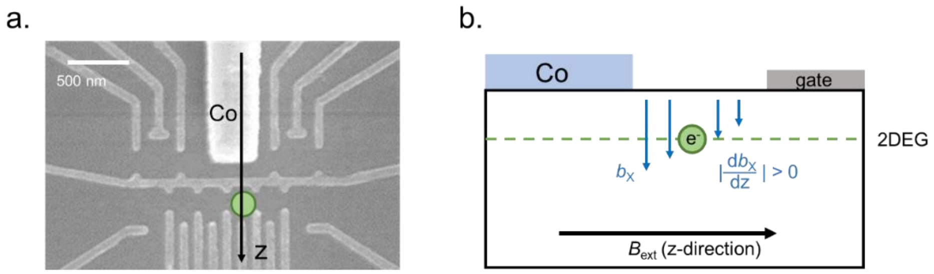

Figure 2.2: **a.** A GaAs QD device with a Co micromagnet. **b.** Schematic of the micromagnet integrated QD device along the line-cut shown in the black arrow in **a.**

2.2 Two-Electron Spin Qubit

Two spin-1/2 particles construct 4 different spin states. The 4 spin states can be categorized into the singlet (s = 0) and triplet state (s = 1), where the triplet state can be further sorted in to T+ (m = 1), T_0 (m = 0) and T- (m = -1). Here, s is the spin quantum number, and m is their projection onto the z-axis which is also referred to as the spin magnetic quantum number.

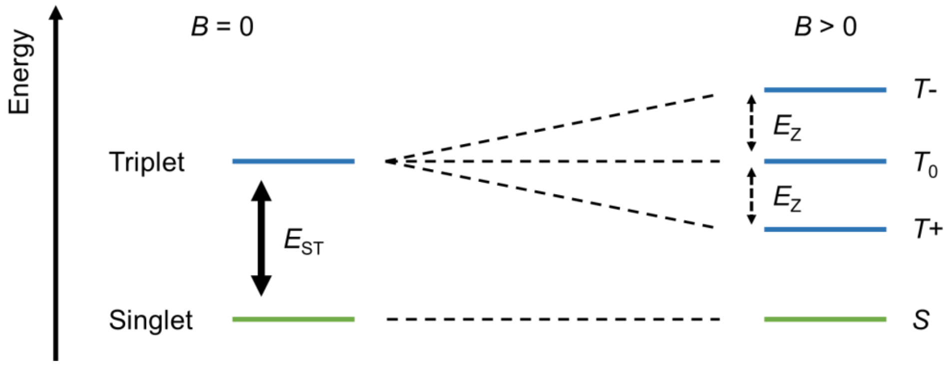

Figure 2.3: Two-electron spin states with and without the magnetic field.

Figure 2.4 shows the energy diagram of the two-electrons confined in a DQD as a function of the voltage detuning ε. Two electrons occupy the (2,0) [(1,1)] charge configuration at the negative [positive] ε. Throughout the thesis, n_1 (n_2) denotes the number electrons in the first (second) QD by the (n_1, n_2) charge configuration. When two electrons occupy the same QD, the eigenstates of the two-electron system becomes the singlet and triplet states due to the strong exchange interaction between the electrons [7,8]. The energy spacing between the singlet and the triplet branch, the singlet-triplet splitting, is described by the orbital splitting in GaAs which is typically on the order of $10^1 \sim 10^2\ h \cdot$ GHz (h is the Planck constant.). On the other hand, when the two electrons are at the (1, 1) charge configuration with the negligible exchange interaction, the eigenstates become the simple product state of two individual spin states,$|\uparrow, \uparrow\rangle$, $|\uparrow, \downarrow\rangle$, $|\downarrow, \uparrow\rangle$, and $|\downarrow, \downarrow\rangle$. While the full 4 different spin states comprise the full subspace for the two-qubit operations with the LD qubits, this section will be focusing on the $m = 0$ subspace formed by $|\uparrow, \downarrow\rangle$ and $|\downarrow, \uparrow\rangle$.

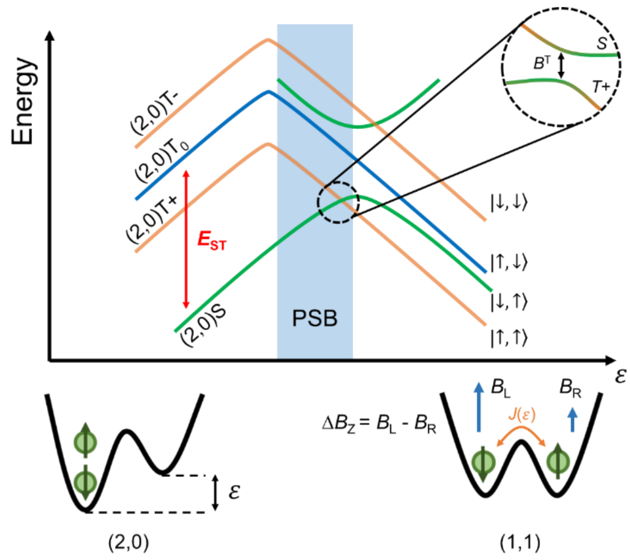

Figure 2.4: Energy diagram of the two-electrons in a double quantum dot

The m = 0 subspace of the two-electron spin states is a quantum two-level system which is commonly referred to as the singlet-triplet (ST_0) qubit [7,9]. By the electrical control of ε (Fig. 2.4), one can freely manipulate the charge state from (2,0) to (1,1). Because the spin singlet state is the ground state at the (2,0) the spin state can be initialized to the (2,0)S by the relaxation or electron exchange with the reservoir [9–11].

The quantum control of the ST_0 qubit is possible at the (1, 1) configuration. When the electrons are separated into different QDs, the electrons may experience the different Zeeman splitting, quantified by the ΔB_Z, due to the spatial g-factor difference [12], nuclear field difference [7,9], or the micromagnet [13]. The magnetic field difference ΔB_Z governs the energy splitting between |↑, ↓⟩ and |↓, ↑⟩ in the deep positive detuning, and the charge hybridization between the (2,0) and (1,1) near the 0 detuning results in the sizable exchange interaction $J(\varepsilon)$. Thereby, the Hamiltonian of the ST_0 qubit can be written as follows with the ordered basis $\{T_0, S\}$.

$$H = J(\varepsilon)\,(\mathbb{I} + \sigma_z)/2 + \Delta B_Z\,\sigma_x = \begin{bmatrix} J(\varepsilon) & \Delta B_z \\ \Delta B_z & 0 \end{bmatrix} \quad \text{(Eq. 2.1)}$$

If the initialized (2,0)S state is brought diabatically (diabatic with respect to the qubit splitting, but adiabatic about the tunnel coupling) to the (1,1) charge detuning, the spin state is kept at the singlet state during the diabatic passage. However, because the eigenstate is $|\uparrow, \downarrow\rangle$, and $|\downarrow, \uparrow\rangle$ in the (1,1) which is the x-axis of the Bloch sphere made of S, and T_0 qubit states, the singlet state can rotate about the x-axis with the oscillation frequency determined by ΔB_Z [7,9,10].

Also, the ST_0 qubit can be driven with the ac control as in the single electron case. Adiabatically bringing the (2,0)S state to the (1,1) regime initializes the qubit state to one of the $|\uparrow, \downarrow\rangle$, and $|\downarrow, \uparrow\rangle$ states depending on the sign of the ΔB_Z. Under such circumstance, if the $J(\varepsilon)$ oscillates resonant to the qubit splitting ΔB_Z by the means of the ε oscillation the qubit can be resonantly driven [14,15].

As described above, the ST_0 qubit can be operated in the (1, 1) charge configuration under the finite magnetic field difference across the DQD. After the qubit manipulation, the states can be detected with the charge sensor after adequate spin-to-charge conversion methods. Pauli-spin blockade (PSB) is one of the techniques to convert the spin state to the charge state. The blue box in Fig. 2.4 is the energy detuning where the PSB can occur. Here, the singlet-state can occupy the (2,0) charge state whereas the triplet can only occupy (1,1) charge state because of the Pauli exclusion principle. The resultant charge difference can be detected with the charge sensor. Various spin-to-charge conversion methods are also introduced in the Chapter 3 along with the emphasis on the energy-selective tunneling (EST) readout.

2.3 Three-Electron Spin Qubit

There are 8 possible spin states formed by the three spin-1/2 particles. In according to their spin quantum number, the states are grouped into quadruplet (s = 3/2), and doublet (s = 1/2) states. The quadruplet states are further sorted into m = -3/2, m = -1/2, m = 1/2 and m = 3/2 states, where the doublet states are sorted into the doublet triplet (D_T) and doublet singlet (D_S) states with m = 1/2 and m = -1/2.

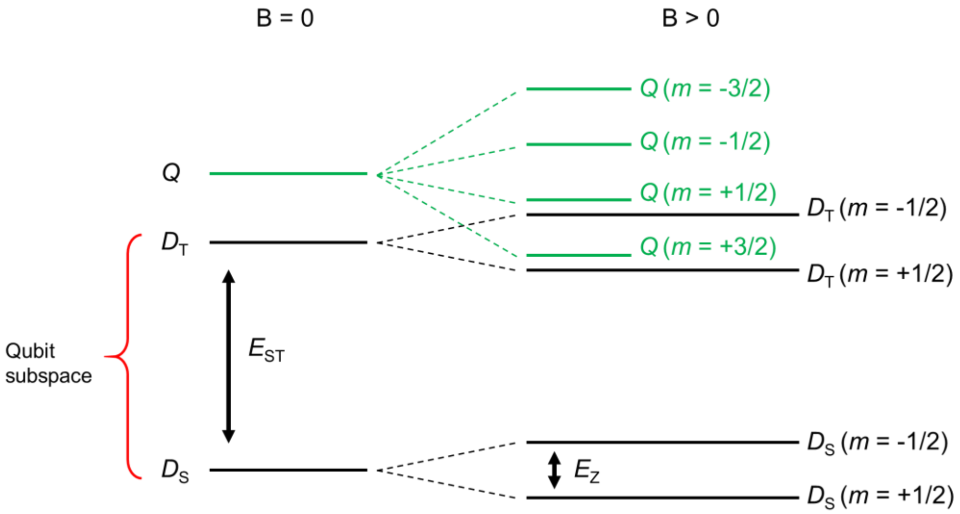

Figure 2.5: Three-electron spin states with and without the magnetic field.

Among the above 8 possible spin states, the D_S and D_T subspace are utilized to encode the three-electron spin qubit. While both the D_S, and D_T states have the spin degeneracy of 2 and result in the 4-dimensional subspace, because both m = 1/2 and m = -1/2 subspaces have the same dynamics for the doublet states and also because the m = 1/2 and m = -1/2 subspace does not couple with each other (in the ideal case), the D_S and D_T subspace can be regarded as a qubit subspace [16]. There are two types of the three-electron spin qubit encoded in the D_S and D_T subspace which are namely the exchange-only qubit, and the hybrid qubit. The exchange-only qubit is defined in a triple quantum dot with three electrons in the (1,1,1) configuration, whereas the hybrid qubit is encoded in the three electron spin state in a DQD. This section will only be describing the hybrid qubit, where the dynamics of the exchange-only qubit is very similar to that of the hybrid qubit [17,18].

As shown in Fig. 2.6, when the three-electrons are at the (2,1) charge configuration, the single electron in the right QD interact with both the ground and excited orbitals in the left QD via the exchange interactions, $J_1(\varepsilon)$ and $J_2(\varepsilon)$. While there exist no direct coupling between the ground (D_S) and excited (D_T) orbital state in the left QD, the exchange interactions $J_1(\varepsilon)$ and $J_2(\varepsilon)$ can mediate the exchange coupling $J_{12}(\varepsilon)$ (between the ground and the excited state. The detailed mathematical description based on the Schrieffer-Wolff transformation can be found in the Ref. [16].

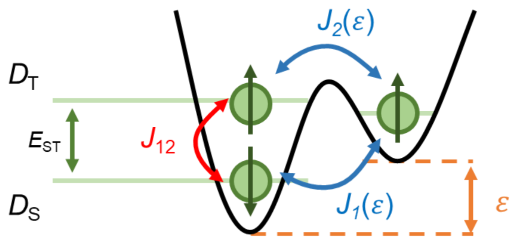

Figure 2.6: Schematic of the three-electron hybrid qubit in a DQD in (2,1) charge configuration

It should be emphasized the while the qubit states are encoded in the spin states in the three-electron hybrid qubit, the manipulation of the qubit does not require any magnetic field at all. The hybrid qubit does not call for micromagnets, striplines or external magnetic field, and the control is possible solely by the electrical means. This is where the name *hybrid* qubit comes from. The spin states couple with the electric field similar to the charge qubits. Even though the gate operation per dephasing time, quantified by T_π/T_2^* (T_π is the time required to realize the X_π gate) is consistent with the other types of qubits, the hybrid qubit can offer a longer dephasing time than the typical charge qubits, and faster manipulation speed compared to typical spin qubits. Because of the electrical controllability without any magnetic components, the hybrid qubit is directly compatible with the superconducting circuits for long range interactions [19] and the CMOS fabrication techniques well-established to date [20]. Details of the hybrid qubit control and readout are shown in Chapter 5.

References

[1] D. Loss and D. P. DiVincenzo, Quantum Computation with Quantum Dots, *Phys. Rev. A* **57**, 120 (1998).

[2] J. J. Pla, K. Y. Tan, J. P. Dehollain, W. H. Lim, J. J. L. Morton, D. N. Jamieson, A. S. Dzurak, and A. Morello, A Single-Atom Electron Spin Qubit in Silicon, *Nature* **489**, 541 (2012).

[3] J. Yoneda et al., Robust Micromagnet Design for Fast Electrical Manipulations of Single Spins in Quantum Dots, *Appl. Phys. Express* **8**, 084401 (2015).

[4] J. Yoneda et al., A Quantum-Dot Spin Qubit with Coherence Limited by Charge Noise and Fidelity Higher than 99.9%, *Nat. Nanotechnol.* **13**, 102 (2018).

[5] A. J. Sigillito, J. C. Loy, D. M. Zajac, M. J. Gullans, L. F. Edge, and J. R. Petta, Site-Selective Quantum Control in an Isotopically Enriched Si 28 / Si 0.7 Ge 0.3 Quadruple Quantum Dot, *Phys. Rev. Applied* **11**, 061006 (2019).

[6] D. M. Zajac, A. J. Sigillito, M. Russ, F. Borjans, J. M. Taylor, G. Burkard, and J. R. Petta, Resonantly Driven CNOT Gate for Electron Spins, *Science* **359**, 439 (2018).

[7] J. R. Petta, A. C. Johnson, J. M. Taylor, E. A. Laird, A. Yacoby, M. D. Lukin, C. M. Marcus, M. P. Hanson, and A. C. Gossard, Coherent Manipulation of Coupled Electron Spins in Semiconductor Quantum Dots, *Science* **309**, 2180 (2005).

[8] R. Hanson, L. P. Kouwenhoven, J. R. Petta, S. Tarucha, and L. M. K. Vandersypen, Spins in Few-Electron Quantum Dots, *Rev. Mod. Phys.* **79**, 1217 (2007).

[9] S. Foletti, H. Bluhm, D. Mahalu, V. Umansky, and A. Yacoby, Universal Quantum Control of Two-Electron Spin Quantum Bits Using Dynamic Nuclear Polarization, *Nat. Phys.* **5**, 903 (2009).

[10] W. Jang, J. Kim, M.-K. Cho, H. Chung, S. Park, J. Eom, V. Umansky, Y. Chung,

and D. Kim, Robust Energy-Selective Tunneling Readout of Singlet-Triplet Qubits under Large Magnetic Field Gradient, *npj Quantum Inf.* **6**, 64 (2020).

[11] T. Botzem et al., Tuning Methods for Semiconductor Spin Qubits, *Phys. Rev. Applied* **10**, 054026 (2018).

[12] D. Jirovec et al., A Singlet-Triplet Hole Spin Qubit in Planar Ge, *Nat. Mater.* **20**, 8 (2021).

[13] W. Jang, M.-K. Cho, J. Kim, H. Chung, V. Umansky, and D. Kim, Individual Two-Axis Control of Three Singlet-Triplet Qubits in a Micromagnet Integrated Quantum Dot Array, *Appl. Phys. Lett.* **117**, 234001 (2020).

[14] J. M. Nichol, L. A. Orona, S. P. Harvey, S. Fallahi, G. C. Gardner, M. J. Manfra, and A. Yacoby, High-Fidelity Entangling Gate for Double-Quantum-Dot Spin Qubits, *npj Quantum Inf.* **3**, 3 (2017).

[15] J. Kim et al., Approaching Ideal Visibility in Singlet-Triplet Qubit Operations Using Energy-Selective Tunneling-Based Hamiltonian Estimation, *Phys. Rev. Lett.* **129**, 040501 (2022).

[16] Z. Shi et al., Fast Hybrid Silicon Double-Quantum-Dot Qubit, *Phys. Rev. Lett.* **108**, 140503 (2012).

[17] E. A. Laird, J. M. Taylor, D. P. DiVincenzo, C. M. Marcus, M. P. Hanson, and A. C. Gossard, Coherent Spin Manipulation in an Exchange-Only Qubit, *Phys. Rev. B* **82**, 075403 (2010).

[18] J. Medford, J. Beil, J. M. Taylor, S. D. Bartlett, A. C. Doherty, E. I. Rashba, D. P. DiVincenzo, H. Lu, A. C. Gossard, and C. M. Marcus, Self-Consistent Measurement and State Tomography of an Exchange-Only Spin Qubit, *Nat. Nanotechnol.* **8**, 654 (2013).

[19] P. Harvey-Collard, J. Dijkema, G. Zheng, A. Sammak, G. Scappucci, and L. M. K. Vandersypen, Coherent Spin-Spin Coupling Mediated by Virtual Microwave Photons, *Phys. Rev. X* **12**, 021026 (2022).

[20] R. Maurand et al., A CMOS Silicon Spin Qubit, *Nat Commun* **7**, 1 (2016).

Chapter 3. Robust energy selective tunneling readout of singlet triplet qubits under large magnetic field gradient

Abstract

Fast and high-fidelity quantum state detection is essential for building robust spin-based quantum information processing platforms in semiconductors. The Pauli spin blockade (PSB)-based spin-to-charge conversion and its variants are widely used for the spin state discrimination of two-electron singlet–triplet (ST_0) qubits; however, the single-shot measurement fidelity is limited by either the low signal contrast, or the short lifetime of the triplet state at the PSB energy detuning, especially due to strong mixing with singlet states at large magnetic field gradients. Ultimately, the limited single-shot measurement fidelity leads to low visibility of quantum operations. Here, we demonstrate an alternative method to achieve spin-to-charge conversion of ST_0 qubit states using energy selective tunneling between doubly occupied quantum dots (QDs) and electron reservoirs. We demonstrate a single-shot measurement fidelity of 90% and an S–T_0 oscillation visibility of 81% at a field gradient of 100 mT (~ 500 MHz$\cdot$h$\cdot$($g^*\mu_B$)$^{-1}$); this allows single-shot readout with full electron charge signal contrast and, at the same time, long and tunable measurement time with negligible effect of relaxation even at strong magnetic field

---

This chapter is adapted from *npj Quantum Information* **6**, 64 (2020).

gradients. Using an rf-sensor positioned opposite to the QD array, we apply this method to two ST_0 qubits and show high-visibility readout of two individual single-qubit gate operations is possible with a single rf single-electron transistor sensor. We expect our measurement scheme for two-electron spin states can be applied to various hosting materials and provides a simplified and complementary route for multiple qubit state detection with high accuracy in QD-based quantum computing platforms.

Introduction

The assessment of general quantum information processing performance can be divided into that of state initialization, manipulation, and measurement. Rapid progress has been made in semiconductor quantum dot (QD) platforms, with independent demonstrations of, for example, high-fidelity state initialization of single and double QD spin qubits [1–3], high-fidelity quantum control with resonant microwaves [4–8] and non-adiabatic pulses [1,9,10], and high-fidelity state measurements using spin-to-charge conversion [3,11–19]. However, the high visibility of a quantum operation requires high fidelity in all stages of the quantum algorithm execution, which has been demonstrated in only a few types of spin qubits so far [4,6,7,10,20,21].

For double QD two-electron spin qubits, the Pauli spin blockade (PSB) phenomenon is typically used for discriminating spin-singlet (S) and -triplet (T_0) states where different spin states are mapped according to the difference in the relative charge occupation of two electrons inside the double QD, which is detected by a nearby electrometer [22–24]. As the spin-dependent signal deterministically appear at the measurement phase defined by the pulse sequence at the PSB, the measurement window can be shortened to the limit which allows enough signal to noise ratio (SNR) to discriminate the different spin signal [13], and such can lead to high measurement bandwidth. However, depending on the device design, the signal contrast can be small compared to the signal of one electron, especially when the charge sensor position in the device is not aligned with the QD axis. This issue is particularly problematic in recent multiple QD designs [25–29], where the charge sensor positioned opposite to the qubit array increases the range of QDs detectable by one sensor, but renders sensitive measurement of the relative electron position between nearest-neighbor QDs difficult.

Moreover, the spatial magnetic field difference $\Delta B_{//} = |B_{L//} - B_{R//}|$, where the $B_{L//}$ ($B_{R//}$) denotes the magnetic field strength parallel to the spin quantization axis at the left (right) dot, provides relaxation pathways through (1,1)T_0–(1,1)S mixing and rapid (1,1)S to (2,0)S tunneling in the PSB region as shown in the solid green regions in Fig. 3.1a, and normal PSB readout is difficult under large $\Delta B_{//}$. For example when $\Delta B_{//} > 200\ \mathrm{MHz}\cdot h\cdot(g^{*}\mu_B)^{-1}$, where h is the Planck's constant, g^* is the electron g-factor in GaAs, and μ_B is the Bohr magneton, the fast spin relaxation is known to lead to vanishing oscillation visibility [30]. As most QD spin qubit platforms utilize sizeable intrinsic [2,31,32] or extrinsic [33] $\Delta B_{//}$ to realize individual qubit addressing and high-fidelity single- and two-qubit operations [4,6,34,35], it is important to develop fast readout techniques that enable high-fidelity spin detection even at large $\Delta B_{//}$. So far, visibility higher than 95% using PSB readout can be achieved only for small $\Delta B_{//}$ despite the method's high measurement bandwidth [13,18].

These limitations of conventional PSB readout have been addressed in previous works, and several variants of the PSB readout have been developed for various QD systems [14–17]. In the latched readout scheme [14], the lack of the reservoir on one side of the double QD enables spin conversion to the (1,0) or (2,1) charge state, enhancing the signal contrast. In Ref [15], singlet–triplet (ST_0) qubit readout was performed in a triple QD to isolate the middle QD from the reservoirs, and the qubit state conversion to a metastable charge state enabled robust, high-fidelity qubit readout. While these techniques enhance the signal contrast to the full electron charge, the explicit demonstration of such methods combined with high-fidelity operation under large $\Delta B_{//}$ (> 200 MHz$\cdot h \cdot (g^{*}\mu_{\mathrm{B}})^{-1}$) has not been reported to date. We stress that it is unclear whether the readout near the (2,1) charge transition [15,17] will not suffer from the fast T_0 relaxation if the spin mixing rate due to $\Delta B_{//}$ is comparable to the (1,1)T_0 – (2,1) tunneling rate. We note here that unlike the readout methods near the (2,1) charge transition [15,17], T_0 relaxation pathway is inherently absent at the readout position of this work, as both the S and T_0 state occupy the (2,0) charge state as we describe below in detail. On the other hand, Orona, L. A. et al.[16] reported the shelving readout technique, whereby one of the qubit states is first converted to the T_+ state through fast electron exchange with the reservoir to prevent mixing with the (1,1)S state, enabling high-visibility readout of the ST_0 spin qubit. They showed explicitly that single-shot readout is possible even for $\Delta B_{//}$ ~ 180 mT (~ 900 MHz$\cdot h\cdot(g^*\mu_B)^{-1}$) by optimizing the shelving pulse sequence. However, the technique relies on PSB for final spin-to-charge conversion and is expected to be effective only when the charge sensor is sensitive to the relative position of electrons in the double QD.

Here, we demonstrate the energy selective tunneling (EST) readout, commonly called Elzerman readout [11], of ST_0 qubits under large $\Delta B_{//}$, accomplishing both signal enhancement, due to one electron tunneling, and long measurement time, enabling a robust single-shot readout. Unlike previous works, which demonstrated independent enhancement of the signal contrast and measurement time through intermediate spin or charge state conversion steps, our scheme does not require additional state conversion during the readout. Using large voltage modulation by rapid pulsing with ε ranging from the PSB-lifted (2,0) to the deep (1,1) charge regions, where the exchange coupling $J(\varepsilon)$ is turned off, we explicitly demonstrate a single-shot measurement fidelity of 90±1.3 % and an S–T_0 oscillation visibility of 81% at $\Delta B_{//}$ ~ 100 mT, corresponding to an oscillation frequency of 500 MHz. Furthermore, we demonstrate the detection of coherent operation of two individual ST_0 qubits in a quadruple QD array with a single rf-reflectometry line. We stress that we combine previous methods which individually demonstrated the Elzerman readout of the two electron spin states [12], large $\Delta B_{//}$ generation with micromagnet [33], high fidelity control of the ST_0 qubit [36], and robust measurement within a single quantum processor yielding a record high quantum oscillation visibility in large $\Delta B_{//}$. We also note that this is achieved at the expense of high bandwidth of PSB readout due to EST readout's intrinsic timing uncertainty in tunneling events. However the achieved measurement time on the order of 100 μs in this work using EST readout is still useful for future application to fast spin state readout, for example single-shot readout-based Bayesian estimation [37]. In this paper, we describe the proposed EST readout method in detail, compare it with the conventional PSB readout, and suggest possible routes for its further optimization.

Results

Energy selective tunneling readout

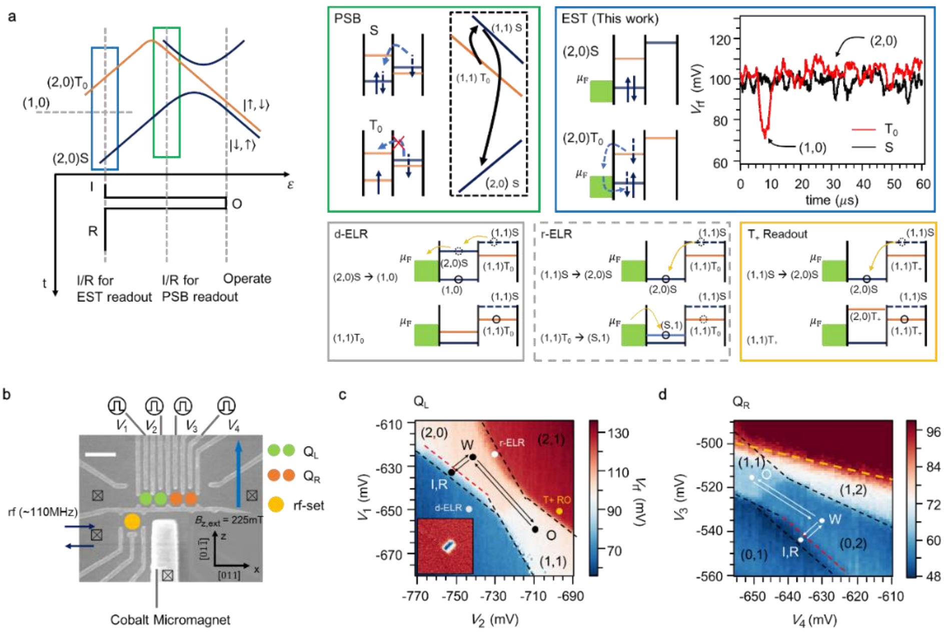

Figure 3.1 Energy levels and device platform a. Schematic of the singlet–triplet (ST_0) qubit energy levels as a function of detuning ε with energy selective tunneling (EST, blue boxes)- and Pauli spin blockade (PSB, green boxes)-based readout schemes. Green panel: At the PSB readout point, the (1,1)S state tunnels into the (2,0) charge state while the tunneling from the (1,1)T_0 state is blocked. The relative charge position is observed to determine the qubit state. Finite magnetic field difference $\Delta B_{//}$ provides a relaxation pathway for the (1,1)T_0 state. Blue panel: The Fermi level resides between the (2,0)S and (2,0)T_0 states, which enables EST. The

triplet state (red) tunnels out to the (1,0) and initializes to the (2,0)S, while no tunneling occurs for the S state. For comparison, three other types of modified PSB readout scheme are presented. Grey panel: In the direct enhanced latched readout (d-ELR) scheme, the (2,0)S state tunnels out to (1,0) while the spin-blockaded (1,1)T_0 state cannot tunnel out [14]. Dashed grey panel: At the reverse ELR (r-ELR) point, an electron tunnels into the spin-blockaded T_0 state to form the (S,1) while the S state stays at the (2,0) [14,15,17]. Yellow panel: In the T_+ readout scheme [16], one of the qubit states is conversed into the T_+ state to prevent the relaxation in the PSB. The readout is taken in the PSB by discriminating the (2,0)S and (1,1)T_+. Points corresponding to different schemes are denoted in Fig. 3.1c. **b.** Scanning electron microscopy image of the device. Green (orange) dots indicate the left (right) ST_0 qubit Q_L (Q_R), and the yellow dot indicates the rf single-electron transistor (rf-set). The blue arrow indicates the external magnetic field direction. The white scale bar corresponds to 500 nm. **c**.(**d.)** Charge stability diagram for Q_L (Q_R) operation with the pulse cycling I – W – O – W – R points superimposed. The red dashed line shows the boundary of the region inside which the EST readout is appropriate. The inset of **c.** shows the PSB readout signal for the same area observed by gated integration. The yellow line in **d.** shows the electron transition signal of the QD coupled to V_2.

The blue rectangular regions in Fig. 3.1a show the position of ε and the energy level configuration used for EST state initialization and readout. At this readout point, the PSB is lifted, and both S and T_0 levels can first occupy the (2,0) charge state, the energies of which are separated by ST_0 splitting typically in the order of ~ 25–30 GHz [38], depending on the dot-confining potential. Near the (1,0) - (2,0) electron transition, the electrochemical potential of the reservoir resides between these states, which enables the EST of the ST_0 qubits. As discussed in detail below, we observe the single-shot spin-dependent tunneling signal where one electron occupying an excited orbital state of the (2,0)T_0 state tunnels to the reservoir to form the (1,0) charge state, leading to an abrupt change in the sensor signal, and predominantly initializes back to the energetically favorable (2,0)S state. In contrast, no tunneling occurs for the (2,0)S state (see Fig. 3.1a, blue right panel).

We study a quadruple QD array with an rf single-electron transistor (rf-set) sensor consisting of Au/Ti metal gates on top of a GaAs/AlGaAs heterostructure, where a 2D electron gas (2DEG) is formed approximately 70 nm below the surface (Fig. 3.1b). A 250 nm-thick rectangular Co micromagnet with large shape anisotropy was deposited on top of the heterostructure to generate stable $\Delta B_{//}$ for ST_0 qubit operation [33,36,39,40] (see methods section for fabrication details). The device was placed on a plate in a dilution refrigerator at ~20 mK and an in-plane magnetic field $B_{z,ext}$ of 225 mT was applied. To demonstrate the EST readout in the experiment, we independently operated and readout two ST_0 qubits (Q_L and Q_R) in the non-interacting regime by blocking Q_L–Q_R tunneling using appropriate gate voltages. We monitored the rf-reflectance of the rf-set sensor (Fig. 3.1b, yellow dot) for fast single-shot charge occupancy detection in the μs time scale [41,42]. The intra qubit tunnel couplings for both Q_L and Q_R were tuned above 8 GHz to suppress unwanted Landau–Zener–Stuckelberg interference under fast ε modulation, and we estimated the electron temperature to be approximately 230 mK (see also Supplementary Note 3.1).

We first locate appropriate EST readout points in the charge stability diagrams. Figure 3.1c (1d) shows the relevant region in the stability diagram for the Q_L (Q_R) qubit operation as a function of two gate voltages V_1 (V_3) and V_2 (V_4). We superimpose the cyclic voltage pulse, sequentially reaching I – W – O – W – R points in the stability diagram (see Fig. 3.1c and 3.1d) with a pulse rise time of 200 ps. During the transition from the point W to point O stage, the pulse brings the initialized (2,0)S state to the deep (1,1) region non-adiabatically, and the time evolution at point O results in coherent S-T_0 mixing due to $\Delta B_{//}$. The resultant non-zero T_0 probability is detected at the I/R point. For this initial measurement, the duration of each pulse stage was not strictly calibrated, but the repetition rate was set to 10 kHz. The resulting ‘mouse-bite’ pattern inside the (2,0) charge region (Fig. 3.1c., boundary marked by the red dashed line) implies the (1,0) charge occupancy within the measurement window, which arises from the EST of the ST_0 qubit states averaged over 100 μs. For comparison, we note that the PSB readout signal with a similar pulse sequence is not clearly visible in the main panel of Fig. 3.1c in the time-averaged manner due to fast relaxation, as described above. The inset in Fig. 3.1c shows the PSB readout signal measured by gated (boxcar) integration (see Supplementary Note 3.2), where an approximately 100 ns gate window was applied immediately after the pulse sequence. This difference in the available range of measurement time scale clearly contrasts two distinct readout mechanisms for the spin-to-charge conversion of ST_0 qubits.

The PSB and EST readouts are systematically compared through time-resolved relaxation measurements, which also serve as calibration of the readout parameters for EST readout visibility optimization. Fig. 3.2a (2b) shows the relaxation of the sensor signal as a function of waiting time τ before reaching the measurement stage, using the pulse sequence shown in the inset of Fig. 3.2a (3.2b) near the PSB (EST) readout position for Q_L (see Supplementary Note 3.3 for measurement result and fidelity analysis of Q_R). As expected, the lifetime T_1 of the T_0 state at the PSB region is in the order of 200 ns, indicating strong spin state mixing and subsequent charge tunneling due to the large $\Delta B_{//}$ produced by the micromagnet (see Supplementary Note 3.4 for magnetic field simulation). However, at large negative ε, the PSB is eventually lifted, and the absence of rapid spin mixing as well as the insensitivity of the (2,0)T_0 – (2,0)S spin splitting to charge fluctuations ensures the long lifetime of the T_0 state. The evolution time at O is varied in the EST relaxation time measurement in Fig. 3.2b, and the amplitude decay of the coherent oscillation is probed to remove background signals typically present for long pulse repetition periods. The resultant T_1 of 337 μs is three orders of magnitude longer than that in PSB readout. Without fast ε modulation, a long T_1 exceeding 2.5 ms has been reported in GaAs QDs [43] implying that further optimization is possible.

Measurement fidelity optimization

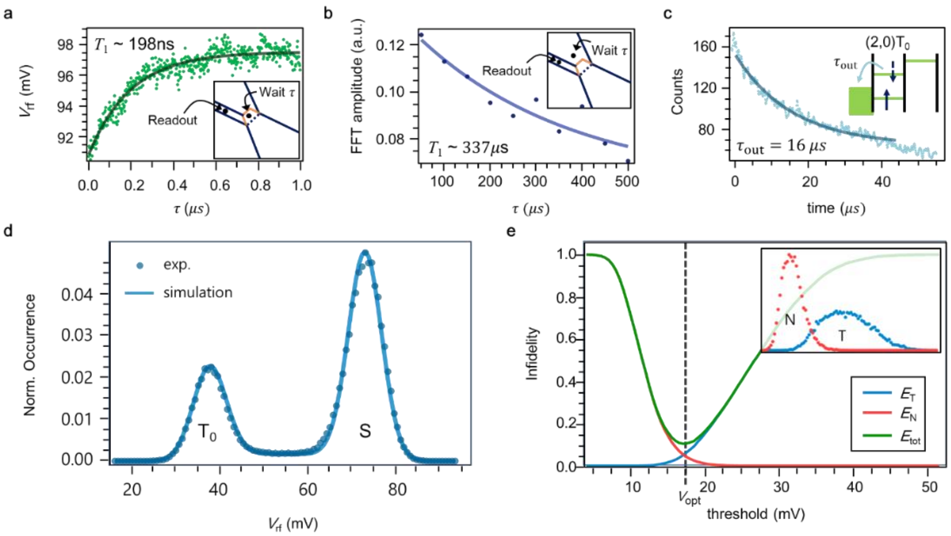

Figure 3.2 Time-resolved relaxation measurements and fidelity analysis of Q_L a. Relaxation time measurement at PSB readout. The time-averaged rf-demodulated signal V_{rf} is recorded as a function of the waiting time τ at the ε denoted in the inset. T_1 ~ 200 ns is extracted from the fitting data to the exponential decay curve. **b.** Relaxation time measurement near EST readout. The decay of the coherent oscillation is observed along the waiting time τ near the detuning at the measurement point denoted in the inset. T_1 ~ 337 μs is extracted. **c.** Histogram of the tunneling out events triggered by the end of the manipulation pulse as a function of time. **d.** Histogram of the experimental and simulated rf-demodulated single-shot traces with the application of π pulses for EST readout showing a mean value separation of more than 8 times the standard deviation. **e.** Tunneling detection infidelity calculated from the CDS peak amplitude histogram shown in the inset. Minimum total error (E_T + E_N) of ~10.5% corresponding to E_T ~ 5 % , and E_N ~ 5.5 %are estimated at the optimal threshold voltage V_{opt}.

Next, we discuss the calibration of the tunnel rates for single-shot readout and the optimization of the readout fidelity and visibility with the given experimental parameters. While for time-averaged charge detection we use a minimum integration time of 30 ns in the signal demodulation setup, corresponding to a measurement bandwidth of 33 MHz, we set the integration time to 1 μs for single-shot detection to increase the signal to noise ratio, and we typically tune the tunneling rates to less than 1 MHz. Fig. 3.2c shows time-resolved tunnel out events triggered by the end of the pulse sequence from which we measure the tunneling out rate $\nu_{out} \sim \tau_{out}^{-1} = (16\ \mu s)^{-1}$, extracted from the fit to an exponentially decaying function. The rate is within our measurement bandwidth. Also note that the ratio T_1/τ_{out} is at least 20, which is reasonable to perform high-fidelity measurements above 90% [44]. Fig. 3.2d shows the resultant histogram showing a separation of the mean value of the S and T_0 signal levels of more than 8 times the standard deviation, confirming the high fidelity of single-shot spin state detection with 1 μs integration time. We also find good agreement between the experimental and numerically simulated single-shot histograms [3] generated using the measured tunneling rates and signal to noise ratio (See Supplementary Note 3.5 for details).

After the rf demodulation stage, we further apply correlated double sampling (CDS) [15] to the single-shot traces to simplify the state discrimination and measurement automation. Using a fast boxcar integration with two gate windows that are 5 μs apart in the time domain, a dc background-removed pseudo-time derivative of the single-shot traces is generated, enabling separate detection of tunneling out/in events with an external pulse counter (Stanford Research Systems, SR400 dual gated photon counter) and time-correlated pulse counting with a multichannel scaler (Stanford Research Systems, SR430 multichannel scaler) without the need for customized field-programmable gate array (FPGA) programming [37,45] (see Supplementary Note 3.2 for details of the CDS scheme). While this scheme was successful, the electronic measurement bandwidth was further reduced to 200 kHz for single-shot detection, which resulted in a relatively long readout time requiring relatively slow tunneling rates. To simulate realistic measurement conditions, we applied the numerical CDS filter to the simulated single-shot traces (Fig. 3.2e) and reproduced the tunneling detection fidelity of the measurement setup. As the measured electron temperature (230 mK ~ 5~6 GHz·h/k_B, where h is the Planck's constant and k_B is the Boltzmann's constant) compared to the ST_0 splitting (25~30 GHz) may trigger unwanted events such as false initialization, thermal tunneling of the ground state, and double-tunneling events within the measurement windows, we have introduced corresponding thermal parameters to the analysis. The parameters were utilized to model the Larmor oscillation measured (see Fig. 3.3), and the values were extracted from the least squares fitting with the experimental data to yield the final measurement fidelity (see Supplementary Note 3.5 for measurement fidelity analysis). The resulting theoretical measurement fidelity of the Q_L is 90±1.3 %, corresponding to a visibility of 80±2.6 %, confirming that high-fidelity single-shot detection is possible at the given experimental conditions. Moreover, in Supplementary Note 3.6, we show through numerical simulation that FPGA-based single-shot detection, which we plan to perform in the future, will yield a measurement fidelity (visibility) of 94% (89%) at the same experimental condition through faster and more accurate peak detection which lowers the tunneling detection infidelity.

High-visibility quantum control with the EST readout

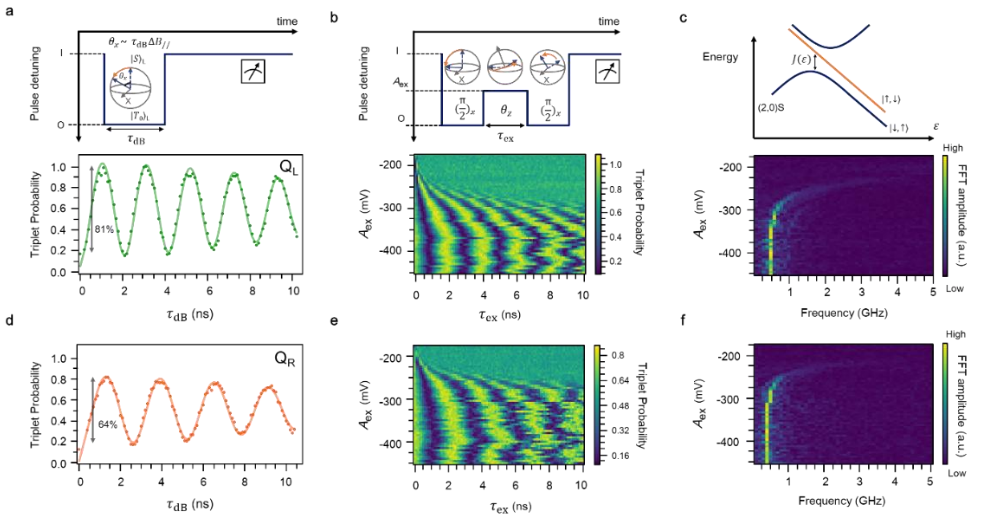

Figure 3.3 High-visibility two-axis control of two ST_0 qubits. a. (**d.**) Coherent ST_0 oscillation of Q_L (Q_R) under large $\Delta B_{//}$. 81% (64%) quantum oscillation visibility is defined by the initial oscillation amplitude which is in good agreement with the analytic model with thermal effects and spin relaxation (See Supplementary Note 3.5). **b.** (**e.**) Coherent exchange oscillation and two-axis control of Q_L (Q_R) on the Bloch sphere. The top panel of **b.** shows the Ramsey pulse sequence where the first $\pi/2$ pulse induces equal superposition of S and T_0 spin states, and the phase evolution under non-zero $J(\varepsilon)$ is probed by the second $\pi/2$ pulse. By varying the pulse amplitude A_{ex} and the evolution time τ_{ex} at the exchange step, the high-resolution rotation axis evolution and an energy spectrum consistent with the expected functional form of $J(\varepsilon)$ [38], the schematic of which is shown in the top panel of **c.**, are confirmed by the fast Fourier transform (FFT) plots in **c.** (**f.**).

We now demonstrate high-visibility coherent qubit operations with the EST single-shot readout. The panels in Fig. 3.3 show the high-visibility two-axis control of Q_L (Figs. 3a–c) and Q_R (Figs. 3d–f) under large $\Delta B_{//}$ recorded with a single rf-set. For the $\Delta B_{//}$ oscillations (Figs. 3a, 3d), the I – W – O – W – R with the period of 150 μs (Fig. 3.3a, top panel) was applied, and the evolution time at O was varied from 0 to 10 ns. Each trace in Figs. 3a and 3d is the average of 50 repeated measurements with 2000 shots per point, which takes over 5 min; thus, we expect an ensemble-averaged coherence time of ST_0 qubit oscillation T_2^* in the order of 15 ns, limited by nuclear bath fluctuation [1]. We clearly observe coherent oscillations of Q_L (Q_R) with ~81% (~64%) visibility, which is consistent with the results of the numerical simulation reported in Supplementary Note 3.5. Under the large $\Delta B_{//}$ of 100 (80) mT, corresponding to an oscillation frequency of 500 (400) MHz, we expect the Q-factor (T_2^*/T_π) of the oscillation to reach up to 28 (22) for Q_L (Q_R), even with the measured ensemble-averaged T_2^*~ 15 ns. Moreover, we estimate the leakage probability during the fast ramp less than 2% (see Supplementary Note 3.7); thus, we assume here that the effect of leakage error to the visibility is not significant. As discussed above, electronic bandwidth owing to the CDS technique is one of the factors limiting the visibility for both Q_L and Q_R. Moreover, we estimate about 8% (9%) probability that the ground state tunnel out to the reservoir and 4% (2%) probability of false initialization to T_0 state for Q_L (Q_R), showing that the reduction of the measurement fidelity and visibility in our experiment stems from the combination of the thermal effects, spin relaxation, and electronic bandwidth of the CDS method. For Q_R, tuning to an even longer τ_{out} of 25 μs was necessary to account for the reduced rf-set sensor's signal contrast to farther QDs, for which the final visibility is approximately 64%. However, as shown in Supplementary Note 3.6, the visibility of the further QDs can be easily enhanced to more than 78% by simply improving the electronics of the measurement system, for example, with FPGA programming.

To acquire the 2D plots shown in Figs. 3b and 3e, the typical Ramsey pulse sequence of I – W – O (π/2) – A_{ex} – O (π/2) – W – R (Fig. 3.3b, top panel) was applied, and the detuning amplitude A_{ex} and evolution time τ_{ex} at the exchange step were varied. The figures show high-visibility quantum oscillation as well as continuous evolution of rotation axis on the Bloch sphere as A_{ex} is varied over different regimes, where T_2^* is limited by the charge noise for $J(\varepsilon) > \Delta B_{//}$ or by fluctuations in $\Delta B_{//}$ for $J(\varepsilon) \sim 0$. The fast Fourier transform (FFT) of the exchange oscillations along the exchange detuning axis (Figs. 3c and 3f) confirms the control of the ST_0 qubit over the two axes on the Bloch sphere for both Q_L and Q_R, which is consistent with the expected qubit energy splitting (Fig. 3.3c, top panel). We emphasize that the measurement of two qubits is possible with one accompanied rf-set, which can be useful for the linear extension of the ST_0 qubits because the charge sensor does not need to be aligned with the QD array. In this work, we focused on independent two single-qubit gate operation; nevertheless, we expect that long T_1 at EST readout will allow the sequential measurement of two qubit states for a given quantum operation, which, in turn, will allow two qubit correlation measurement, enabling full two qubit state and process tomography in the future. Characterization of the two qubit interaction of ST_0 qubits in the current quadruple dot array, for example by dipole coupling [6,10] or exchange interaction [36], is the subject of current investigations.

Discussion

High-visibility readout of the ST_0 qubit at large $\Delta B_{//}$ is necessary for high-fidelity ST_0 qubit operations [6,37]. We performed high-visibility single-shot readout of two adjacent ST_0 qubits at $\Delta B_{//}$ of 100 mT (~500 MHz$\cdot h\cdot(g^*\mu_B)^{-1}$) by direct EST with one rf-set. No mixing between T_0 and (1,1)S state was observed at the EST readout point, which would allow sequential readout of multiple arrays of qubits due to the long T_1. Full one-electron signal difference discriminates the S and T_0 states compared to other readout methods where the dipolar charge difference is measured to readout the ST_0 qubit states [13,16]. This feature can be especially useful for scaling up the ST_0 qubits for the following reasons: 1) the large signal contrast can result in high visibility and low measurement error, and 2) the sensor does not need to be aligned along the QD array. Especially for GaAs spin qubits, high-visibility ST_0 qubit readout allows fast nuclear-spin fluctuation measurements, which will enable accurate feedback/stabilization of the nuclear spin bath for high-fidelity qubit control [2,32,37]. Furthermore, our method does not require additional metastable states [15,17,46] or pulsing sequences for high-fidelity measurements at large $\Delta B_{//}$ [14,16], showing that the experimental complexity is greatly reduced. EST readout of ST_0 qubits in nuclear spin-free systems, including Si, may also enhance the measurement fidelity by providing even longer T_1 for electron spins [7,47,48]. We further expect that the large $\Delta B_{//}$ based high-fidelity control combined with the high-fidelity readout method will be a powerful tool not only for single-qubit operations but also for exploring the charge-noise insensitive two-qubit operations of the ST_0 qubits using extended sweet spot [6].

Because the highest bandwidth potential of rf-reflectometry cannot be fully exploited with the CDS technique used in this study, we expect that the use of FPGA to detect the peaks from the bare rf demodulated single-shot traces will enhance the visibility to at least 88% (78%) for Q_L (Q_R). The use of FPGA programming will also allow faster nuclear environment Hamiltonian learning [37], which can be useful in, for example, studying the time-correlation of nuclear spin bath fluctuations at different QD sites. We have taken the thermal tunneling probabilities into the analysis, and have successfully modeled the coherent ST_0 oscillation in our measurement setup, and derived the measurement fidelities. In the future, we plan to improve the performance by adopting an FPGA-based customized measurement, reducing electron temperature, and further optimizing the electronic signal path. However, even with the current limitations, the achieved visibility of 81% for ST_0 qubits at large $\Delta B_{//}$ shows potential to realize high-fidelity quantum measurements in scalable and individually addressable multiple QD arrays in semiconductors.

Methods

Device Fabrication. The quadruple QD device was fabricated on a GaAs/AlGaAs heterostructure with a 2DEG formed 73 nm below the surface. The transport property of the 2DEG shows mobility $\mu = 2.6\times10^{6}$ cm^{2} V^{-1} s^{-1} with electron density n = 4.6×10^{11} cm^{-2} and temperature T = 4 K. Mesa was defined by the wet etching technique to eliminate the 2DEG outside the region of interest. Ohmic contact was formed through metal diffusion to connect the 2DEG with the electrode on the surface. The depletion gates were fabricated on the surface using standard e-beam lithography and metal evaporation. The QD array axis was oriented parallel to the [011] crystallographic direction of GaAs. Subsequently, the micromagnet was patterned perpendicular to the QD array using standard e-beam lithography, and a Ni 10 nm/Co 250 nm/Au 5 nm was deposited using metal evaporation.

Measurement. The experiments were performed on a quadruple QD device placed on the 20 mK plate in a commercial dilution refrigerator (Oxford instruments, Triton-500). Rapid voltage pulses generated by Agilent M8195A arbitrary waveform generator (65 GSa/s sampling rate) and stable dc voltages generated by battery-operated voltage sources (Stanford Research Systems SIM928) were applied through bias-tees (picosecond Pulselabs 5546) in the dilution refrigerator before applying the metal gates. An LC-resonant tank circuit was attached to one of the ohmic contacts near the rf-set with a resonance frequency of ~110 MHz for homodyne detection. The reflected rf-signal was first amplified at 4 K with a commercial cryogenic amplifier (Caltech Microwave Research, CITLF2) and then further amplified at room temperature with home-made low-noise amplifiers. Signal demodulation was performed with an ultra-high-frequency lock-in amplifier (Zurich instrument UHFLI), and the demodulated amplitude was processed using a boxcar integrator built in the UHFLI for CDS. The CDS peaks were counted with an external photon counter (Stanford Research, SR400). The pulse parameters could be rapidly swept via a hardware looping technique, which enabled fast acquisition of the $\Delta B_{//}$oscillations. In Supplementary Note 3.8, we show the details of the measurement setup, CDS technique, and signal analysis.

References

[1] J. R. Petta *et al.* Coherent manipulation of coupled electron spins in semiconductor quantum dots. *Science* **309**, 2180–2184 (2005).

[2] S. Foletti, H. Bluhm, D. Mahalu, V. Umansky, and A. Yacoby, Universal quantum control of two-electron spin quantum bits using dynamic nuclear polarization. *Nat. Phys.* **5**, 903–908 (2009).

[3] A. Morello *et al.* Single-shot readout of an electron spin in silicon. *Nature* **467**, 687–691 (2010).

[4] D. M. Zajac *et al.* Resonantly driven CNOT gate for electron spins. *Science* **359**, 439–442 (2018).

[5] D. Kim *et al.* High-fidelity resonant gating of a silicon-based quantum dot hybrid qubit. *npj Quantum Inf.* **1**, 15004 (2015).

[6] J. M. Nichol *et al.* High-fidelity entangling gate for double-quantum-dot spin qubits. *npj Quantum Inf.* **3**, 3 (2017).

[7] J. Yoneda *et al.* A quantum-dot spin qubit with coherence limited by charge noise and fidelity higher than 99.9%. *Nat. Nanotechnol.* **13**, 102 (2018).

[8] M. Veldhorst *et al.* An addressable quantum dot qubit with fault-tolerant control-fidelity. *Nat. Nanotechnol.* **9**, 981–985 (2014).

[9] D. Kim *et al.* Quantum control and process tomography of a semiconductor quantum dot hybrid qubit. *Nature* **511**, 70–74 (2014).

[10] M. D. Shulman *et al.* Demonstration of entanglement of electrostatically coupled singlet-triplet qubits. *Science* **336**, 202–205 (2012).

[11] J. M. Elzerman *et al.* Single-shot read-out of an individual electron spin in a quantum dot. *Nature* **430**, 431–435 (2004).

[12] T. Meunier *et al.* High fidelity measurement of singlet–triplet state in a quantum dot. *Phys. status solidi B* **243**, 3855–3858 (2006).

[13] C. Barthel, D. J. Reilly, C. M. Marcus, M. P. Hanson, and A. C. Gossard, Rapid single-shot measurement of a singlet-triplet qubit. *Phys. Rev. Lett.* **103**, 160503 (2009).

[14] P. Harvey-Collard *et al.* High-fidelity single-shot readout for a spin qubit via an enhanced latching mechanism. *Phys. Rev. X* **8**, 021046 (2018).

[15] T. Nakajima *et al.* Robust single-shot spin measurement with 99.5% fidelity in a quantum dot array. *Phys. Rev. Lett.* **119**, 017701 (2017).

[16] L. A. Orona *et al.* Readout of singlet-triplet qubits at large magnetic field gradients. *Phys. Rev. B* **98**, 125404 (2018).

[17] M. A. Broome *et al.* High-fidelity single-shot singlet-triplet readout of precision-placed donors in silicon. *Phys. Rev. Lett.* **119**, 046802 (2017).

[18] K. Eng *et al.* Isotopically enhanced triple-quantum-dot qubit. *Sci. Adv.* **1**, e1500214 (2015).

[19] L. A. Tracy *et al.* Single shot spin readout using a cryogenic high-electron-mobility transistor amplifier at sub-Kelvin temperatures. *Appl. Phys. Lett.* **108**, 063101 (2016).

[20] T. F. Watson *et al.* A programmable two-qubit quantum processor in silicon. *Nature* **555**, 633–637 (2018).

[21] M. Veldhorst *et al.* A two-qubit logic gate in silicon. *Nature* **526**, 410–414 (2015).

[22] A. C. Johnson, J. R. Petta, C. M. Marcus, M. P. Hanson, and A. C. Gossard, Singlet-triplet spin blockade and charge sensing in a few-electron double quantum

dot. *Phys. Rev. B* **72**, 165308 (2005).

[23] A. C. Johnson *et al.* Triplet–singlet spin relaxation via nuclei in a double quantum dot. *Nature* **435**, 925–928 (2005).

[24] J. R. Petta *et al.* Pulsed-gate measurements of the singlet-triplet relaxation time in a two-electron double quantum dot. *Phys. Rev. B* **72**, 161301 (2005).

[25] C. Volk *et al.* Loading a quantum-dot based "Qubyte" register. *npj Quantum Inf.* **5**, 29 (2019).

[26] A. R. Mills *et al.* Shuttling a single charge across a one-dimensional array of silicon quantum dots. *Nat. Commun.* **10**, 1063 (2019).

[27] F. Martins *et al.* Negative spin exchange in a multielectron quantum dot. *Phys. Rev. Lett.* **119**, 227701 (2017).

[28] M. G. Borselli *et al.* Undoped accumulation-mode Si/SiGe quantum dots. *Nanotechnology* **26**, 375202 (2015).

[29] W. H. Lim *et al.* Electrostatically defined few-electron double quantum dot in silicon. *Appl. Phys. Lett.* **94**, 173502 (2009).

[30] C. Barthel *et al.* Relaxation and readout visibility of a singlet-triplet qubit in an Overhauser field gradient. *Phys. Rev. B* **85**, 035306 (2012).

[31] J. R. Petta *et al.* Dynamic nuclear polarization with single electron spins. *Phys. Rev. Lett.* **100**, 067601 (2008).

[32] H. Bluhm, S. Foletti, D. Mahalu, V. Umansky, and A. Yacoby, Enhancing the coherence of a spin qubit by operating it as a feedback loop that controls its nuclear spin bath. *Phys. Rev. Lett.* **105**, 216803 (2010).

[33] J. Yoneda *et al.* Robust micromagnet design for fast electrical manipulations of single spins in quantum dots. *Appl. Phys. Express* **8**, 084401 (2015).

[34] T. Ito *et al.* Four single-spin Rabi oscillations in a quadruple quantum dot. *Appl. Phys. Lett.* **113**, 093102 (2018).

[35] A. J. Sigillito *et al.* Site-selective quantum control in an isotopically enriched Si 28 / Si 0.7 Ge 0.3 quadruple quantum dot. *Phys. Rev. Appl.* **11**, 061006 (2019).

[36] A. Noiri *et al.* A fast quantum interface between different spin qubit encodings. *Nat. Commun.* **9**, 5066 (2018).

[37] M. D. Shulman *et al.* Suppressing qubit dephasing using real-time Hamiltonian estimation. *Nat. Commun.* **5**, 5156 (2014).

[38] O. E. Dial *et al.* Charge noise spectroscopy using coherent exchange oscillations in a singlet-triplet qubit. *Phys. Rev. Lett.* **110**, 146804 (2013).

[39] S. Chesi *et al.* Single-spin manipulation in a double quantum dot in the field of a micromagnet. *Phys. Rev. B* **90**, 235311 (2014).

[40] M. Pioro-Ladrière *et al.* Electrically driven single-electron spin resonance in a slanting Zeeman field. *Nat. Phys.* **4**, 776–779 (2008).

[41] D. J. Reilly, C. M. Marcus, M. P. Hanson, and A. C. Gossard, Fast single-charge sensing with a rf quantum point contact. *Appl. Phys. Lett.* **91**, 162101 (2007).

[42] C. Barthel *et al.* Fast sensing of double-dot charge arrangement and spin state with a radio-frequency sensor quantum dot. *Phys. Rev. B* **81**, 161308 (2010).

[43] R. Hanson *et al.* Single-shot readout of electron spin states in a quantum dot using spin-dependent tunnel rates. *Phys. Rev. Lett.* **94**, 196802 (2005).

[44] D. Keith *et al.* Benchmarking high fidelity single-shot readout of semiconductor qubits. *New J. Phys.* **21**, 063011 (2019).

[45] E. Kawakami *et al.* Gate fidelity and coherence of an electron spin in an Si/SiGe quantum dot with micromagnet. *Proc. Natl. Acad. Sci. USA* **113**, 11738–11743

(2016).

[46] S. A. Studenikin *et al.* Enhanced charge detection of spin qubit readout via an intermediate state. *Appl. Phys. Lett.* **101**, 233101 (2012).

[47] W. Huang *et al.* Fidelity benchmarks for two-qubit gates in silicon. *Nature* **569**, 532–536 (2019).

[48] E. Kawakami *et al.* Electrical control of a long-lived spin qubit in a Si/SiGe quantum dot. *Nat. Nanotechnol.* **9**, 666–670 (2014).

Supplementary Information 3

Supplementary Note 3.1. Electron temperature and intra-qubit tunnel coupling calibration

Electron temperature, and the tunnel coupling strength of the left double quantum dot are measured using the standard lock-in technique. dV_{rf}/dV_2 is observed by modulating V_2 gate voltage with 337Hz frequency. With proper adjustment of dot-reservoir tunnel rates less than 1 MHz and setting minimal modulation amplitude, the electron temperature T_e ~ 230mK is determined by fitting the heterodyne detected single electron transition line to the equation $\frac{dV_{rf}}{dV_2}(V_1) = A_{offset} - \frac{A\alpha}{k_B T}\frac{\exp(\alpha(V_1 - V_{offset})/k_B T)}{(1+\exp(\alpha(V_1 - V_{offset})/k_B T))^2}$, which is the derivative of the typical Fermi-Dirac distribution (Supplementary Fig. 3.1a). Here α = 0.035 is the lever-arm of the V_1 gate obtained from the Coulomb diamond measurement, k_B is the Boltzmann constant, and A_{offset} and V_{offset} are the dV_{rf}/dV_2 offset and the offset V_1 voltage in the $dV_{rf}/dV_2 - V_1$ plot, respectively. The intra-qubit tunnel coupling strength t_c was obtained in the similar manner, by sweeping the gate voltage through the inter-dot transition line in the stability diagram for example shown in Fig. 1c of the main text. The broadening is fitted using the same equation described above, with the broadening width $2t_c$ instead of $k_B T$ where the t_c represents the tunnel coupling strength. The resultant $2t_c/h$ is 16 GHz where h is the Plank's constant.

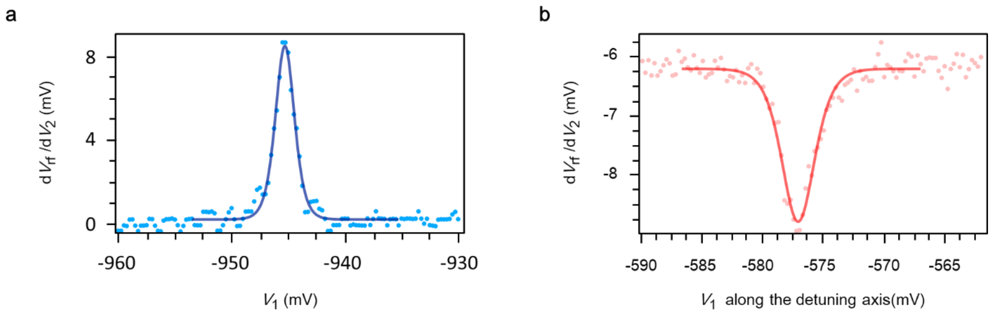

Supplementary Figure 3.1 System parameter calibration. a. Electron temperature measurement. **b.** tunnel coupling strength measurement using the heterodyne detection scheme. Typical lock-in measurement was performed to obtain the broadening of the single electron transition due to thermal broadening and the intra-qubit tunneling. Electron temperature T_e ~ 230 mK, and tunnel coupling t_c/h ~ 8GHz were obtained from the fitting. When obtaining **b.** both V_1, and V_2 were swept through the inter-dot transition line in Fig. 3.1c, but only the V_1 gate voltage is shown in the x-axis.

Supplementary Note 3.2. Correlated double sampling (CDS)

By resampling the demodulated rf-signal with the boxcar integrator, we enable the real-time single-shot event counting without the use of field-programmable gate arrays (FPGA) programming. As shown in Supplementary Fig. 3.2, the boxcar integrator subtracts the 100 ns-averaged baseline signal from the gate signal which are separated by 5 μs in the time domain to yield a pseudo-time derivative signal of the single-shot trace with 200 kHz sampling rate. CDS converts the falling (rising) edge to the positive (negative) peak and the peaks are detected by the external photon counter (Stanford Research Systems SR400) as shown in Supplementary Fig. 3.2a. This allows the separate detection of tunneling in / out event in real-time without post-processing which may reduce the experimental overhead in the analysis step. By counting the tunneling out events, we have observed the coherent singlet-triplet qubit (ST_0 qubit) oscillations in the energy selective tunneling (EST) readout point in the main text. For single-shot readout, the boxcar integrator is operated with average number set to 1 (no averaging).

When averaged, however, the CDS technique can also be utilized to observe short-lived T_0 signal for Pauli Spin Blockade (PSB) readout, which enable measurement bandwidth of 33MHz in time averaged manner (see also the inset to Fig. 3.1c in the main text). By setting the ~ 0.1 μs gate window right after the spin-mixing pulse comes back to the PSB region, and the ~ 0.1 μs baseline gate window before the next pulse start as shown in Supplementary Fig. 3.2b, the demodulated signal is effectively sampled for short time where the portion of the T_0 signal is sufficiently large to be observed with sufficient periodic average.

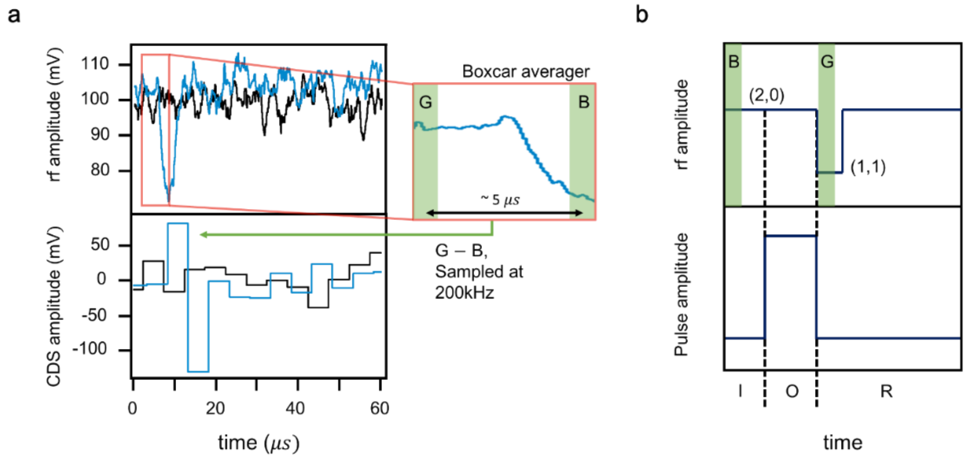

Supplementary Figure 3.2 Correlated double sampling schematics. a. Correlated double sampling for tunneling out / in event detection. Boxcar integrator resamples the bare demodulated rf signal by subtracting the ~ 100 ns averaged baseline (B) signal from the gate (G) signal every 5 μs. This resampling process converts the falling edge signal of the rf signal to a positive peak with removing dc background and produces pulse signal robust to background drift. **b.** CDS scheme for short T_0 signal detection in PSB readout. Pulse mixes the S and T_0 states in the operation (O) sequence, and when returning to the readout (R) step, the T_0 quickly relaxes to (2,0) charge state under large magnetic field difference. The boxcar integrator in this case is operated in averaging mode where sampled signal G of the rf-signal for short period time after the pulse sequence are subtracted by the B signal and averaged about 5000 times to increase signal to noise ratio.

Supplementary Note 3.3. Right qubit measurement fidelity

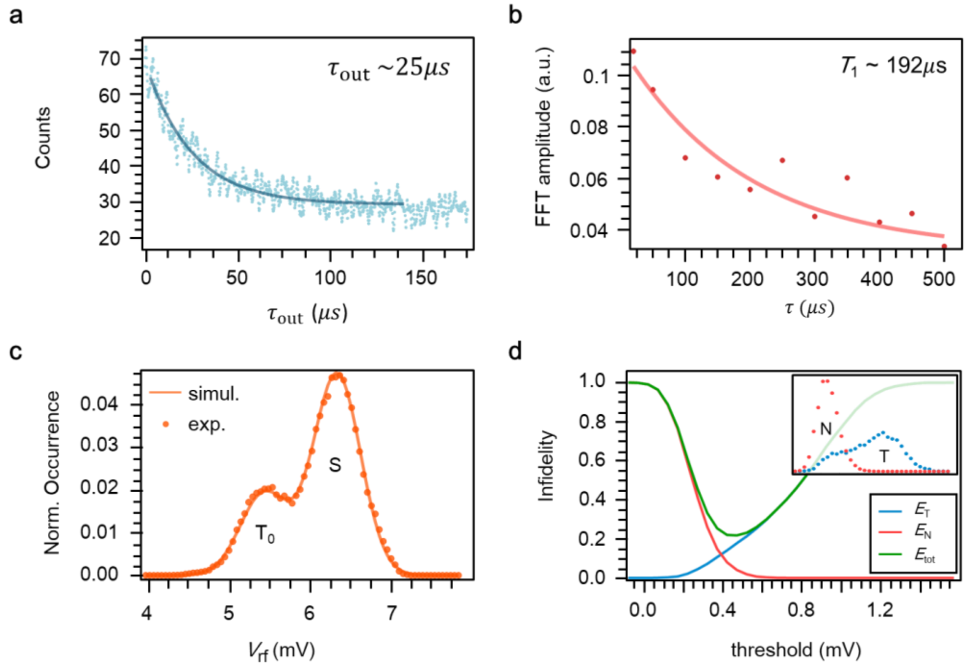

Supplementary Figure 3.3 Right qubit readout fidelity analysis. a. Tunneling out rate of the right qubit Q_R at the EST readout point. Tunneling out events were recorded as a function of the tunneling time, and the exponential fit to the curve yields $\tau_{out} \sim 25$ μs. **b.** Relaxation time measurement near EST readout point. The decay of the coherent oscillation is observed along the waiting time τ near the EST readout point. $T_1 \sim 192$ μs is extracted from the fit. **c.** Experimental, and simulated rf single-shot traces of the Q_R with the π-pulse applied. **d.** Tunneling detection infidelity calculated from the CDS peak amplitude histogram shown in the inset. Minimum total error (E_T + E_N) of 28.2% corresponding to $E_T \sim 19\%$, and $E_N \sim 9.2\%$ are estimated at the optimal threshold.

Supplementary Note 3.4. Magnetic field simulation

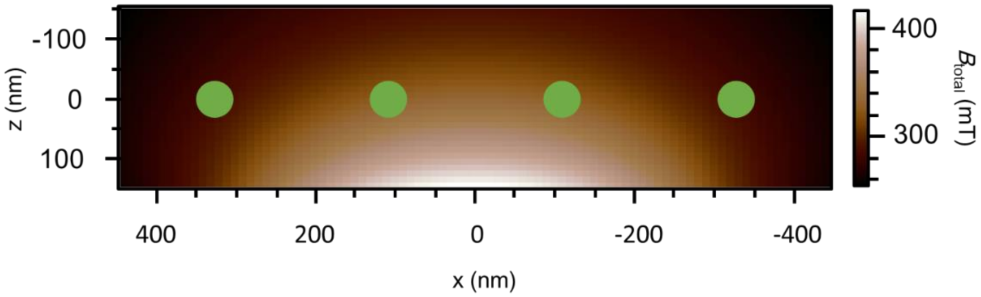

Supplementary Figure 3.4 Simulation of the magnetic field around the QDs. The total magnetic field strength around the quantum dots in our device (see Supplementary Fig. 3.8) is simulated using the boundary integral method with RADIA [1,2] package. Green dots indicate the quantum dot positions. The fast $\Delta B_{//}$oscillations shown in Fig. 3.3 in the main text is up to 500MHz corresponding to $\Delta B_{//}$ of 100 mT, and we ascribe this higher-than-expected- $\Delta B_{//}$ to the displacement of the electrons from the expected positions by the confining potential in the few electron regime.

Supplementary Note 3.5. Measurement fidelity analysis

We have taken the thermal tunneling events into consideration for the fidelity analysis and describe the analysis protocol in detail here. We first define two parameters α_1, and β where α_1 corresponds to the probability for the ground (S) state to tunnel out to the reservoir within a measurement window, and β corresponds to the false initialization probability following the Pla. *et al.*[3]. Regarding the false initialization we assume the following for three triplet states – T_0, T_+, and T_-.

1) Probabilities for the electron to falsely initialize to different triplet states are all equal to $\beta / 3$.

2) The relaxation time is equal for all T_0, T_+, and T_- state.

3) T_+ (1,1), and T_- (1,1) states do not evolve to other states during the Larmor oscillation phase.

It should be noted that while the false initialization to T_0 state contribute to the visibility loss while the false initialization to T_+ or T_- states would result in overall shift of the Larmor oscillation because the T_+ or T_- will not undergo coherent mixing process during the evolution time. We introduce an additional parameter, α_2 to account for the double-tunneling probability of the ground state within a single measurement window. For example, in the case that a T_0 state first tunnels out to the reservoir and initialize to the S state in a measurement phase, there still exist non-zero probability for the S state to tunnel out within the measurement window, and α_2 represents the corresponding probability. It is thus natural to define the total double tunneling probability as P_2 = (β + (1-β)/α_2) which covers the double-tunneling probability of the false initialized triplet states and the reinitialized S state after a single tunneling event.

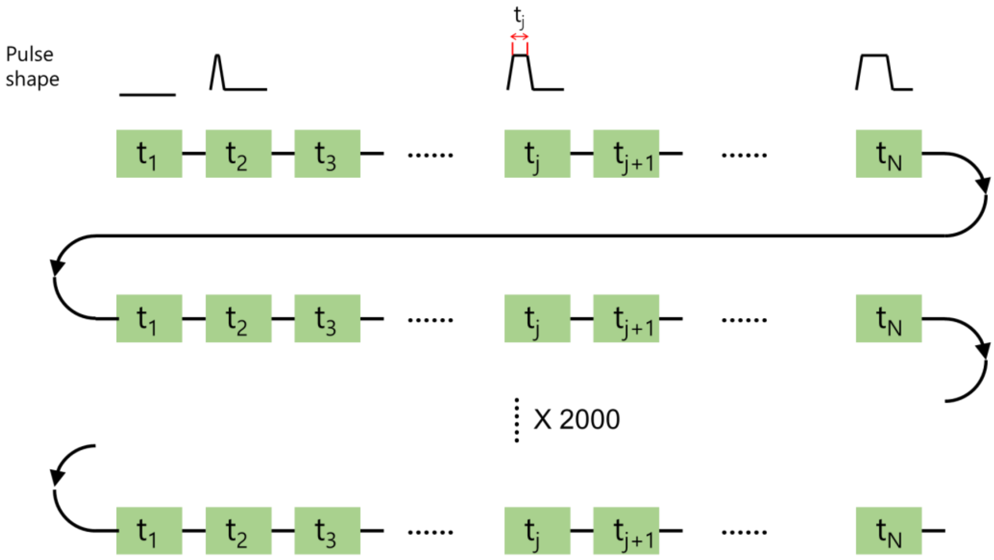

Supplementary Figure 3.5 Pulse sequence for Larmor oscillation measurement. The Larmor oscillations of Q_L and Q_R are measured by first sweeping the pulse parameter, the free evolution time t_j, and repeating the measurement over 2000 times to average traces. N different pulses corresponding to N different evolution time are all recorded in the arbitrary waveform generator (AWG) before measurements to enable the rapid hardware triggered sweep of the pulse parameter.

In the Larmor experiment in Supplementary Fig. 3.3a, 3d of the main text, we obtain the oscillation by averaging single-shot traces using the pulse sequence shown in Supplementary Fig. 3.5. As we regard the spin state is at the excited (T_0) state if there is at least one tunneling event within a measurement window, we first define the P(t_j, $\Delta B_{//}$) as the probability for at least one tunneling to occur within a single measurement window at the evolution time t_j ($1 \leq j \leq N$, j is integer) under the magnetic field difference $\Delta B_{//}$. It should be noted that $P(t_j, \Delta B_{//})$ must be derived recursively since the tunneling event at the j^{th} shot affects the tunneling probability of the $(j+1)^{th}$ shot. The relation between the $P(t_{j+1}, \Delta B_{//})$, and $P(t_j, \Delta B_{//})$ is as follows.

$$
\begin{aligned}
P(t_{j+1},\Delta B_{//}) = P(t_j,\Delta B_{//})[(1-\beta)\{f_{j+1}r+(1-f_{j+1})\alpha_1+f_{j+1}(1-r)\alpha_1\}+ \\
\frac{\beta}{3}\{f_{j+1}\alpha_1+(1-f_{j+1})r+(1-f_{j+1})(1-r)\alpha_1\}+ \\
\frac{2\beta}{3}\{r+(1-r)\alpha_1\}]+ \\
(1-P(t_j,\Delta B_{//}))(f_{j+1}r+(1-f_{j+1})\alpha_1+f_{j+1}(1-r)\alpha_1)
\end{aligned}
$$

- (1)

Here $f_{j+1} = f(t_{j+1}, \Delta B_{//}) = \sin^2(\pi\, \Delta B_{//}\, t_{j+1})$ is the ideal T_0 probability at the evolution time t_{j+1} under the magnetic field difference $\Delta B_{//}$ when the initial state is the singlet state, and (1- r) is the relaxation probability of the T_0 state within the measurement window which is given by $r = \frac{\int_0^M \exp(-t/T_1)\exp(-t/\tau_{out})dt}{\int_0^\infty \exp(-t/\tau_{out})dt}$ where M is the length of the measurement window, T_1 is the spin-relaxation time, and τ_{out} is the tunneling-out time.

However, recursively obtained $P(t, \Delta B_{//})$ cannot yet fully account for the experimentally obtained Larmor curve. We additionally define tunneling detection fidelity T_T (T_N) which is the fidelity to correctly tell there is a (no) tunneling event when there is a (no) peak in the signal. Here T_T and T_N are determined by the signal to noise ratio (SNR) of the measurement setup, and the detailed description on how to obtain the tunneling detection fidelities is given below. With P(t, $\Delta B_{//}$),T_{T}, and T_{N}, the experimental Larmor curve can be fully modeled. A(t, $\Delta B_{//}$), the average number of the tunneling events detected by the photon counter, has the following relation with the P(t, $\Delta B_{//}$).

$$\mathrm{A}(t,\Delta B_{//}) = \mathrm{P}(t,\Delta B_{//})(1+P_2)T_{\mathrm{T}} + (1-\mathrm{P}(t,\Delta B_{//}))(1-T_{\mathrm{N}}) \qquad (2)$$

Assuming that $\Delta B_{//}$ suffers from the Gaussian noise, we perform the Gaussian weighted sum of A(t, $\Delta B_{//}$)curves as below within the 5-sigma range.

$$\bar{\mathrm{A}}(t,\Delta B_{//}) = \sum_{b=\Delta B_{//}-5\sigma}^{\Delta B_{//}+5\sigma} \mathrm{A}(t,b)\,\mathrm{G}(b,\Delta B_{//},\sigma)\Delta b \qquad (3)$$

Here $G(x,\ \mu,\ \sigma)$ is the Gaussian distribution centered at μ with the standard deviation σ.

By setting α_1, α_2, β, σ, and $\Delta B_{//}$ as the fitting parameters we perform the least squares fitting of the $\bar{\mathrm{A}}(t,\Delta B_{//})$ to the experimental Larmor curve. Below we describe the protocol for obtaining the tunneling detection infidelities.

Typical measurement fidelities are acquired by obtaining the histograms of the time-resolved signals of qubit ground and excited states, and finding the adequate threshold which yields the highest visibility [4–6]. The obtained measurement fidelities not only suffer from the imperfect tunneling detection, but also from the spin-relaxation or thermal tunneling events, implying that the T_{T}, and T_{N} cannot be solely obtained experimentally. We first numerically simulate [6] the traces with the experimental parameters including the offset rf-voltage, amplitude of the tunneling peaks, tunneling in/out time, spin-relaxation (T_1) time, and sampling rate (Parameters are denoted in the Supplementary Table 3.1.). The thermal tunneling events are added to the signals in according to the thermal tunneling parameters α_1, α_2, and β, which then undergo through the numerical noise and low pass filter to yield a realistic signal. Then the amplitude of the noise filter is varied to match the experimentally obtained histogram of the rf-signal as in Fig. 3.2d, and the optimal noise amplitude is chosen. With the noise amplitude, we numerically generate the 'ideal' signals of triplets and singlets without the thermal tunneling events, or spin-relaxation to solely evaluate the tunneling detection fidelity of the electrical measurement setup. As we have utilized the CDS technique as described in Supplementary Note 3.2, corresponding boxcar filter is applied to the numerical signals, and the histograms of the boxcar-filtered signals are acquired to perform a typical integration for tunneling detection fidelity calculation [4–6]. We have plotted the tunneling detection infidelity E_T (E_N) where $E_T = 1 - T_T$ ($E_N = 1\text{-}T_N$) in the Fig. 3.2e and Supplementary Fig. 3.3d. The tunneling detection fidelities $T_T(V_{op})$, and $T_N(V_{op})$ at the optimal threshold which yields the lowest $E_{tot}(V_{op}) = E_T(V_{op}) + E_N(V_{op})$ are utilized for the Larmor curve fitting described above.

To sum up, the whole process is done as follows.

1) Put the initial guesses of parameters to perform Larmor curve fitting, and obtain the α_1, α_2, and β.
2) Use the obtained thermal tunneling parameters for rf-histogram fitting to acquire the optimal noise amplitude.
3) Generate ideal traces of the T_0, and S states with the noise amplitude from 2), and calculate T_T, and T_N
4) Use T_T, and T_N for Larmor curve fitting, and obtain α_1, α_2, and β.
5) Iteratively obtain the optimal T_T, T_N, α_1, α_2, and β..

We now turn to discuss the total measurement fidelity. If there exist thermal tunneling events irrelevant with the spin dynamics, it is difficult to tell whether the tunneling peak occurs due to the thermal effect or not upon acquiring a single-shot trace. Thereby the total measurement fidelity should now be obtained by taking α_1, α_2, and β into account. Let us define F_{T0} (F_S) as the T_0 (S) measurement fidelity, and R_{T0} (R_S) = 1 – F_{T0} (F_S) as the measurement infidelity. We first evaluate R_S by categorizing the cases which can detract the S measurement fidelity.

X_1: No tunneling occurs (1 - α_1), photon counter 'beeps' due to electrical noise (E_N)

X_2: A single tunneling occurs (α_1), photon counter detects the tunneling (1 - E_T)

X_3: A single tunneling occurs (α_1), the tunneling is not detected (E_T) but the photon counter 'beeps' due to electrical noise (E_N)

X_4: Double tunneling occurs ($\alpha_1 P_2$), first tunneling is not detected (E_T), and the second tunneling is detected (1 - E_T)

X_5: Double tunneling occurs ($\alpha_1 P_2$), both tunneling events are not detected (E_T^2), but photon counter 'beeps' due to electrical noise (E_N)

As X_1 ~ X_5 are independent, mutually exclusive,

$R_S = P(X_1) + P(X_2) + P(X_3) + P(X_4) + P(X_5)$ holds. i.e.

$$R_S = (1-\alpha_1)E_N + \alpha_1(1-E_T) + \alpha_1 E_T E_N + \alpha_1 P_2 E_T (1-E_T) + \alpha_1 P_2 E_T{}^2 E_N \qquad - (4)$$

Cases for the T_0 measurement infidelity can be similarly categorized with the relaxation process considered, as follows.

Y: T_0 relaxes within the measurement time (1- r), photon counter detects no tunneling (1 - R_S)

Z_1: T_0 does not relax within the measurement time (r), the tunneling is not detected (E_T), no additional tunneling occurs (1-P_2), counter detects no signal (1 - E_N)

Z_2: T_0 does not relax within the measurement time (r), double-tunneling occurs (P_2), both tunneling events are not detected (E_T^2)

Y, Z_1, Z_2 are all independent, and mutually exclusive leading to $R_{T0} = P(Y) + P(Z_1) + P(Z_2)$. i.e.

$$R_{T_0} = (1-r)(1-R_S) + rE_T(1-P_2)(1-E_N) + rE_T^{\,2}P_2 \qquad - (5)$$

Finally, the total measurement fidelity $F_{\mathrm{meas}} = 1 - \dfrac{(R_S + R_{T_0})}{2}$ with the spin-relaxation, thermal tunneling events, and the tunneling detection infidelity of the setup is calculated as 90±1.3% (80.3±1 %) corresponding to visibility ($F_S + F_{T0}$ -1) of 80±2.6 % (60.6±2 %) for Q_L (Q_R). Also, from the Larmor curve fitting we obtain the $\Delta B_{//}$fluctuation of σ ~15.71 MHz (15.73 MHz) corresponding to T_2^* ~ 14.33 ns (14.31 ns) for Q_L (Q_R). We assume that ~ 3% disagreement of the Q_R visibility is due to the uncertainty in measured relaxation time.

Input	**Q_L**	**Q_R**
τ_{out} (μs) –:Tunneling-out time of the triplet states	16	25.5
τ_{in} (μs) : Tunneling-in time of the singlet state	117	130.5
T_1 (μs) : Relaxation time of the triplet states	337	192
Meas. Time (μs)	150	200
Sampling rate (MHz)	14	14
CDS freq. (kHz)	200	50
CDS gate width (μs)	0.1	4
Output		
α_1 : False tunneling-out probability of the singlet state	0.081	0.092
α_2 : Double tunneling-out probability	0.08	0.089
β : False initialization probability	0.12	0.069
σ (MHz) : Std. deviation of the $\Delta B_{//}$ distribution	15.71	15.73
E_T : Tunneling detection infidelity	0.05	0.19
E_N : No-tunneling detection infidelity	0.055	0.092
R_{T0} : T_0 measurement infidelity	0.077	0.232
R_S : S measurement infidelity	0.128	0.162
F_{meas} : Total measurement fidelity	90$\pm$1.3%	80.3$\pm$1 %

Supplementary Table 3.1. Input and output parameters of the analysis

Supplementary Note 3.6. Expected fidelity with direct peak detection

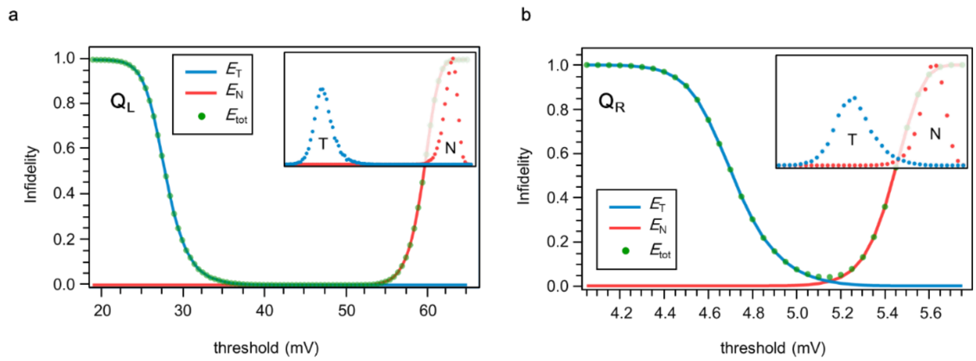

Supplementary Figure 3.6 Error simulation for direct peak detection scheme. **a.** (**b.**) The tunneling detection infidelity calculated from the rf-histogram in the inset. The histograms are constructed by sampling the peak values for Q_L (Q_R) single-shot traces without the spin relaxation, and thermal tunneling events to evaluate the tunneling detection infidelities without the CDS. For Q_L, the tunneling detection infidelities are below 0.00001% while for Q_R infidelities of E_T ~ 2 % , and E_N ~ 2 % are obtained at the optimal threshold.

The measurement fidelity and visibility are calculated for the direct peak detection scheme to explicitly show that the use of FPGA rather than CDS technique may extend the measurement fidelity and visibility with the same experimental parameters. Following the A. Morello *et al.*[6], single-shot traces were first simulated with the experimental parameters, and instead of passing through additional numerical CDS filter, the peak value (the minimum value) from each rf single-shot trace is sampled from 15,000 traces to construct the histogram shown in the insets of Supplementary Fig. 3.6a. and 6b. Because the short peaks or the full signal contrast cannot be perfectly detected with the CDS due to its limited bandwidth, the tunneling detection fidelities are naturally higher for the FPGA case. With the same τ_{out}, T_1, α_1, α_2, and β, the measurement fidelity of Q_L (Q_R) is estimated as 94 % (88.8 %). We claim that the fidelities can further be higher if the FPGA-based readout is applied because the large peak separation would allow faster single-shot measurements with faster tunneling rates which would result in less relaxation due to lower τ_{out}/T_1.

Supplementary Note 3.7. Leakage error analysis due to Landau-Zener transition

We estimate the Landau-Zener transition probability during the fast ramp time by solving the time-dependent Schrodinger equation with the typical ST_0 qubit Hamiltonian [7]. We put the measured parameters such as the tunnel coupling strength, pulse rise time, pulse amplitude, and the magnetic field differences into the numerical simulation, and obtained the time trace of (2,0)S along the evolution time up to 10 ns. As the decoherence of the system is not considered in the simulation, the resultant trace (Supplementary Fig. 3.7) exhibits non-decaying oscillatory behavior in the 0 ~ 3% range which averages to 1.7%. We therefore conclude that the leakage probability and its effect to the visibility is not significant.

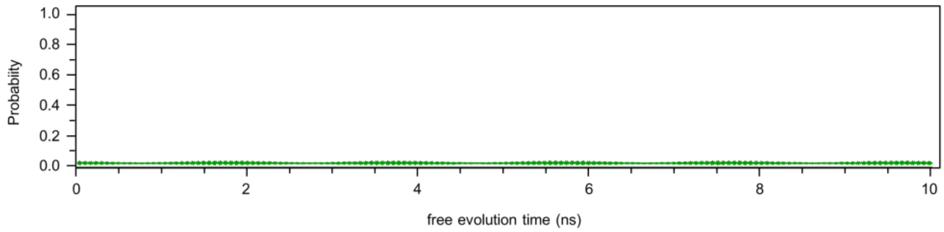

Supplementary Figure 3.7 The (2,0)S probability along the free evolution time. Time evolution of the (2,0)S state probability under the typical ST_0 qubit Hamiltonian is numerically obtained by putting the experimental parameters. The simulation yields 1.7% (2,0)S average occupation probability during the qubit manipulation time.

Supplementary Note 3.8. Measurement setup

A rf-single electron transistor (rf-set) sensor is operated to detect the charge states of the ST_0 qubits in our device. For the rf-reflectometry, impedance matching tank circuit as shown in Supplementary Fig. 3.8 is attached to the rf-ohmic contact of the device, and the 100 pF capacitor is connected in series to the other ohmic contact (depicted on the micromagnet) to serve as a rf-ground. With the inductor value L = 1500 nH and the parasitic capacitance C_p = 1.4 pF of the circuit board, the resonance frequency is about 110MHz, and the impedance matching occurs at rf-set sensor resistance approximately 0.5 h/e^2 where h is Plank's constant and e is the electron charge. A commercial high frequency lock-in amplifier (Zurich Instrument, UHFLI) is used as the carrier generator, rf demodulator for the homodyne detection, and further signal processing such as gated integration and timing marker generation. Carrier power of -40dBm power is generated at room temperature and attenuated through the attenuators and the directional coupler by -50 dB in the input line. The reflected signal is first amplified by 25 dB with commercial cryogenic amplifier (Caltech Microwave Research Group, CITLF2), and further amplified by 50 dB at room temperature using a home-made low-noise rf amplifier. Demodulated signal is acquired with a data acquisition card (National Instruments, NI USB-9215A) for raster scanning and also boxcar-averaged with the gated integrator module in the UHFLI for the correlated double sampling described above. For single-shot readout, the CDS output is counted with a high-speed commercial photon counter (Stanford Research Systems, SR400 dual gated photon counter). A commercial multichannel scalar (Stanford Research Systems, SR430 multichannel scaler & average) is also used for time correlated pulse counting for tunneling rate calibration.

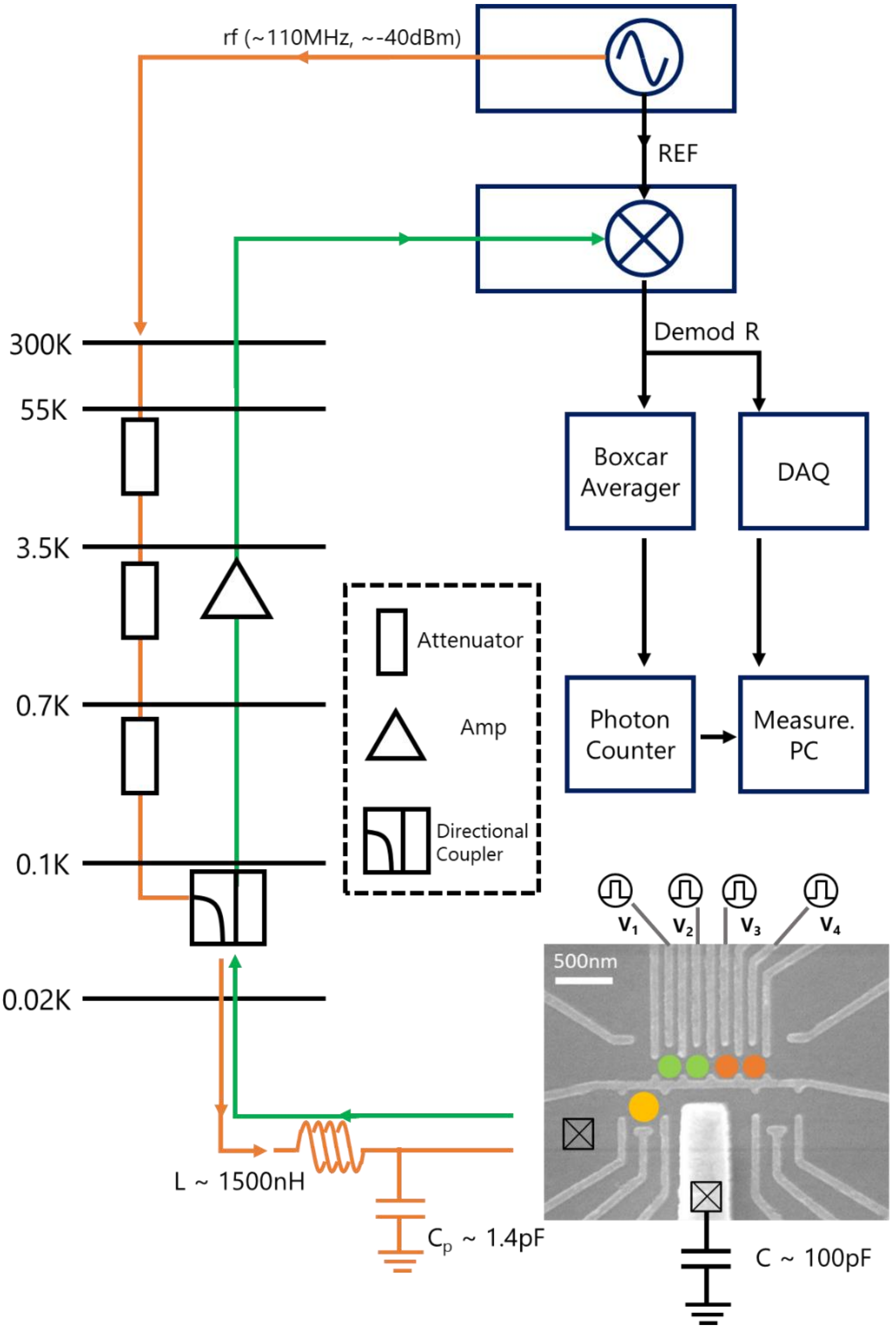

Supplementary Figure 3.8 The measurement setup for radio frequency (rf)-reflectometry, and the signal block diagram. Impedance matching tank-circuit (L~1500 nH, C_p ~ 1.4pF) is attached to the rf-set sensor Ohmic contact for homodyne detection. Orange (green) line indicates the input (reflected) signal.

Reflected signal is demodulated and processed for single-shot event counting as shown in the block diagram.

Supplementary References

[1] P. Elleaume, O. Chubar, and J. Chavanne, Computing 3D magnetic fields from insertion devices. in *Proceedings of the 1997 Particle Accelerator Conference (Cat. No.97CH36167)* vol. 3 3509–3511 (1997).

[2] O. Chubar, P. Elleaume, and J. Chavanne, A three-dimensional magnetostatics computer code for insertion devices. *J. Synchrotron Rad.* **5**, 481–484 (1998).

[3] J. J. Pla *et al.* A single-atom electron spin qubit in silicon. *Nature* **489**, 541–545 (2012).

[4] C. Barthel, D. J. Reilly, C. M. Marcus, M. P. Hanson, and A. C. Gossard, Rapid single-shot measurement of a singlet-triplet qubit. *Phys. Rev. Lett.* **103**, 160503 (2009).

[5] T. Nakajima *et al.* Robust single-shot spin measurement with 99.5% fidelity in a quantum dot array. *Phys. Rev. Lett.* **119**, 017701 (2017).

[6] A. Morello *et al.* Single-shot readout of an electron spin in silicon. *Nature* **467**, 687–691 (2010).

[7] D. Stepanenko, M. Rudner, B. I. Halperin, and D. Loss, Singlet-triplet splitting in double quantum dots due to spin-orbit and hyperfine interactions. *Phys. Rev. B* **85**, 075416 (2012).

Chapter 4. Approaching ideal visibility in singlet-triplet qubit operations using energy selective tunneling-based Hamiltonian estimation

Abstract

We report energy selective tunneling readout-based Hamiltonian parameter estimation of a two-electron spin qubit in a GaAs quantum dot array. Optimization of readout fidelity enables a single-shot measurement time of 16 μs on average, with adaptive initialization and efficient qubit frequency estimation based on real-time Bayesian inference. For qubit operation in a frequency heralded mode, we observe a 40-fold increase in coherence time without resorting to dynamic nuclear polarization. We also demonstrate active frequency feedback with quantum oscillation visibility, single-shot measurement fidelity, and gate fidelity of 97.7%, 99%, and 99.6%, respectively, showcasing the improvements in the overall capabilities of GaAs-based spin qubits. By pushing the sensitivity of the energy selective tunneling-based spin to charge conversion to the limit, the technique is useful for advanced quantum control protocols such as error mitigation schemes, where fast qubit parameter calibration with a large signal-to-noise ratio is crucial.

This chapter is adapted from *Physical Review Letters* **129**, 040501 (2022).

The efficient and precise characterization of a quantum system is important for building scalable quantum technologies that are robust to noise stemming from a fluctuating environment [1,2]. Estimating Hamiltonian parameters faster than the characteristic noise fluctuation time scale is essential, where knowledge gained from the measurement is used for correcting control parameters [2-4]. Active measurement-based feedback for example is used to enhance quantum sensing [5,6]. For semiconductor quantum dot (QD)-based spin qubit platforms, Hamiltonian parameter estimation applied to GaAs has shown that the effect of quasi-static nuclear spin fluctuation can be strongly suppressed for both single spin [7] and singlet-triplet qubits [2]. While the development of spin qubits in nuclear noise-free group-IV materials such as ^{28}Si shows impressive progress in increasing single spin qubit coherence times [8,9], two-qubit control fidelity is often impeded by charge noise, which is also often sufficiently non-Markovian [10] and hence suppressible. Thus, fast Hamiltonian learning methods are expected to be used for a wide range of materials in noisy intermediate-scale quantum systems.

The fast single-shot measurement of qubits with high fidelity is a prerequisite for enabling Hamiltonian estimation. Semiconductor spin qubit devices mostly utilize a nearby charge sensor, where spin states are distinguished via spin to charge conversion mechanisms such as energy selective tunneling (EST) [11,12] or Pauli spin blockade (PSB) [13]. While both mechanisms are applicable for the detection of single spin [11], singlet-triplet (ST_0) [13], and exchange only qubits [14], PSB-based readout has been predominantly used for real-time Hamiltonian estimation owing to its deterministic readout time and fast initialization capability [15]. However, direct application of PSB often suffers from small signal contrast due to sub-optimal sensor position relative to double quantum dot (DQD) or fast relaxation at the readout condition due to large magnetic field difference-induced singlet state tunneling or the effect of spin-orbit coupling [16]. Variants of PSB-based readout have been developed using electron latching mechanisms in sufficiently isolated quantum dots [17,18] or by mapping to states outside the qubit space [19] circumventing some of the PSB-readout's known disadvantages. For Si devices, high readout visibility has been demonstrated using both PSB and EST readout owing to relatively long relaxation time [20-22]. However, so far the experiments using GaAs devices showed visibility below 80% using PSB readout.

The EST-based single-shot readout, on the other hand, guarantees a signal contrast corresponding to a full electron charge and long relaxation time [23,24]. As the Hamiltonian learning efficiency is directly affected by the ideality of the likelihood function, the large signal-to-noise ratio (SNR) of the EST readout can potentially be used for real-time Hamiltonian parameter estimation. Because the EST readout suffers from the intrinsically probabilistic nature of electron tunneling, requiring a longer waiting time than the PSB readout [25], it is important to determine whether the current state-of-the-art sensitivity of the RF-charge sensor can provide an EST readout that is sufficiently fast and simultaneously has a large SNR to enable efficient qubit frequency estimation on the fly.

In this Letter, we demonstrate real-time Hamiltonian parameter estimation by EST-based single-shot readout with sub-MHz accuracy in qubit frequency verified by observing over a 40-fold increase in coherence time T_2* compared to that of bare evolution on the order of 20 ns in GaAs [13]. With frequency feedback, the single-qubit operation performance in terms of initialization, manipulation, and measurement fidelity is one of the best figures reported thus far for semiconductor spin qubits, providing a promising route for applying the EST-based single-shot readout method to various qubit operations.

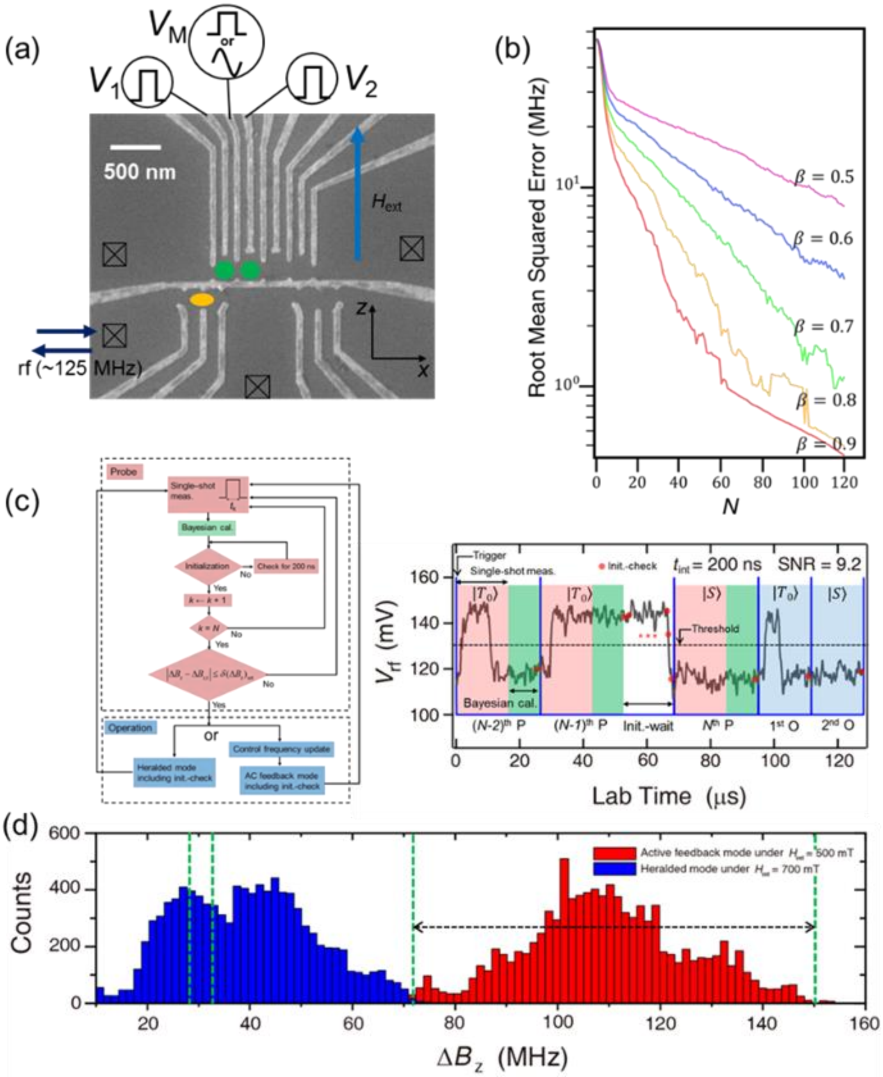

Figure 4.1 (a) Scanning electron microscopy image of a device similar to the one used in the experiment. Green (yellow) circles indicate the position of quantum dots for the ST_0 qubit (RF charge sensor. H_{ext} is applied to the z-axis as indicated by the blue arrow. **(b)** Root mean squared error of the Bayesian estimator as a function of N and β. **(c)** Left panel: block diagram of the experimental procedure including the probe and operation step, where the latter is performed either in heralded or active feedback mode. Right panel: example scope trace of the charge sensor signal

recorded during the experiment. Gray trace: RF-demodulated sensor signal with SNR = 9.2 at t_{int} =200 ns. Blue trace: trigger signals marking the start timings of each probe and operation step. The red dots show the timings of the initialization check sequences. **(d)** Histograms of ΔB_Z obtained by running the probe step 10000 times at two different H_{ext}. For the heralded (active feedback) mode, $\delta(\Delta B_Z)_{set}$ on the order of 1 MHz (few tens of MHz) around an average ΔB_Z of 30 (110) MHz was chosen. Green dashed lines indicate a tolerance window $2\delta(\Delta B_Z)_{set}$.

The quantum system we study is an ST_0 qubit with a basis state singlet $\left|S\right\rangle$ and triplet-zero $\left|T_0\right\rangle$, formed by two gate-defined lateral QDs. Fig. 4.1(a) shows a scanning electron microscope image of a quantum dot device similar to the one we measured. Au/Ti gate electrodes were deposited on top of the GaAs/AlGaAs heterostructure, where a 2D electron gas is formed 70 nm below the surface. Focusing on the DQD denoted by green circles in Fig. 4.1(a), high-frequency voltage pulses combined with DC voltages through bias tees are input to gates V_1, V_2, and V_M. RF-reflectometry was performed by injecting a carrier frequency of $\approx$125 MHz with an estimated power of -100 dBm at the Ohmic contacts and monitoring the reflected power through homodyne detection. The device was operated in a dilution refrigerator with base temperature $\approx$ 7 mK and with an external magnetic field H_{ext}. The measured electron temperature is $\approx$ 72 mK [26-28].

The qubit Hamiltonian is given by $H = \frac{J(\varepsilon)}{2}\sigma_z + \frac{\Delta B_z}{2}\sigma_x$, where $J(\varepsilon)$ is the exchange splitting between states $\left|S\right\rangle$ and $\left|T_0\right\rangle$ controlled by potential detuning ε, $\sigma_{i = x, y, z}$ is the Pauli matrix, and ΔB_z is the magnetic field difference between QDs set by the hyperfine interaction with the host Ga and As nuclei. We adopted units where $g^* \mu_B/h = 1$, in which $g^* \approx -0.44$ is the effective gyromagnetic ratio in GaAs, μ_B is the Bohr magneton, and h is Planck's constant. With the quantum control provided by rapidly turning on and off $J(\varepsilon)$, the main task is to estimate ΔB_z, which varies randomly in time owing to statistical fluctuations of the nuclei. The basic idea of the Bayesian inference is to update one's knowledge about the Hamiltonian parameter by comparing the measurement results with the expected form of time evolution (likelihood function). Based on the single-shot projective measurement of the qubit evolving around the x-axis on the Bloch sphere for time $t_k = 4k$ ns (Larmor oscillation), Bayesian inference is performed by the following rule up to a normalization constant [2]:

$$P(\Delta B_z \mid m_N, m_{N-1}, \ldots m_1) = P_0(\Delta B_z) \prod_{k=1}^{N} \frac{1}{2}[1 + r_k(\alpha + \beta \cos(2\pi \Delta B_z t_k))] \qquad (1)$$

where N is the number of single-shot measurements per Hamiltonian estimation, $P_0(\Delta B_Z)$ is the uniform initial distribution, $r_k = 1$ (-1) for $m_k = |S\rangle (|T_0\rangle)$, and α (β) is the parameter determined by the axis of rotation (oscillation visibility). After the N^{th} single-shot measurement and update, the most probable ΔB_z is determined from the posterior distribution $P(\Delta B_Z \mid m_N, m_{N-1}, \ldots, m_1)$.

In the likelihood function $\frac{1}{2}[1 + r_k(\alpha + \beta \cos(2\pi \Delta B_z t_k))]$, ideally, $\alpha = 0$ and $\beta = 1$. Fig. 4.1(b) shows the simulation results of the root mean squared error between the true and estimated ΔB_z. Compared to the low-visibility case ($\beta = 0.5$) corresponding to a large measurement error, the high-visibility case ($\beta = 0.9$) shows a large improvement in the rate of convergence, reaching sub-MHz accuracy in less than N = 70. To date, Bayesian estimations of quantum dot spin qubits have been performed with β~0.7 [2,7] requiring N > 120 for practical Hamiltonian estimation. Below, we show that the EST readout indeed provides β reaching unity enabling efficient frequency detection and feedback.

Fig. 4.1(c) shows a schematic block diagram and an example scope trace during the experiment. We set the integration time of the RF demodulator t_{int} = 200 ns, at which SNR = 9.2 [24,26,29-33]. The measurement time was set to 15 μs, during which the dot-to-reservoir tunnel rate tuned to the order of 1 MHz ensures that a tunnel-out event occurs for the state $\left|T_0\right\rangle$. For the probe sequence, we diabatically pulse ε to rapidly turn off J. The calculation time according to Eq. (1) is $\approx$10 μs after the k^{th} measurement. For the operation, there are two types of modes. The first is heralded mode where the operation is conditionally triggered only when the estimated qubit frequency in the probe step falls within a preset tolerance $\delta(\Delta B_{\mathrm{Z}})_{\mathrm{set}}$ around the target frequency $\Delta B_{\mathrm{z.t}}$. Once a short operation on the order of 20 shots is finished, one has to wait for the next $\Delta B_{\mathrm{z.t}} \pm \delta(\Delta B_{\mathrm{Z}})_{\mathrm{set}}$ to happen. The method is conceptually similar to Ref. [34] where the Bayesian estimator-based heralding was used to effectively suppress thermally induced initialization error. The second is the active feedback mode where resonant modulation of $J(\varepsilon)$ (Rabi oscillation) is performed using the frequency obtained from the probe step. Here, $\delta(\Delta B_{\mathrm{Z}})_{\mathrm{set}}$ is typically set to more than 70 MHz and the control frequency is actively adjusted so that the waiting time is minimized. In all steps, we apply an adaptive initialization step [34,35] where the controller triggers the next experiment provided that the state is $|S\rangle$. Including all the latency components, the repetition period for one probe (operation) step is approximately 26 (16) μs on average [26]. Fig. 4.1(d) shows typical histograms of ΔB_z obtained by repeatedly running the probe step at different H_{ext}, showing fluctuation about a non-zero mean ΔB_z. Note that the average ΔB_z depends on H_{ext}. While the exact origin of this is not well understood to date, previous studies in GaAs quantum dot report similar behavior [36,37], and we adjust H_{ext} to set the most probable ΔB_z about 30 MHz (110 MHz) for the heralded (active feedback) mode.

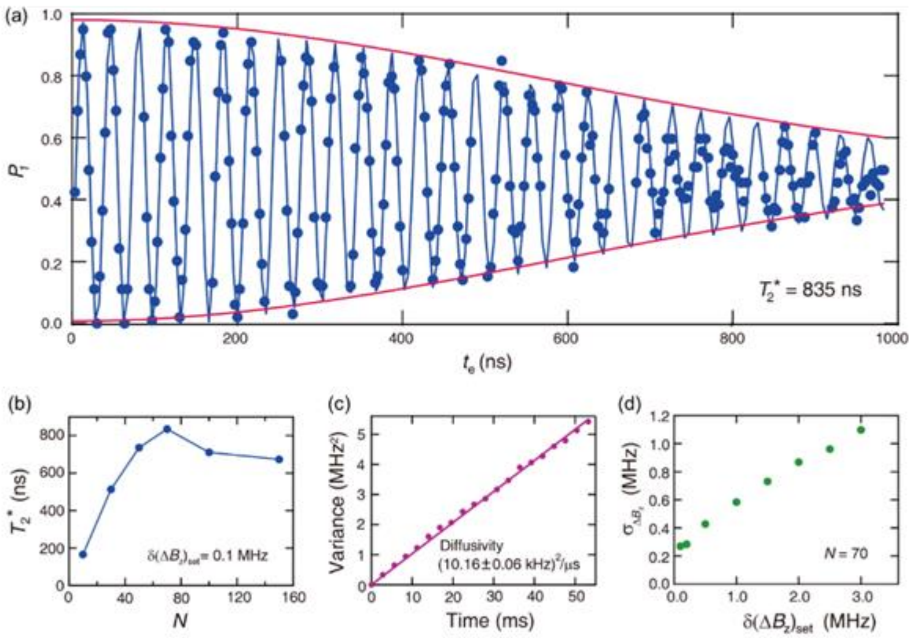

Figure 4.2 (a) Representative Larmor oscillations with N = 70 showing T_2* = 835 ns, with a fit to a Gaussian decay function (red envelope and blue oscillatory fit). **(b)** T_2* as a function of N, showing an optimal N = 70 with $\delta(\Delta B_Z)_{set}$ = 0.1 MHz. **(c)** The variance of the ΔB_z as a function of elapsed time showing a diffusion process with the diffusivity (10.16 ± 0.06 kHz)^2/μs. **(d)** The uncertainty of the frequency estimation $\sigma_{\Delta Bz}$ as a function of the half-width of the tolerance $\delta(\Delta B_Z)_{set}$.

First, we demonstrate the performance of the EST-based Bayesian estimator using the heralded mode operation. Fig. 4.2(a) shows the representative Larmor oscillations where P_1 is the triplet return probability with N = 70, $\Delta B_{z,t}$ = 30 MHz, and $\delta(\Delta B_Z)_{set}$ = 0.1 MHz. The measurement of $T_2^*(N)$, extracted by fitting the Larmor oscillations to a Gaussian decay, reveals the uncertainty of the EST-Bayesian estimation (Fig. 4.2(b)). The initial increase in $T_2^*(N)$ corresponds to an improvement in the estimation accuracy. T_2^* reaches an optimal coherence time of over 800 ns near N = 70 and subsequently decreases for N > 80. The latter reflects the effect of nuclear fluctuation during the increased estimation period consistent with the diffusive behavior of ΔB_z with diffusivity D = 10.16 kHz^2/μs (Fig. 4.2(c)) [2].

Fig. 4.2(d) shows the $\delta(\Delta B_Z)_{set}$ dependence of the experimental estimation uncertainty $\sigma_{\Delta Bz} = 1/(\sqrt{2}\pi T_2^*)$ [38]. As we set the tolerance more stringently (smaller $\delta(\Delta B_Z)_{set}$), T_2^* increases correspondingly. The residual uncertainty of the EST-based Bayesian estimator when $\delta(\Delta B_Z)_{set}$ = 0 is approximately 0.25 MHz. It is likely overestimated by the nuclear fluctuation during the operation time of 0.32 ms (16 μs× 20 shots) after the probe step. Thus, we conclude that our Hamiltonian estimation scheme enables qubit frequency estimation in 70 shots with an accuracy better than 0.25 MHz. Note also that while the maximum T_2^* = 835 ns we observe is less than the PSB-based Hamiltonian estimation [2], the actual performance of the PSB and EST-based Bayesian estimators is difficult to directly compare so far because the dynamic nuclear polarization [3,39] is not used in the current experiment.

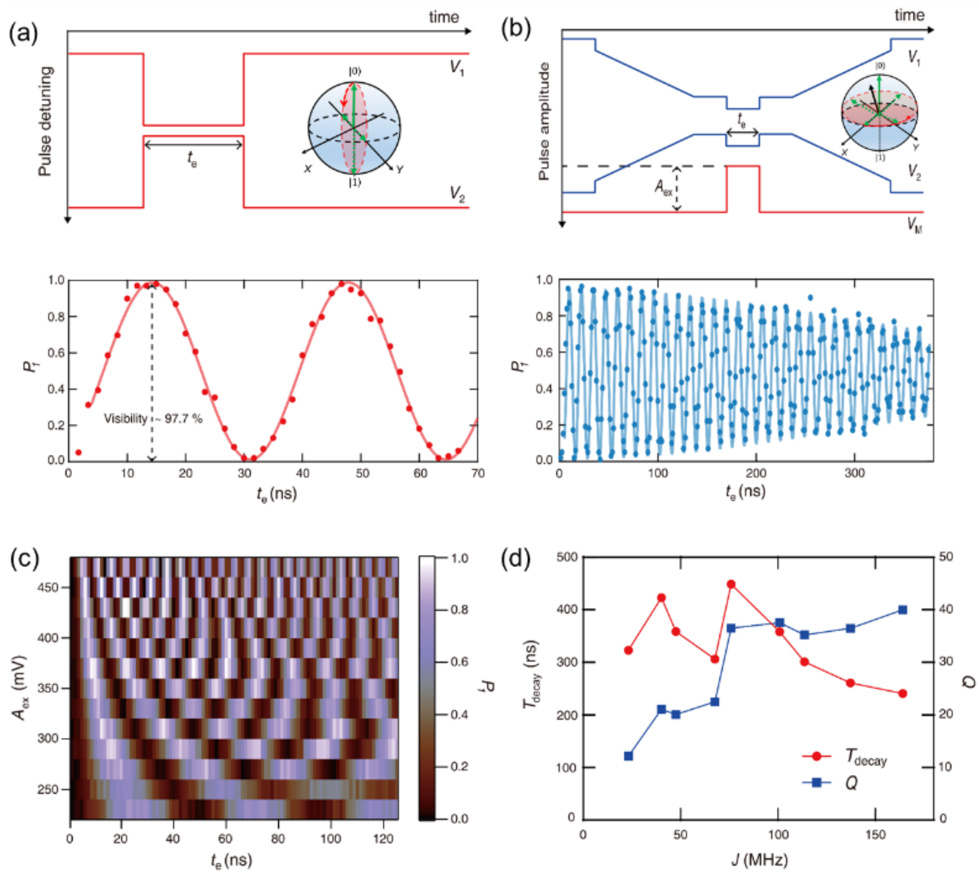

Figure 4.3 (a) Top: Pulse sequences applied to gates V_1 and V_2 for the heralded Larmor oscillations measurement. Bottom: Larmor oscillations with visibility higher than 97% **(b)** Top: Pulse sequence for coherent exchange operation. Bottom: Corresponding exchange oscillations at $J = 75$ MHz, $\Delta B_{z,t} = 30$ MHz showing charge noise-limited coherence time $T_{decay} = 450$ ns. **(c)** Exchange oscillations as a function of barrier pulse amplitude A_{ex} and evolution time t_e. **(d)** T_{decay} and the quality factor Q as a function of exchange coupling J.

We now discuss the application of the EST-based Hamiltonian estimation to general single-qubit operations (Fig. 4.3: heralded mode, Fig. 4.4: active feedback mode). Fig. 4.3(a) shows coherent Larmor oscillations with $\Delta B_{z,t}$ = 30 MHz. The oscillation shows the visibility of approximately 97.7%. Considering possible imperfections in the control stemming from residual J and finite rise time of the waveform generator (~0.4 ns), the result shows that the EST-based Bayesian method enables accurate qubit frequency estimation and high measurement fidelity at the same time, leading to near ideal visibility. By comparing the oscillation with the numerical simulation, we estimate measurement fidelity of 99% with less than 0.1% initialization errors for the heralded mode [23,26,40,41].

Using symmetric barrier-pulse operation, recently demonstrated in Ref. [42], Fig. 4.3(b) shows coherent exchange oscillations with $\Delta B_{z,t}$ = 30 MHz, and J = 75 MHz. In addition, a two-dimensional map of the exchange oscillations is measured as a function of exchange amplitude A_{ex} and exchange duration t_e (Fig. 4.3(c)), showing the oscillations with a high-quality factor Q. Moreover, $Q(J)$ follows the general trend observed in previous results [42] where Q (T_{decay}) tends to saturate (decrease) at large J owing to the crossover from nuclear noise to electrical noise-limited decoherence. While the maximum Q of ~40 is comparable to that in the previous report [42], our EST-based Bayesian method effectively suppresses the ΔB_z fluctuation, leading to the observation of Q > 30 in a wide range of J.

Although the heralded mode operation exemplifies the performance of the EST-based Hamiltonian estimator with minimal overhead in the Bayesian circuit, the main drawback is the low duty cycle (actual operation/waiting time), which can be < 1% depending on the tolerance. Thus we further develop our methodology using ac-driven qubit operation in active feedback mode. The pulse sequence for qubit operation is the same as in Fig. 4.3(b) except that a sinusoidal RF pulse is applied to V_M using the frequency detected in the probe step. In this manner, the total waiting time is reduced down to one probe step (70 shots x 26 μs = 1.82 ms). Fig. 4.4(a) shows the coherent Rabi oscillation measured as a function of the RF pulse duration and controlled detuning δf. The pulse amplitude A_{RF} is chosen to maximize the Q factor $Q_{Rabi} = f_{Rabi}T_{Rabi} \sim 12$ with the Rabi frequency f_{Rabi} of 6.05 MHz and the Rabi decay time T_{Rabi} of 1.71 μs (inset to Fig. 4.4(a)). The oscillation visibility reaches approximately 97.6 %, (Fig. 4.4(b)). This near-ideal visibility of the RF-driven oscillation even without dynamic nuclear polarization again reveals the precise qubit frequency estimation and high measurement fidelity simultaneously enabled by the EST-based Bayesian estimator.

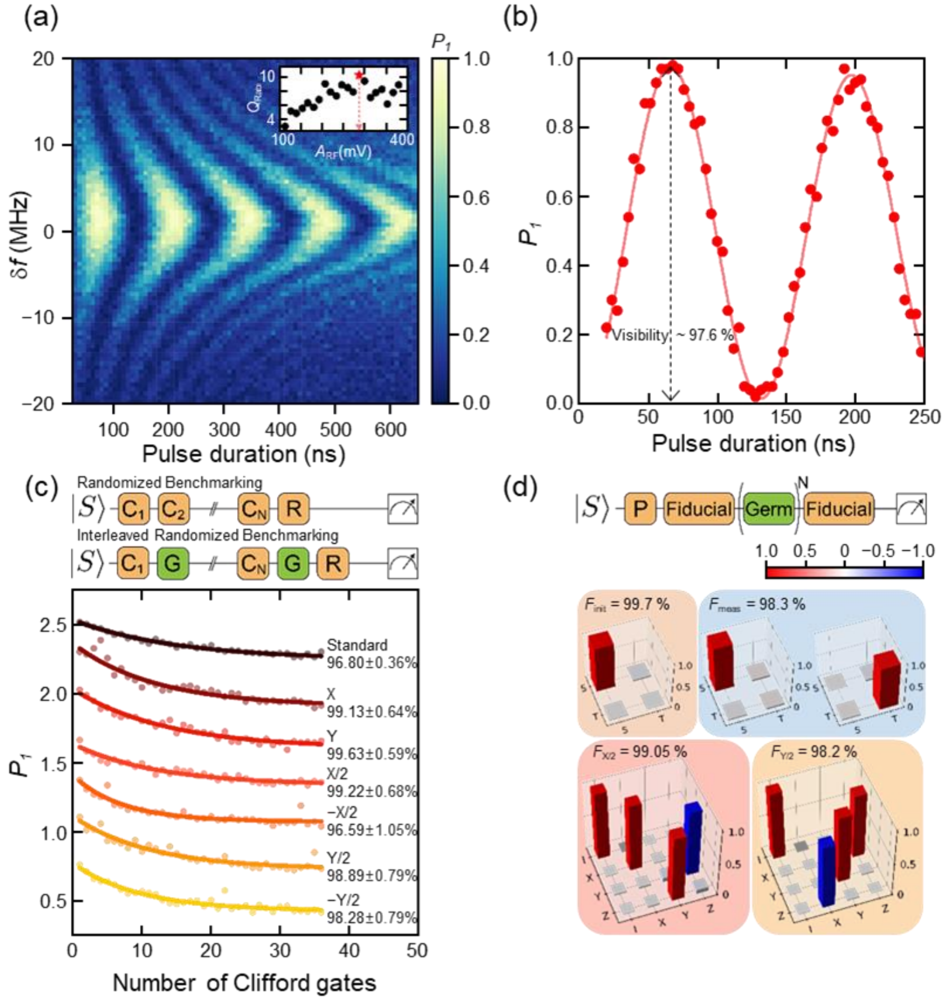

Figure 4.4 (a) Rabi oscillation of P_1 as a function of controlled detuning δf and pulse duration. Inset: Oscillation quality factor Q_{Rabi} as a function of RF amplitude A_{RF} (measured at the output of the signal generator). The red symbol marks the condition for the maximum Q_{Rabi}. **(b)** Representative Rabi oscillation with visibility higher than 97 %. The oscillation is fit to the sinusoidal function with the Gaussian envelope, from which Rabi decay time $T_{\mathrm{Rabi}} = 1.71$ μs is obtained. **(c)** P_1 as a function of the number of random Clifford gates obtained from a single qubit standard and interleaved randomized benchmarking. Traces are offset by 0.3 for clarity. **(d)** Density matrices (top row) and Pauli transfer matrices (bottom row) evaluated by gate set tomography.

Furthermore, we perform the standard randomized benchmarking (RB) and interleaved randomized benchmarking (IRB) where single-qubit gates X, Y, X/2, Y/2, −X/2, and −Y/2 are interleaved to random Clifford gates [43-45]. The recovery gate is chosen such that the final state is ideally singlet, and the gate fidelity is obtained by fitting the measured data to the exponentially decaying curve [26,45]. We find the average gate fidelity F_{avg} of 96.80 % and π-pulse fidelity F_{X} of 99.13 %, the latter being close to the Q-factor limited value $\exp(-1/(2Q_{\mathrm{Rabi}})^2)$= 99.76% ± 0.03 %.

To compare the state preparation and measurement (SPAM) errors between two operation modes, we perform gate-set tomography (GST) [41]. Fig. 4.4(d) shows the density matrix (top row) and the Pauli transfer matrix (PTM, bottom row), obtained using a single qubit GST protocol with a gate set {I, X/2, and Y/2}2 [26,46], from which we obtain $F_{\mathrm{X/2}}$ = 99.05 % and $F_{\mathrm{Y/2}}$ = 98.2 %, consistent with the values obtained from the IRB. The GST yields the initialization fidelity of 99.7% and measurement fidelity of 98.3%. We ascribe slightly lower initialization and measurement fidelity for the active feedback mode-based GST compared to the heralded mode to a combination of an additional leakage probability through S-T_+ anticrossing while preparing (projecting) a state on the x(z)-axis of the Bloch sphere and the increased relaxation probability during the idle time between the discrete gates. Nevertheless, these results consolidate the high gate fidelity and low SPAM error illustrating that our Hamiltonian estimation enables the real-time application of general qubit operations in GaAs with the fidelities reaching the level of singlet-triplet qubits in Si devices [47].

In conclusion, using energy selective tunneling readout-based Hamiltonian parameter estimation of an ST_0 qubit in GaAs, we demonstrated passive and active suppression of nuclear noise, leading to T_2* above 800 ns, near-ideal quantum oscillation visibility, and gate fidelity up to 99.6% confirmed by both RB and GST comparable with recently demonstrated optimal control-based gate fidelity [48]. The work showcases the improvements in the overall capabilities of GaAs-based spin qubits. With the large SNR of the charge sensor and real-time capability, the EST-based Hamiltonian estimation is potentially useful for advanced quantum control protocols with affordable overhead in classical signal processing, such as error mitigation schemes and entanglement demonstration experiments, where fast qubit parameter calibration with large readout visibility is essential [35].

References

[1] C. Ferrie, C. Granade, G. Paz-Silva, and H. M. Wiseman, Bayesian quantum noise spectroscopy, *New J. Phys.* **20,** 123005 (2018).

[2] M. D. Shulman, S. P. Harvey, J. M. Nichol, S. D. Bartlett, A. C. Doherty, V. Umansky, and A. Yacoby, Suppressing qubit dephasing using real-time Hamiltonian estimation, *Nat. Commun.* **5,** 5156 (2014).

[3] H. Bluhm, S. Foletti, D. Mahalu, V. Umansky, and A. Yacoby, Enhancing the Coherence of a Spin Qubit by Operating it as a Feedback Loop That Controls its Nuclear Spin Bath, *Phys. Rev. Lett.* **105,** 216803 (2010).

[4] A. Sergeevich, A. Chandran, J. Combes, S. D. Bartlett, and H. M. Wiseman, Characterization of a qubit Hamiltonian using adaptive measurements in a fixed basis, *Phys. Rev. A* **84,** 052315 (2011).

[5] G. Waldherr *et al.*, High-dynamic-range magnetometry with a single nuclear spin in diamond, *Nat. Nanotech.* **7,** 105 (2012).

[6] N. M. Nusran, M. U. Momeen, and M. V. G. Dutt, High-dynamic-range magnetometry with a single electronic spin in diamond, *Nat. Nanotech.* **7,** 109 (2012).

[7] T. Nakajima *et al.*, Coherence of a Driven Electron Spin Qubit Actively Decoupled from Quasistatic Noise, *Phys. Rev. X* **10,** 011060 (2020).

[8] M. Veldhorst *et al.*, An addressable quantum dot qubit with fault-tolerant control-fidelity, *Nat. Nanotech.* **9,** 981 (2014).

[9] J. Yoneda *et al.*, A quantum-dot spin qubit with coherence limited by charge noise and fidelity higher than 99.9%, *Nat. Nanotech.* **13,** 102 (2018).

[10] O. E. Dial, M. D. Shulman, S. P. Harvey, H. Bluhm, V. Umansky, and A. Yacoby, Charge Noise Spectroscopy Using Coherent Exchange Oscillations in a Singlet-Triplet Qubit, *Phys. Rev. Lett.* **110,** 146804 (2013).

[11] J. M. Elzerman, R. Hanson, L. H. W. van Beveren, B. Witkamp, L. M. K. Vandersypen, and L. P. Kouwenhoven, Single-shot read-out of an individual electron spin in a quantum dot, *Nature* **430,** 431 (2004).

[12] R. Hanson, L. H. W. van Beveren, I. T. Vink, J. M. Elzerman, W. J. M. Naber, F. H. L. Koppens, L. P. Kouwenhoven, and L. M. K. Vandersypen, Single-shot readout of electron spin states in a quantum dot using spin-dependent tunnel rates,

Phys. Rev. Lett. **94,** 196802 (2005).

[13] J. R. Petta, A. C. Johnson, J. M. Taylor, E. A. Laird, A. Yacoby, M. D. Lukin, C. M. Marcus, M. P. Hanson, and A. C. Gossard, Coherent manipulation of coupled electron spins in semiconductor quantum dots, *Science* **309,** 2180 (2005).

[14] J. Medford *et al.*, Self-consistent measurement and state tomography of an exchange-only spin qubit, *Nat. Nanotech.* **8,** 654 (2013).

[15] C. Barthel, D. J. Reilly, C. M. Marcus, M. P. Hanson, and A. C. Gossard, Rapid Single-Shot Measurement of a Singlet-Triplet Qubit, *Phys. Rev. Lett.* **103,** 4 (2009).

[16] C. Barthel, J. Medford, H. Bluhm, A. Yacoby, C. M. Marcus, M. P. Hanson, and A. C. Gossard, Relaxation and readout visibility of a singlet-triplet qubit in an Overhauser field gradient, *Phys. Rev. B* **85,** 7 (2012).

[17] P. Harvey-Collard *et al.*, High-Fidelity Single-Shot Readout for a Spin Qubit via an Enhanced Latching Mechanism, *Phys. Rev. X* **8,** 021046 (2018).

[18] T. Nakajima *et al.*, Robust Single-Shot Spin Measurement with 99.5% Fidelity in a Quantum Dot Array, *Phys. Rev. Lett.* **119,** 017701 (2017).

[19] L. A. Orona, J. M. Nichol, S. P. Harvey, C. G. L. Bottcher, S. Fallahi, G. C. Gardner, M. J. Manfra, and A. Yacoby, Readout of singlet-triplet qubits at large magnetic field gradients, *Phys. Rev. B* **98,** 125404 (2018).

[20] K. Eng *et al.*, Isotopically enhanced triple-quantum-dot qubit, *Sci. Adv.* **1,** 7 (2015).

[21] L. A. Tracy, D. R. Luhman, S. M. Carr, N. C. Bishop, G. A. Ten Eyck, T. Pluym, J. R. Wendt, M. P. Lilly, and M. S. Carroll, Single shot spin readout using a cryogenic high-electron-mobility transistor amplifier at sub-Kelvin temperatures, *Appl. Phys. Lett.* **108,** 5 (2016).

[22] J. P. Dehollain *et al.*, Optimization of a solid-state electron spin qubit using gate set tomography, *New J. Phys.* **18,** 9 (2016).

[23] W. Jang, J. Kim, M. K. Cho, H. Chung, S. Park, J. Eom, V. Umansky, Y. C. Chung, and D. Kim, Robust energy-selective tunneling readout of singlet-triplet qubits under large magnetic field gradient, *npj Quant. Inf.* **6,** 7 (2020).

[24] D. Keith, M. G. House, M. B. Donnelly, T. F. Watson, B. Weber, and M. Y. Simmons, Single-Shot Spin Readout in Semiconductors Near the Shot-Noise Sensitivity Limit, *Phys. Rev. X* **9,** 041003 (2019).

[25] D. Keith, S. K. Gorman, L. Kranz, Y. He, J. G. Keizer, M. A. Broome, and M. Y. Simmons, Benchmarking high fidelity single-shot readout of semiconductor qubits, *New J. Phys.* **21,** 063011 (2019).

[26] see Supplementary Materials 4.

[27] I. Ahmed, A. Chatterjee, S. Barraud, J. J. L. Morton, J. A. Haigh, and M. F. Gonzalez-Zalba, Primary thermometry of a single reservoir using cyclic electron tunneling to a quantum dot, *Communications Physics* **1,** 66 (2018).

[28] C. P. Scheller, S. Heizmann, K. Bedner, D. Giss, M. Meschke, D. M. Zumbuhl, J. D. Zimmerman, and A. C. Gossard, Silver-epoxy microwave filters and thermalizers for millikelvin experiments, *Appl. Phys. Lett.* **104,** 5 (2014).

[29] J. Stehlik, Y. Y. Liu, C. M. Quintana, C. Eichler, T. R. Hartke, and J. R. Petta, Fast Charge Sensing of a Cavity-Coupled Double Quantum Dot Using a Josephson Parametric Amplifier, *Phys. Rev. Appl.* **4,** 014018 (2015).

[30] Y. Makhlin, G. Schon, and A. Shnirman, Quantum-state engineering with Josephson-junction devices, *Rev. Mod. Phys.* **73,** 357 (2001).

[31] C. Barthel, D. J. Reilly, C. M. Marcus, M. P. Hanson, and A. C. Gossard, Rapid Single-Shot Measurement of a Singlet-Triplet Qubit, *Phys. Rev. Lett.* **103,** 160503 (2009).

[32] C. Barthel, M. Kjaergaard, J. Medford, M. Stopa, C. M. Marcus, M. P. Hanson, and A. C. Gossard, Fast sensing of double-dot charge arrangement and spin state with a radio-frequency sensor quantum dot, *Phys. Rev. B* **81,** 161308 (2010).

[33] A. Noiri, K. Takeda, J. Yoneda, T. Nakajima, T. Kodera, and S. Tarucha, Radio-Frequency-Detected Fast Charge Sensing in Undoped Silicon Quantum Dots, *Nano Lett.* **20,** 947 (2020).

[34] M. A. I. Johnson, M. T. Mądzik, F. E. Hudson, K. M. Itoh, A. M. Jakob, D. N. Jamieson, A. Dzurak, and A. Morello, Beating the thermal limit of qubit initialization with a Bayesian 'Maxwell's demon', *arXiv:* **2110**.02046 (2021).

[35] J. P. Dehollain *et al.*, Bell's inequality violation with spins in silicon, *Nat. Nanotechnol.* **11,** 242 (2016).

[36] F. K. Malinowski *et al.*, Spectrum of the Nuclear Environment for GaAs Spin Qubits, *Phys. Rev. Lett.* **118,** 177702 (2017).

[37] H. F. Qiao, Y. P. Kandel, K. Y. Deng, S. Fallahi, G. C. Gardner, M. J. Manfra,

E. Barnes, and J. M. Nichol, Coherent Multispin Exchange Coupling in a Quantum-Dot Spin Chain, *Phys. Rev. X* **10,** 031006 (2020).

[38] F. H. L. Koppens *et al.*, Control and detection of singlet-triplet mixing in a random nuclear field, *Science* **309,** 5739 (2005).

[39] S. Foletti, H. Bluhm, D. Mahalu, V. Umansky, and A. Yacoby, Universal quantum control of two-electron spin quantum bits using dynamic nuclear polarization, *Nat. Phys.* **5,** 903 (2009).

[40] A. Morello *et al.*, Single-shot readout of an electron spin in silicon, *Nature* **467,** 687 (2010).

[41] R. Blume-Kohout, J. K. Gamble, E. Nielsen, K. Rudinger, J. Mizrahi, K. Fortier, and P. Maunz, Demonstration of qubit operations below a rigorous fault tolerance threshold with gate set tomography, *Nat. Commun.* **8,** 14485 (2017).

[42] F. Martins, F. K. Malinowski, P. D. Nissen, E. Barnes, S. Fallahi, G. C. Gardner, M. J. Manfra, C. M. Marcus, and F. Kuemmeth, Noise Suppression Using Symmetric Exchange Gates in Spin Qubits, *Phys. Rev. Lett.* **116,** 5 (2016).

[43] E. Magesan, J. M. Gambetta, and J. Emerson, Scalable and Robust Randomized Benchmarking of Quantum Processes, *Phys. Rev. Lett.* **106,** 180504 (2011).

[44] E. Magesan, J. M. Gambetta, and J. Emerson, Characterizing quantum gates via randomized benchmarking, *Phys. Rev. A* **85,** 042311 (2012).

[45] E. Magesan *et al.*, Efficient Measurement of Quantum Gate Error by Interleaved Randomized Benchmarking, *Phys. Rev. Lett.* **109,** 080505 (2012).

[46] E. Nielsen, K. Rudinger, T. Proctor, A. Russo, K. Young, and R. Blume-Kohout, Probing quantum processor performance with pyGSTi, *Quantum Science and Technology* **5,** 044002 (2020).

[47] K. Takeda, A. Noiri, J. Yoneda, T. Nakajima, and S. Tarucha, Resonantly Driven Singlet-Triplet Spin Qubit in Silicon, *Phys. Rev. Lett.* **124,** 5 (2020).

[48] P. Cerfontaine, T. Botzem, J. Ritzmann, S. S. Humpohl, A. Ludwig, D. Schuh, D. Bougeard, A. D. Wieck, and H. Bluhm, Closed-loop control of a GaAs-based singlet-triplet spin qubit with 99.5% gate fidelity and low leakage, *Nat. Commun.* **11,** 4144 (2020).

Supplementary Materials 4

S4.1. Measurement setup and FPGA implementation

An RF-single electron transistor (RF-SET) sensor is used to detect the quantum states of the ST_0 qubit. An impedance matching tank circuit as shown in Fig. S4.1 is attached to the RF-ohmic contact of the device. With the inductor value L = 1500 nH and the parasitic capacitance C_p = 1.4 pF of the circuit board, the resonance frequency is about 125 MHz, and the impedance matching occurs when the conductance of the RF-SET sensor is approximately 0.5 h/e^2 where h is Plank's constant and e is the electron charge. A commercial high-frequency lock-in amplifier (Zurich Instrument, UHFLI) is used as the carrier generator, RF-demodulator for the homodyne detection, and further signal processing units such as gated integration and timing marker generation. Carrier power of – 40 dBm is generated at room temperature and further attenuated through the cryogenic attenuators and the directional coupler by -60 dB. The reflected signal is first amplified by 50 dB with a two-stage commercial cryogenic amplifier (Caltech Microwave Research Group, CITLF2 x 2 in series), and further amplified by 25 dB at room temperature using a home-made low-noise RF amplifier.

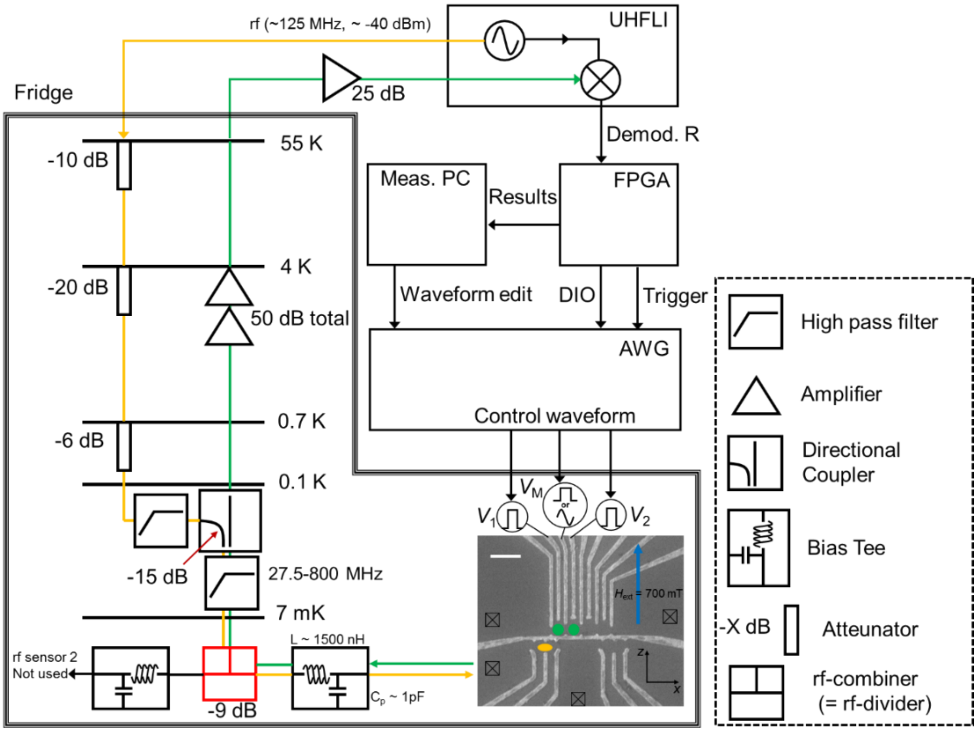

Supplementary Figure S4.1 Measurement setup for radio frequency (RF)-reflectometry and signal block diagram. An impedance matching tank-circuit (L ~1500 nH, C_p ~1.4 pF) is attached to the RF-SET sensor Ohmic contact for homodyne detection. The yellow (green) line indicates the input (reflected) signal. The reflected signal is demodulated in the UHFLI, and subsequently processed in a Field Programmable Gate Array (FPGA) for the EST readout-based Bayesian estimation.

For real-time data processing, we implement a digital logic circuit with a Field Programmable Gate Array board (FPGA, Digilent Zedboard with Zynq-7000 XC7Z020-CLG484). The RF-demodulated analog signal from the UHFLI is input to the 12-bit ad-converter of the FPGA. For single-shot discrimination, the transient tunneling events of the qubit state are thresholded in real-time by comparing the preset threshold value with the data in parallel. The discriminator records bit 1 immediately when data above the threshold value is detected. The bit 0 is recorded when such events did not happen throughout the preset measurement period of 15 μs. The Bayesian estimation after a single shot measurement for the probe step is carried out by calculating the posterior probability distribution for 512 values of ΔB_z between 10 and 160 MHz. We use a look-up table (LUT) storing all the possible values of the likelihood function in the Block RAM inside the FPGA and design a 512-parallelized calculation module to minimize latency due to data processing. After the calculation, the FPGA follows either of the following steps depending on the operation mode. For the heralded mode operation, the user-defined controller triggers the operation step provided that the ΔB_z calculated after the N^{th} Bayesian update is in the range $\Delta B_{z.t} \pm \delta(\Delta B_Z)_{\text{set}}$ where $\Delta B_{z.t}$ is the target frequency and $\delta(\Delta B_Z)_{\text{set}}$ is the preset tolerance. For the active feedback mode, the FPGA converts the estimated ΔB_z into a 9-bit digital signal and sends it to the digital input/output port of the arbitrary waveform generator (Zurich Instruments, HDAWG). The HDAWG applies the square-wave enveloped sinusoidal waveform with the frequency corresponding to the digital value to V_M using the multifrequency modulation function. For both probe and operation steps, an adaptive state initialization is performed by acquiring a 200 ns long sample and thresholding repeatedly until the lastest value falls below the threshold. For the entire data processing, about 60% of LUT and 38% of Flip Flop resources were used.

S4.2. Charge stability diagram and electron temperature

Fig. S4.2(a) shows the charge stability diagram as a function of gate voltages V_1 and V_2 showing the relevant region for the EST-Bayesian of our ST_0 qubit, where initialization/read-out points in (2,0) and the operation point in (1,1) are depicted as black circles. Fig. S4.2(b) shows the normalized charge transition signal of the last electron in the left quantum dot as a function of V_1 at the mixing chamber temperature T_{mixing} = 7 mK. This data is fitted to the Fermi-Dirac distribution curve given by $P_e(V_1) = \frac{1}{e^{a(V_1-\text{b})}+1}$, $a = \frac{\alpha}{k_B T_e}$, where a and b are fitting parameters, α is the lever-arm for V_1, k_B is the Boltzmann constant, and T_e is the electron temperature. The $1/a$ extracted at several different T_{mixing} is converted to T_e using α = 0.0497 meV/mV obtain from the linear relationship for T_{mixing} > 100 mK as shown in Fig. S4.2(c) [1]. From a power law $T_e(T_{\text{mixing}}) = (T_S^k + T_{\text{mixing}}^k)^{\frac{1}{k}}$ where T_S is a saturation limit of T_e at T_{mixing} = 0 mK and k is an exponent that depends on the thermalization mechanisms, we estimate T_S = 72 mK and k = 3.35, indicating that Wiedemann-Franz cooling is a dominant cooling mechanism rather than electron-phonon cooling [2].

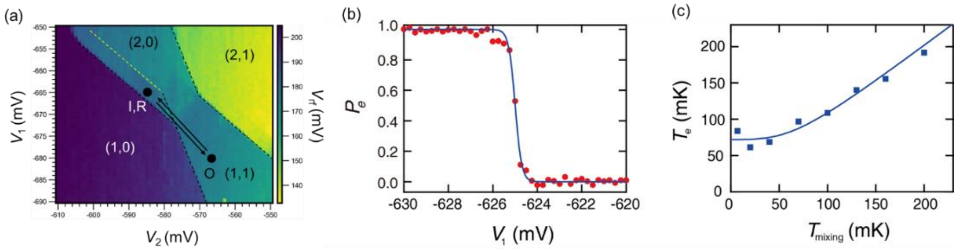

Supplementary Figure S4.2 (a) Charge stability diagram measured at the mixing chamber temperature T_{mixing} = 7 mK. The Yellow dashed line indicates the boundary of the EST-readout window. **(b)** Normalized charge transition signal from (1,0) to (0,0) as a function of V_1 at T_{mixing} = 7 mK. **(c)** Electron temperature T_e extracted from broadening of the Fermi-Dirac distribution as a function of T_{mixing} showing estimated T_e of 72 mK at T_{mixing} = 7 mK.

S4.3. Charge sensitivity

We evaluate the sensitivity of the charge sensor by observing the integration time t_{int} dependence of the signal-to-noise ratio (SNR). We define the SNR by $\Delta V/\sigma$, where ΔV is the sensor signal contrast for a single electron charge transition and σ is the rms noise amplitude at a given t_{int}. The sampling rate of the oscilloscope is set above 200 MHz. As shown in Fig. S4.3, the SNR is proportional to $\sqrt{t_{\text{int}}}$ and we linearly fit the SNR^2 to extract the minimum integration time for achieving SNR = 1, $\tau_{\min}$ of 2.45 ns [3].

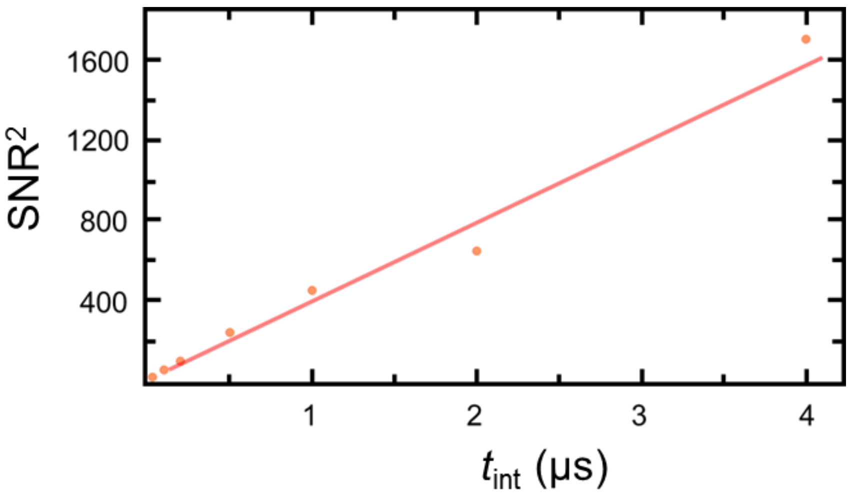

Supplementary Figure S4.3 Signal to noise ratio (SNR) of the RF-single-electron transistor charge sensor as a function of integration time t_{int}. The minimum integration time τ_{min} ~ 2.45 ns corresponding to the integration time for achieving the unit SNR is obtained from extrapolating a linear fit to the data.

Using τ_{min} as a suitable metric for binary charge detection sensitivity $e\sqrt{\tau_{\mathrm{min}}}$ [4,5], we compare performances of the recently published works as shown in Supplementary Table 4.1. [3,4,6-8] showing that the charge sensitivity achieved in this work is one of the best values available. By comparison, the charge sensor used in this work is more sensitive than a dispersive sensor with a cavity-coupled Josephson parametric amplifier [3] but less sensitive than a similarly prepared RF-SET in a strong quantum dot – sensor capacitive coupling regime [4].

Literature	τ_{min} (ns)	Charge Sensitivity ($e\sqrt{\mathrm{Hz}}$)
C. Barthel *et al*. (2009)[Ref. 5]	400	6.32×10^{-4}
C. Barthel *et al*. (2010)[Ref. 6]	23	1.52×10^{-4}
J. Stehlik *et al*. (2015)[Ref. 2]	7	8.37×10^{-5}
D. Keith *et al*. (2019)[Ref. 3]	1.25	3.54×10^{-5}
A. Noiri *et al*. (2020)[Ref. 7]	38	1.95×10^{-4}
Our work (2022)	2.45	4.95×10^{-5}

Supplementary Table 4.1. Comparison of minimum integration time τ_{min} and corresponding charge sensitivity.

S4.4. Visibility analysis

We analyze the visibility of the quantum oscillation shown in Fig. 4.3 in the main text with a numerical model which includes the thermal tunneling, and the false initialization errors. The analysis essentially amounts to combining the visibility with the computed readout infidelities to extract the relevance of other effects. We first evaluate the tunneling detection infidelity of our readout circuit by numerically simulating the histogram of the RF single-shot traces [9,10]. Following the Ref. 10, we fit the numerical histogram obtained from the simulated traces to the experimental histogram which yields the tunneling detection error (Fig. S4.4(a)) of E_T (E_N) ~ 1.4 % (0.7 %) where the E_T (E_N) corresponds to the infidelity for detecting the tunneling (no-tunneling) events.

Based on the tunneling detection infidelities, we extract the state measurement fidelities by fitting the Larmor oscillation curve to the numerical model which comprises the state relaxation, false initialization, and the thermal tunneling errors, where the following parameters describe the error rates respectively.

α_S : Thermal tunneling probability of the singlet (S) state

$\beta_{T(S)}$: Probability for the qubit state to be initialized to the triplet (singlet) state

: Relaxation probability ~ τ_{out}/T_1 ~ 0.3% where we use T_1 ~ 337 μs previously measured in Ref. 10 as a rough estimate. While T_1 time can be different depending on tuning conditions, we obtain measurement fidelity consistent with that of gate set tomography (see section S4.5 below).

With $P_{flip}(\tau)$ ~ $\sin^2(\pi\ \Delta B_Z\ \tau)$ corresponding to the ideal diabatic Larmor oscillation under the magnetic field gradient ΔB_Z, we estimate the probability $P_i(\tau)$ (i = S, T_0, T_+, T_-), which is the realistic probability for the qubit state to be at one of the two-spin states after the manipulation. We assume the polarized triplet states T_+, and T_-

states are not involved in the coherent dynamics at the manipulation stage, and all three triplet states have the same relaxation rates to the ground (singlet) state. We also suppose that false initialization probability to each of three triplet states is all equal to $\beta_T/3$. The estimation procedure is as follows.

i) $P_S(\tau)$: Probability for the final qubit state to be S after the manipulation.

- Initializes to S (β_S), does not flip under the manipulation pulse ($1- P_{flip}(\tau)$)

- Initializes to S (β_S), flip under the manipulation pulse ($P_{flip}(\tau)$), relax to the ground state (γ)

- Initializes to T_0 ($\beta_T/3$), flip under the manipulation pulse ($P_{flip}(\tau)$)

- Initializes to T+ or T- ($2\beta_T/3$), relax to the ground state (γ)

$$\Rightarrow P_S(\tau) = \beta_S[1-P_{flip}(\tau)+P_{flip}(\tau)\gamma]+{\beta_T}/{3}\,[P_{flip}(\tau)+(1-P_{flip}(\tau)\gamma)]+{2\beta_T}/{3}\,\gamma$$

ii) $P_{T0}(\tau)$: Probability for the final qubit state to be the T_0 after the manipulation.

- Initialize to S (β_S), flip under the manipulation pulse ($P_{flip}(\tau)$), does not relax to the ground state ($1-\gamma$)

- Initialize to T_0 ($\beta_T/3$), does not flip under the manipulation pulse ($1- P_{flip}(\tau)$), does not relax to the ground state ($1-\gamma$)

$$\Rightarrow P_{T0}(\tau) = \beta_S P_{flip}(\tau)(1-\gamma)+{\beta_T}/{3}\,(1-P_{flip})(1-\gamma)$$

iii) $P_{T+}(\tau)$ ($P_{T-}(\tau)$) : Probability for the final qubit state to be the T+ (T-) after the manipulation.

- Initialize to T+ (T-) ($\beta_T/3$), does not relax to the ground state ($1-\gamma$)

$$\Rightarrow P_{T+}(\tau) = P_{T-}(\tau) = {\beta_T}/{3}\,(1-\gamma)$$

Combined with the tunneling detection infidelities, the probability for the tunneling event to be detected $P_D(\tau)$ can be calculated as, $P_D(\tau)$ = ($P_{T0}(\tau)$ + $P_{T+}(\tau)$ +

$P_{T\text{-}}(\tau)$)(1-E_T) + $P_S(\tau)E_N$ + $\alpha_S P_S(\tau)$(1-E_T). We neglect the terms proportional to $E_T \cdot E_N$. By fitting the $P_D(\tau)$ to the measured Larmor oscillation (Fig. S4.4(b)), we extract the thermal tunneling error α_S ~ 0.6 %, and β_T < 0.1 %. Note that the adaptive initialization scheme described above facilitates very low false initialization error β_T and we expect the accurate measure of the β_T should be possible with the self-consistent tomography schemes [11]. Also, large $E_{ST}/k_B T_e$ at the EST readout position provided by singlet-triplet splitting E_{ST} on the order of 30 GHz [9] enables α_S < 1 %. Based on the error rates, we evaluate the singlet (triplet) measurement fidelity F_S (F_{T0}) ~ 99.28 % (~ 98.53 %) yielding the total measurement fidelity about 99 %. This corresponds to the quantum oscillation visibility of ~ 98 % consistent with the observation.

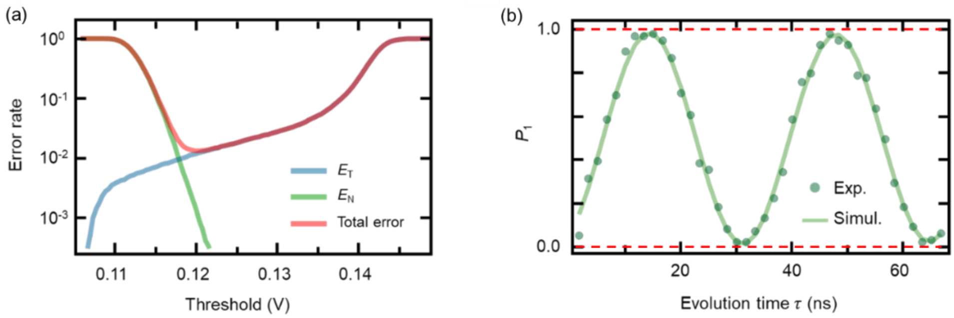

Supplementary Figure S4.4 Quantum oscillation visibility analysis (a) Tunneling (no-tunneling) detection infidelity shown in blue (green) curves. At the optimum threshold voltage, the error rate for the tunneling (no-tunneling) detection E_T (E_N) ~ 1.4 % (0.7 %) is obtained. The red curve corresponds to the total error (E_T + E_N) as a function of the threshold voltage. (**b)** Experimental Larmor oscillation curve (green dot) and the numerical model (green curve) comprising the thermal tunneling, false initialization, and the relaxation errors. Fit to the model yield thermal tunneling error (α_S) ~ 0.6 % with the false initialization error (β_T) < 0.1 %.

S4.5. Randomized Benchmarking and Gate Set Tomography

Randomized benchmarking (RB and IRB): A single-qubit Clifford gate set is constructed using primitive gates I, X, Y, ±X/2, and ±Y/2, which are implemented by calibrated RF bursts. For concatenating RF bursts, we use an idle time of 16 ns. The elements of the Clifford gate set are randomly selected during the benchmarking. Each point in Fig. 4.4(c) is obtained by averaging 1000 single-shot measurements per sequence. The measurement data obtained from the standard randomized benchmarking (RB) is fitted to the exponentially decaying curve $P_1(m) = Ap_{\mathrm{avg}}^m + B$ where m denotes the number of Clifford gates. The average gate fidelity F_{avg} is then determined by the depolarizing parameter p_{avg} as $(1+p_{\mathrm{avg}}) / 2$ [12].

The gate fidelity of each primitive gate, on the other hand, is obtained with respect to the reference random Clifford gate sets using interleaved randomized benchmarking (IRB) protocol [12]. The measurement data from the interleaved randomized benchmarking is fitted to the same exponentially decaying curve $P_1(m) = Ap_{\mathrm{gate}}^m + B$ to obtain the depolarizing parameter p_{gate}. The gate fidelity is then obtained as $(1+p_{\mathrm{gate}}/p_{\mathrm{avg}}) / 2$, where the effect of the reference RB is reflected as $1/p_{\mathrm{avg}}$ [12].

Gate set tomography (GST): We use a single qubit gate set of {I, X/2, Y/2}, where the notation for each element is the same as those in the RB. Specifically, the length of all gates is fixed to a specific length, including the idle gate I. Compositing the elements in the gate set, we conducted the GST experiment with germs {I, X/2, Y/2, X/2∘Y/2, X/2∘X/2∘Y/2} and fiducials {null, X/2, Y/2, X/2∘X/2, X/2∘X/2∘X/2, Y/2∘Y/2∘Y/2} and the results are analyzed using the open-source python package, pyGSTi [13].

Supplementary references

[1] I. Ahmed, A. Chatterjee, S. Barraud, J. J. L. Morton, J. A. Haigh, and M. F. Gonzalez-Zalba, Primary thermometry of a single reservoir using cyclic electron tunneling to a quantum dot, *Communications Physics* **1,** 66 (2018).

[2] C. P. Scheller, S. Heizmann, K. Bedner, D. Giss, M. Meschke, D. M. Zumbuhl, J. D. Zimmerman, and A. C. Gossard, Silver-epoxy microwave filters and thermalizers for millikelvin experiments, *Appl. Phys. Lett.* **104,** 5 (2014).

[3] J. Stehlik, Y. Y. Liu, C. M. Quintana, C. Eichler, T. R. Hartke, and J. R. Petta, Fast Charge Sensing of a Cavity-Coupled Double Quantum Dot Using a Josephson Parametric Amplifier, *Phys. Rev. Appl.* **4,** 014018 (2015).

[4] D. Keith, M. G. House, M. B. Donnelly, T. F. Watson, B. Weber, and M. Y. Simmons, Single-Shot Spin Readout in Semiconductors Near the Shot-Noise Sensitivity Limit, *Phys. Rev. X* **9,** 041003 (2019).

[5] Y. Makhlin, G. Schon, and A. Shnirman, Quantum-state engineering with Josephson-junction devices, *Rev. Mod. Phys.* **73,** 357 (2001).

[6] C. Barthel, D. J. Reilly, C. M. Marcus, M. P. Hanson, and A. C. Gossard, Rapid Single-Shot Measurement of a Singlet-Triplet Qubit, *Phys. Rev. Lett.* **103,** 160503 (2009).

[7] C. Barthel, M. Kjaergaard, J. Medford, M. Stopa, C. M. Marcus, M. P. Hanson, and A. C. Gossard, Fast sensing of double-dot charge arrangement and spin state with a radio-frequency sensor quantum dot, *Phys. Rev. B* **81,** 161308 (2010).

[8] A. Noiri, K. Takeda, J. Yoneda, T. Nakajima, T. Kodera, and S. Tarucha, Radio-Frequency-Detected Fast Charge Sensing in Undoped Silicon Quantum Dots, *Nano Lett.* **20,** 947 (2020).

[9] A. Morello *et al.*, Single-shot readout of an electron spin in silicon, *Nature* **467,** 687 (2010).

[10] W. Jang, J. Kim, M. K. Cho, H. Chung, S. Park, J. Eom, V. Umansky, Y. C. Chung, and D. Kim, Robust energy-selective tunneling readout of singlet-triplet qubits under large magnetic field gradient, *npj Quant. Inf.* **6,** 7 (2020).

[11] R. Blume-Kohout, J. K. Gamble, E. Nielsen, K. Rudinger, J. Mizrahi, K. Fortier,

and P. Maunz, Demonstration of qubit operations below a rigorous fault tolerance threshold with gate set tomography, *Nat. Commun.* **8,** 14485 (2017).
[12] E. Magesan *et al.*, Efficient Measurement of Quantum Gate Error by Interleaved Randomized Benchmarking, *Phys. Rev. Lett.* **109,** 080505 (2012).
[13] E. Nielsen, K. Rudinger, T. Proctor, A. Russo, K. Young, and R. Blume-Kohout, Probing quantum processor performance with pyGSTi, *Quantum Science and Technology* **5,** 044002 (2020).

Chapter 5. Single-shot readout of a driven hybrid qubit in a GaAs double quantum dot

Abstract

We report a single-shot-based projective readout of a semiconductor hybrid qubit formed by three electrons in a GaAs double quantum dot. Voltage-controlled adiabatic transitions between the qubit operations and readout conditions allow high-fidelity mapping of quantum states. We show that a large ratio both in relaxation time vs. tunneling time (~ 50) and singlet-triplet splitting vs. thermal energy (~ 20) allow energy-selective tunneling-based spin-to-charge conversion with readout visibility ~ 92.6 %. Combined with ac driving, we demonstrate high visibility coherent Rabi and Ramsey oscillations of a hybrid qubit in GaAs. Further, we discuss the generality of the method for use in other materials, including silicon.

Performing high-fidelity projective readout of qubit states is an important requirement in many steps of quantum information processing protocols [1–8]. In the semiconductor quantum dot (QD) qubit platform, state detection mainly uses sensors proximal to qubits, where the sensor is either sensitive to the number [9–14] or the susceptibility of the charges inside a QD to external perturbation [15–19]. Along with the progress in developing wide-bandwidth charge sensors [10,20],

---

This chapter is adapted from *Nano Letters* **21**, 12 (2021).

single-shot state detection methods have been employed in various spin qubits in semiconductors, including single-spin [21,22], singlet-triplet [23–29], and exchange-only qubits [30]. The rapidly repeated single-shot readout performed in these systems is also used for nuclear feedback control [31,32] and quantum non-demolition measurement [33,34].

The QD hybrid qubit (HQ) [35–38] compromises the desirable features of charge (fast manipulation) and spin (long coherence time) qubits. Formed by a decoherence-free subspace of three-electron spin states in a double QD, recent experiments on both Si/SiGe [36–38] and GaAs [39] have demonstrated fast electrical control of HQ with a favorable ratio between the manipulation time and coherence time T_2^*. Moreover, the naturally formed extended charge noise-insensitive sweet spot is tunable, and T_2^* exceeding 100 ns has been demonstrated in Si/SiGe [38]. However, so far these experiments have been performed by time-averaged measurements, while more advanced protocols [1,2,4–8] using HQ require high-fidelity single-shot readout. Time-averaged measurements are also often susceptible to errors in relaxation time T_1 compensated probability normalization.

In this work, we demonstrate high-fidelity single-shot measurements of a three-electron HQ in GaAs. The logical states $|0\rangle$ and $|1\rangle$ are mapped to spin states that are energetically separated by more than 20 times the thermal energy, and the energy-selective tunneling (EST) events between one of the QDs and the reservoir is measured by a radio-frequency single-electron transistor (rf-set). Similar to Ref.[37], we use resonant driving to coherently control the HQ states and demonstrate high-visibility, normalization-free two-axis control on the HQ Bloch sphere. Achieving measurement fidelity ~ 96.4 %, readout visibility ~ 92.6 %, and quantum oscillation visibility ~ 75 %, the result facilitates efficient HQ state detection with fidelity in line with the state-of-the-art EST single-shot detections achieved in various semiconductor gate-defined QD qubits [22,25].

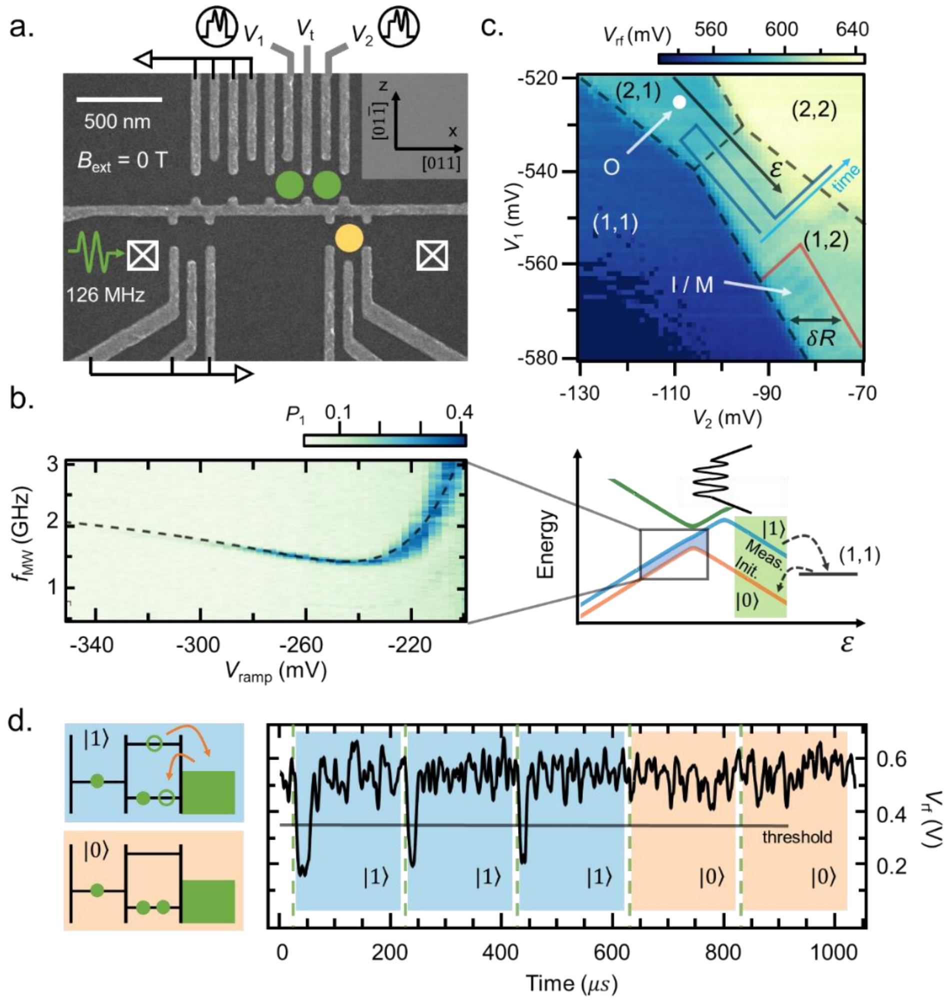

Figure 5.1 (a) Scanning electron microscope image of the hybrid qubit (HQ) device similar to the one used in the experiment. Green (Yellow) circles: Double (Single) quantum dot used to form an HQ (charge sensor). **(b)** Probability of the state $|1\rangle$, P_1, as a function of the ramp amplitude V_{ramp} and applied microwave frequency f_{MW}, illustrating the energy dispersion of the HQ. The black dashed line shows the calculated dispersion using the Hamiltonian described in supporting information.

Inset: Schematic energy levels of the HQ as a function of the energy detuning ε and pulse sequence used for the spectroscopy. (**c)** Double dot charge stability diagram near the (2,1) – (1,2) charge transition spanned by V_1 and V_2. The superimposed non-adiabatic step-pulse (blue pulse diagram) results in an oscillatory detector signal near the point I/M. (**d)** Single-shot traces of the HQ. The energy-selective tunneling (EST) readout of the HQ is enabled by putting the reservoir level between the qubit splitting. EST of $|1\rangle$ results in the step-pulse signal whereas no peak occurs for $|0\rangle$.

Fig. 5.1a shows a scanning electron microscope image of a QD device similar to the one we measured. The device is designed to form up to four QDs used for qubits, but we focus on the right double QD by grounding the irrelevant gate electrodes. Au/Ti gate electrodes are deposited on top of a GaAs/AlGaAs heterostructure, where a 2D electron gas (2DEG) is formed $70\ \mathrm{nm}$ below the surface. The device was operated in a dilution refrigerator with base temperature~ 20 mK and at zero external magnetic fields. The electron temperature is ~ 234 mK (see SI Section S5.3).

A previous study of HQ in GaAs double QD showed that operating the HQ near the (2,3)-(1,4) charge occupation provides energy tunability stemming from asymmetric and anharmonic potentials [39]. Instead, we operate our HQ with the same total number of electrons as proposed originally near the (2,1) – (1,2) charge transition. We define the qubit states at the readout window as $|0\rangle = |\downarrow\rangle|S\rangle$ and $|1\rangle = \sqrt{1/3}|\downarrow\rangle|T_0\rangle - \sqrt{2/3}|\uparrow\rangle|T_-\rangle$ where $|\downarrow\rangle$ and $|\uparrow\rangle$ represent the spin configuration of the single electron in the left QD and, $|S\rangle$, $|T_0\rangle$, and $|T_-\rangle$ represent the singlet (S) and triplet (T_0, T_-) spin configurations of the two electrons in the right QD as in the original HQ design [35,36]. Note that the spin states comprise $\left|S_{tot}=1/2,S_z=-1/2\right\rangle$ subspace. We describe the detailed energy levels and toy-model Hamiltonian in supporting information.

We perform ac-driven spectroscopy of the qubit frequency. As shown in the right panel of Fig. 5.1b, we start with an initial qubit state at the (1,2) ground level at the initialization and measurement point I/M. After adiabatically ramping the detuning ε to the operation point O, the resonant ac-modulation in the detuning induces the probability to be in the excited state, P_1, which is adiabatically mapped back to the point I/M. The point I/M is chosen so that the Fermi level of the right reservoir resides between the energies of $\left|0\right\rangle$ and $\left|1\right\rangle$ to enable EST. The same technique was used for HQ in Si/SiGe in time-averaged probability measurement [37]. Here, we monitor the charge difference using fast rf-reflectometry recording tunneling events at MHz bandwidth, which enables single-shot projective readout. As we show below in detail, the double QD used in this work exhibits a highly asymmetric singlet-triplet splitting between the dots, where the splitting in the left (right) dot, δL (δR) is ~ 3 (96) h·GHz. The exceptionally small δL may be a possible evidence for the non-negligible electron-electron interaction which is known to cause quenching of excited orbital energy spectrum [40,41] (see SI Section S5.2 for preliminary theoretical calculation). From the magnetic field susceptibility measurement (see SI section S5.2) we show that the (2,1) qubit states split by δL have the same S_{tot}, and S_z where the spin-conserving tunnel-coupling ensures the (2,1) ground states with $\left|S_{tot}=1/2,S_z=-1/2\right\rangle$ can be prepared via the adiabatic passage discussed above. Thus we interpret the (2,1) qubit states observed in this work as the

HQ states, and use the toy-model Hamiltonian identical to the original HQ proposal [35,42] to simulate the energy dispersion. The calculation agrees well with the measured energy dispersion (black dashed curve, Fig. 5.1b). While further studies including the exact diagonalization calculation [41,43] are required to reveal the actual origin of the asymmetry, we focus on the single-shot readout of the HQ in this work and leave the detailed investigation of the energy levels for the future works.

Fig. 5.1c shows a double-dot charge stability diagram where the scanning gate voltage is superimposed with a voltage pulse with a rise time of 100 ps and width of 10 ns (schematic in Fig. 5.1c, see SI for zoom-out version of the diagram, and the high-frequency setup), which induces a non-adiabatic coherent Landau-Zener tunneling. The range of the gate voltage V_2 where these oscillations appear can be used for estimating singlet-triplet splitting ~ 0.39 meV using the measured lever arm 0.028. This is ~ 20 times larger than the thermal energy ~ 20 μeV. As shown in Fig. 5.1d, the real-time traces of the rf-set signal at I/M show a clear distinction between $|0\rangle$ and $|1\rangle$. An electron occupying an excited orbital state of $|1\rangle$ tunnels to the reservoir to form the (1,1) charge state, leading to an abrupt change in the sensor signal, and initializes back to the energetically favorable $|0\rangle$. In contrast, no tunneling occurs for the state $|0\rangle$.

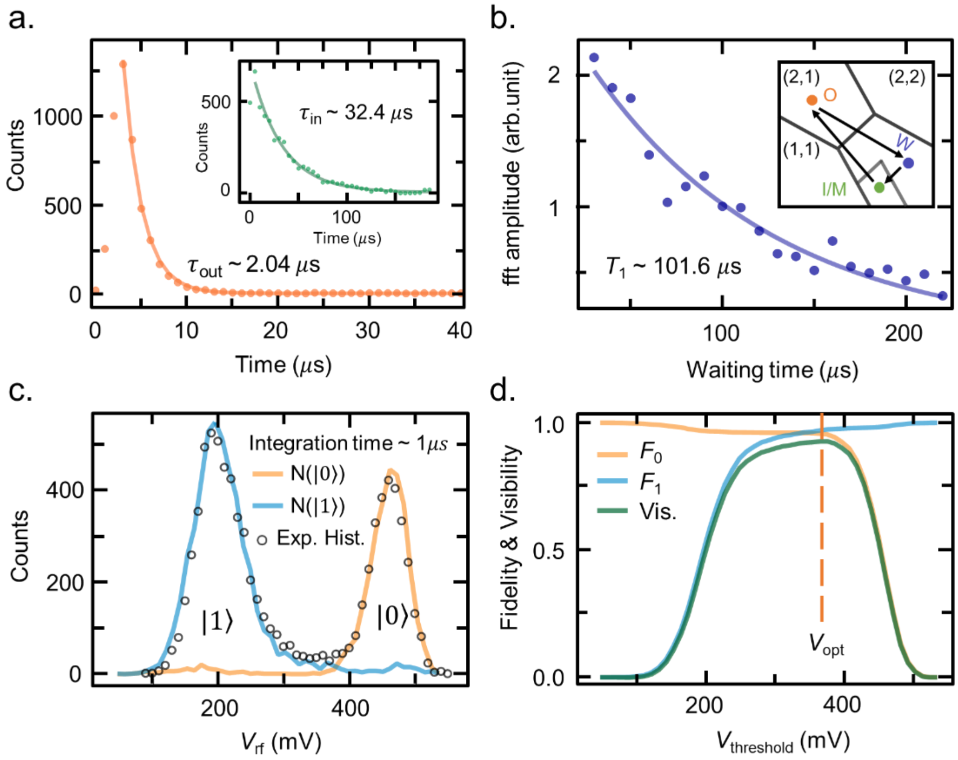

Figure 5.2 (a) Histogram of the tunnel-out time τ_{out}. Inset: Histogram of the tunnel-in time τ_{in}. Exponential fits yield, τ_{out} = 2.04 ±0.03 μs, and τ_{in} = 32 ± 3 μs. **(b)** Relaxation time T_1 measurement at ε identical to point I/M. By observing the amplitude decay of the Larmor oscillation as a function of the waiting time at the point W indicated in the inset, T_1 = 102 ± 6 μs is obtained. (**c**) Histogram of the detector signal with an integration time of 1 μs. The solid curves are the histograms for the states $|0\rangle$ and $|1\rangle$ simulated using the experimentally obtained τ_{out} , τ_{in} , T_1, and the thermal tunneling probability. **(d)** Calculated fidelity and visibility as a function of the threshold level $V_{threshold}$ showing the readout fidelity for the state $|0\rangle$ ($|1\rangle$) of 95.4 % (97.3 %). The readout visibility is 92.6 % at the optimal threshold V_{opt}.

We analyze the performance of the single-shot readout by optimizing various tunneling rates and signal integration times. Fig. 5.2a depicts the time-resolved tunnel-out events, which predominantly involve triplet states, triggered at the end of the pulse sequence. We measure the tunneling-out time $\tau_{out} \sim 2$ μs extracted from the exponential fitting. Similar measurements for tunneling in events, which occurs mostly by singlet states, result in a tunneling-in time of $\tau_{in} \sim 32$ μs (Fig. 5.2a, inset). Highly asymmetric tunneling times stem from different spatial distributions of the orbital wave functions of the singlet and triplet states that lead to different dot-to-reservoir coupling [23,25]. We note that this large difference in state-dependent tunneling rates can, in principle, be used for tunneling rate-based single-shot measurement, which can be useful for reducing measurement times [23], but here we focus on the Elzerman-type readout [21] and set the measurement window to 140 μs longer than τ_{in}. Compared with these time scales, T_1 at the point I/M shown in Fig. 5.2b, which is obtained by measuring the decay of the oscillation visibility as a function of the waiting time at point W (see inset to Fig. 5.2b), is longer than 100 μs leading to T_1/τ_{in} about 50. Fig. 5.2c, which depicts the signal histogram with 1 μs integration time, shows a separation of the mean value of the $|0\rangle$ and $|1\rangle$ signal levels by more than 5 times the standard deviation. Using these parameters, we estimate the measurement fidelities for $|0\rangle$, $|1\rangle$, and readout visibility that accounts for measurement errors owing to relaxation and thermal tunneling events [22,25] (see SI section S5.4). As shown in Fig. 5.2d, the measurement fidelity (visibility) reaches 96.4% (92.6%) at the optimum threshold, confirming high-fidelity single-shot readout of the HQ states (see SI section S5.5). Moreover, using master equation simulations and additional T_1 measurements, we estimate that the readout error due to leakage and state relaxation during the adiabatic ramp pulse is less than 2 % (see SI section S5.4).

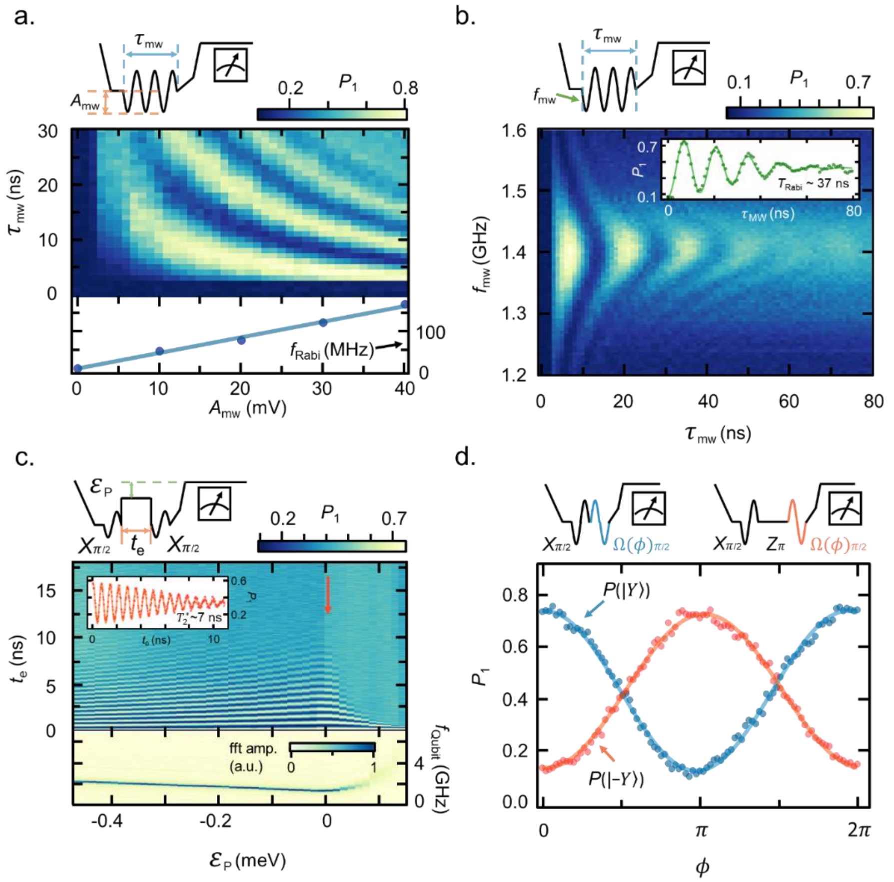

Figure 5.3 (a) P_1 as a function of the microwave burst time τ_{mw} and amplitude A_{mw} at instrument output when the resonant driving frequency f_{mw} ~ 1.4 GHz. The bottom panel shows that the Rabi frequency f_{Rabi} increases linearly with A_{mw}. **(b)** Rabi oscillation of P_1 as a function of f_{mw} and τ_{mw}. Inset: Line-cut at f_{mw} ~ 1.4 GHz. (**c**) ac-Ramsey oscillation as a function of the detuning amplitude ε_P and free evolution time t_e. Inset: Line-cut showing T_2^* ~ 7 ns at the ε_P indicated by an arrow. The bottom panel shows the fast Fourier transform of the time-domain signal indicating that the spectrum is consistent with Fig. 5.1(b). (**d**) Projection of the initial state along (opposite to) the y-axis of the Bloch sphere ($P(|Y\rangle)$ blue and $P(|-Y\rangle)$ orange) to the measurement axis controlled by the phase ϕ of the second rotation pulse demonstrating two-axis control of the HQ qubit on the x-y plane of the Bloch sphere. The solid lines are fittings to the sinusoidal function. The upper insets in **(a)**- **(d)** show the schematic pulse sequences used for the corresponding measurements, and the microwave bursts with the Gaussian rising / falling edge with ~ 1 ns rise/fall time are utilized. The inclusion of the Gaussian envelop leads to negligible P_1 for τ_{mw} < 2 ns.

We now discuss the application of the single-shot readout method to ac-driven coherent operations of the HQ. Applying bursts of ac detuning modulation at the point O yields Rabi oscillations corresponding to *x*-axis rotations on the Bloch sphere, as shown in Figs. 5.3a-b. The typical Rabi frequency, which is of the order of 100 MHz, increases linearly as a function of the microwave amplitude A_{mw} at the output port of the waveform generator. Although the readout visibility with perfect gate control can be as high as 92.6 %, the limited Rabi decay time due to decoherence and finite pulse length (see SI Section S5.4) leads to maximum oscillation visibility of approximately 75 % in this experiment.

Moreover, T_2^* is characterized by performing a Ramsey experiment (Fig. 5.3c), which demonstrates *z*-axis rotations on the qubit Bloch sphere. Between the first and second rotation pulses $X_{\pi/2}$, which initialize the superposition state and set the measurement axis, respectively, we apply a ramp-evolution pulse with detuning amplitude ε_{P}. Z-axis rotation during the evolution time t_{e} results from the development of a relative phase between $|0\rangle$ and $|1\rangle$, given by, $\varphi = -t_{\mathrm{e}}\cdot(2\pi f_{\mathrm{Qubit}})$ where f_{Qubit} is the qubit frequency. Typically, T_2^* is of the order of 7 ns, which is similar to earlier results (Fig. 5.3c, inset) [39]. While a recent theory provides coherence analysis of HQs in both GaAs and Si [44], more work is necessary for systematically identifying the dominant sources of noise in this system.

Furthermore, Fig. 5.3d demonstrates two-axis controllability on the *x*-*y* plane of the Bloch sphere. The P_1 oscillations of the states initially prepared along and opposite to the *y*-axis ($\mathrm{P}(|Y\rangle)$ and $\mathrm{P}(|\text{-}Y\rangle)$) are out-of-phase as a function of the phase ϕ of the measurement pulse $\Omega(\phi)_{\pi/2}$ that determines the angle between the x-axis and the measurement axis. Together with the Rabi (x-axis control) and Ramsey (z-axis control) oscillations, the result demonstrates the full control of the GaAs HQ with single-shot readout capability.

In this experiment, the highly asymmetric singlet–triplet energy splitting, possibly originating from the electron-electron interaction [40,41], was exploited, which provided the f_{Qubit} ~ 1.4 GHz regime during operation in the (2,1) configuration that facilitates electronic ac-control. It also provided the f_{Qubit} ~ 95.8 GHz regime in the measurement configuration (1,2), which is useful for high-fidelity EST. While the technique is general and can be used for GaAs HQ in other electron occupancies as well as silicon-based HQ [37,45], further investigations are required for determining a convenient regime for both ac-control and high-fidelity measurement. In Si/SiGe, T_1 at the I/M point is shown to exceed 100 ms [35] which facilitates high-fidelity single-shot readout even with a room-temperature trans-impedance amplifier. Moreover, the current quantum oscillation visibility is limited by T_2^* for the given tuning. While the splitting in the energy level in the operation configuration is expected to be tunable, one cannot rule out that T_2^* of the HQ in GaAs in this tuning is limited by nuclear fluctuations that mix different logical states. In such a situation, reducing $\mathrm{d}f_{\text{Qubit}} / \mathrm{d}\varepsilon$ and hence, reducing the susceptibility to charge noise by further tuning may not necessarily increase T_2^*. We plan to investigate the dominant source of noise by systematic tuning as well as the HQ regime for the left double QD (Fig. 5.1a) in the same device.

In conclusion, we have demonstrated the high-fidelity EST-single-shot readout of a driven HQ in GaAs. Achieving a measurement fidelity ~ 96.4 % and readout visibility ~ 92.6 %, which are comparable with state-of-the-art EST single-shot detections for other types of QD qubits [22,25,46], the results set the benchmark for HQ readout performance and provide a useful demonstration that can be adopted for HQ in a more general setting. With single-shot readout on a μs time scale, experiments involving fast Hamiltonian learning [32,47] or detecting wide-band noise spectra [47–50] using HQ, whose demonstration has so far been limited only to single-spin and singlet-triplet qubits, are also conceivable.

References

[1] A. R.Calderbank, and P. W. Shor, Good Quantum Error-Correcting Codes Exist. *Phys. Rev. A* **54**, 1098–1105, (1996).

[2] M. D. Reed *et al.*, Realization of Three-Qubit Quantum Error Correction with Superconducting Circuits. *Nature* **482**, 382–385, (2012).

[3] M. A. Nielsen, and I. L. Chuang, *Quantum Computation and Quantum Information*, 10th anniversary ed.; Cambridge University Press: Cambridge ; New York, (2010).

[4] P. Aliferis, and A. W. Cross, Subsystem Fault Tolerance with the Bacon-Shor Code. *Phys. Rev. Lett.* **98**, 220502, (2007).

[5] L. K. Grover, Quantum Mechanics Helps in Searching for a Needle in a Haystack. *Phys. Rev. Lett.* **79**, 325–328, (1997).

[6] P. Shor, Polynomial-Time Algorithms for Prime Factorization and Discrete Logarithms on a Quantum Computer. *SIAM Rev.* **41**, 303–332, (1999).

[7] P. Schindler *et al.*, Experimental Repetitive Quantum Error Correction. *Science* **332**, 1059–1061, (2011).

[8] E. Knill, Quantum Computing with Realistically Noisy Devices. *Nature* **434**, 39–44, (2005).

[9] M. Field *et al.*, Measurements of Coulomb Blockade with a Noninvasive Voltage Probe. *Phys. Rev. Lett.* **70**, 1311–1314, (1993).

[10] D. J. Reilly, C. M. Marcus, M. P. Hanson, and A. C. Gossard, Fast Single-Charge Sensing with a Rf Quantum Point Contact. *Appl. Phys. Lett.* **91**, 162101, (2007).

[11] R. Hanson, *et al.*, Spins in Few-Electron Quantum Dots. *Rev. Mod. Phys.* **79**, 1217–1265, (2007).

[12] F. A. Zwanenburg, *et al.*, Silicon Quantum Electronics. *Rev. Mod. Phys.* **85**, 961–1019, (2013).

[13] W. Lu *et al.*, Real-Time Detection of Electron Tunnelling in a Quantum Dot. *Nature* **423**, 422–425, (2003).

[14] M. Yuan *et al.*, Si/SiGe Quantum Dot with Superconducting Single-Electron Transistor Charge Sensor. *Appl. Phys. Lett.* **98**, 142104, (2011).

[15] J. I. Colless *et al.*, Dispersive Readout of a Few-Electron Double Quantum Dot with Fast Rf Gate Sensors. *Phys. Rev. Lett.* **110**, 046805, (2013).

[16] A. Rossi, R. Zhao, A. S. Dzurak, and M. F. Gonzalez-Zalba, Dispersive Readout of a Silicon Quantum Dot with an Accumulation-Mode Gate Sensor. *Appl. Phys. Lett.* **110**, 212101, (2017).

[17] M. F. Gonzalez-Zalba, S. Barraud, A. J. Ferguson, and A. C. Betz, Probing the Limits of Gate-Based Charge Sensing. *Nat. Commun.* **6**, 6084, (2015).

[18] M. F. Gonzalez-Zalba *et al.*, Gate-Sensing Coherent Charge Oscillations in a Silicon Field-Effect Transistor. *Nano Lett.* **16**, 1614–1619, (2016).

[19] J. Verduijn, M. Vinet, and S. Rogge, Radio-Frequency Dispersive Detection of Donor Atoms in a Field-Effect Transistor. *Appl. Phys. Lett.*, **104**, 102107, (2014).

[20] C. Barthel *et al.*, Fast Sensing of Double-Dot Charge Arrangement and Spin State with a Radio-Frequency Sensor Quantum Dot. *Phys. Rev. B* **81**, 161308, (2010).

[21] J. M. Elzerman *et al.*, Single-Shot Read-out of an Individual Electron Spin in a Quantum Dot. *Nature* **430**, 431–435, (2004).

[22] A. Morello *et al.*, Single-Shot Readout of an Electron Spin in Silicon. *Nature* **467**, 687–691, (2010).

[23] R. Hanson *et al.*, L. M. K. Vandersypen, Single-Shot Readout of Electron Spin

States in a Quantum Dot Using Spin-Dependent Tunnel Rates. *Phys. Rev. Lett.* **94**, 196802, (2005).

[24] C. Barthel *et al.*, Rapid Single-Shot Measurement of a Singlet-Triplet Qubit. *Phys. Rev. Lett.* **103**, 160503, (2009).

[25] W. Jang *et al.*, Robust Energy-Selective Tunneling Readout of Singlet-Triplet Qubits under Large Magnetic Field Gradient. *npj Quantum Inf.* **6**, 64, (2020).

[26] T. Nakajima *et al.*, Robust Single-Shot Spin Measurement with 99.5% Fidelity in a Quantum Dot Array. *Phys. Rev. Lett.* **119**, 017701, (2017).

[27] P. Harvey-Collard *et al.*, High-Fidelity Single-Shot Readout for a Spin Qubit via an Enhanced Latching Mechanism. *Phys. Rev. X* **8**, 021046, (2018).

[28] L. A. Orona *et al.*, Readout of Singlet-Triplet Qubits at Large Magnetic Field Gradients. *Phys. Rev. B* **98**, 125404, (2018).

[29] M. A. Broome *et al.*, High-Fidelity Single-Shot Singlet-Triplet Readout of Precision-Placed Donors in Silicon. *Phys. Rev. Lett.* **119**, 046802, (2017).

[30] J. Medford *et al.*, Self-Consistent Measurement and State Tomography of an Exchange-Only Spin Qubit. *Nat. Nanotechnol.* **8**, 654–659, (2013).

[31] H. Bluhm *et al.*, Enhancing the Coherence of a Spin Qubit by Operating It as a Feedback Loop That Controls Its Nuclear Spin Bath. *Phys. Rev. Lett.* **105**, 216803, (2010).

[32] M. D. Shulman *et al.*, Suppressing Qubit Dephasing Using Real-Time Hamiltonian Estimation. *Nat. Commun.* **5**, 5156, (2014).

[33] T. Nakajima *et al.*, Quantum Non-Demolition Measurement of an Electron Spin Qubit. *Nat. Nanotechnol.* **14**, 555–560, (2019).

[34] X. Xue *et al.*, Repetitive Quantum Nondemolition Measurement and Soft

Decoding of a Silicon Spin Qubit. *Phys. Rev. X* **10**, 021006, (2020).

[35] Z. Shi *et al.*, Fast Hybrid Silicon Double-Quantum-Dot Qubit. *Phys. Rev. Lett.* **108**, 140503, (2012).

[36] D. Kim *et al.*, Quantum Control and Process Tomography of a Semiconductor Quantum Dot Hybrid Qubit. *Nature* **511**, 70–74, (2014).

[37] D. Kim *et al.*, High-Fidelity Resonant Gating of a Silicon-Based Quantum Dot Hybrid Qubit. *npj Quantum Inf.* **1**, 15004, (2015).

[38] B. Thorgrimsson *et al.*, Extending the Coherence of a Quantum Dot Hybrid Qubit. *npj Quantum Inf.* **3**, 1–4, (2017).

[39] G. Cao *et al.*, Tunable Hybrid Qubit in a GaAs Double Quantum Dot. *Phys. Rev. Lett.* **116**, 086801, (2016).

[40] S. Pecker *et al.*, Observation and Spectroscopy of a Two-Electron Wigner Molecule in an Ultraclean Carbon Nanotube. *Nat. Phys.* **9**, 576–581, (2013).

[41] J. Corrigan *et al.*, Coherent Control and Spectroscopy of a Semiconductor Quantum Dot Wigner Molecule. *arXiv:2009.13572*, (2020).

[42] Z. Shi *et al.*, Fast Coherent Manipulation of Three-Electron States in a Double Quantum Dot. *Nat. Commun.* **5**, 3020, (2014).

[43] M. Rontani, C. Cavazzoni, D. Bellucci, and G. Goldoni, Full Configuration Interaction Approach to the Few-Electron Problem in Artificial Atoms. *The Journal of Chemical Physics* **124** (12), 124102, (2006).

[44] E. Ferraro, M. Fanciulli, and M. D. Michielis, Coherence Time Analysis in Semiconducting Hybrid Qubit under Realistic Experimental Conditions. *Adv. Quantum Technol.* **1**, 1800040, (2018).

[45] M. Friesen, M. A. Eriksson, and S. N. Coppersmith, Magnetic Field

Dependence of Valley Splitting in Realistic Si/SiGe Quantum Wells. *Appl. Phys. Lett.* **89**, 202106, (2006).

[46] C. B. Simmons *et al.*, Tunable Spin Loading and T 1 of a Silicon Spin Qubit Measured by Single-Shot Readout. *Phys. Rev. Lett.* **106**, 156804, (2011).

[47] T. Nakajima *et al.*, Coherence of a Driven Electron Spin Qubit Actively Decoupled from Quasistatic Noise. *Phys. Rev. X* **10**, 011060, (2020).

[48] O. E. Dial *et al.*, Charge Noise Spectroscopy Using Coherent Exchange Oscillations in a Singlet-Triplet Qubit. *Phys. Rev. Lett.* **110**, 146804, (2013).

[49] F. K. Malinowski *et al.*, Spectrum of the Nuclear Environment for GaAs Spin Qubits. *Phys. Rev. Lett.* **118**, 177702, (2017).

[50] J. Yoneda *et al.*, A Quantum-Dot Spin Qubit with Coherence Limited by Charge Noise and Fidelity Higher than 99.9%. *Nat. Nanotechnol.* **13** (2), (2018).

Supporting Information 5

S5.1. Stability diagram measurement down to zero-electron regime

Here we show the stability diagram in wider region to show the three-electron occupancy at the hybrid qubit operation / readout regime in this work (Fig. S5.1). Also, the Pauli spin-blockade (PSB) measurements at (2,0), and (0,2) charge configuration are demonstrated respectively to show the asymmetry in the singlet-triplet splitting of the left and the right dot (Fig. S5.2).

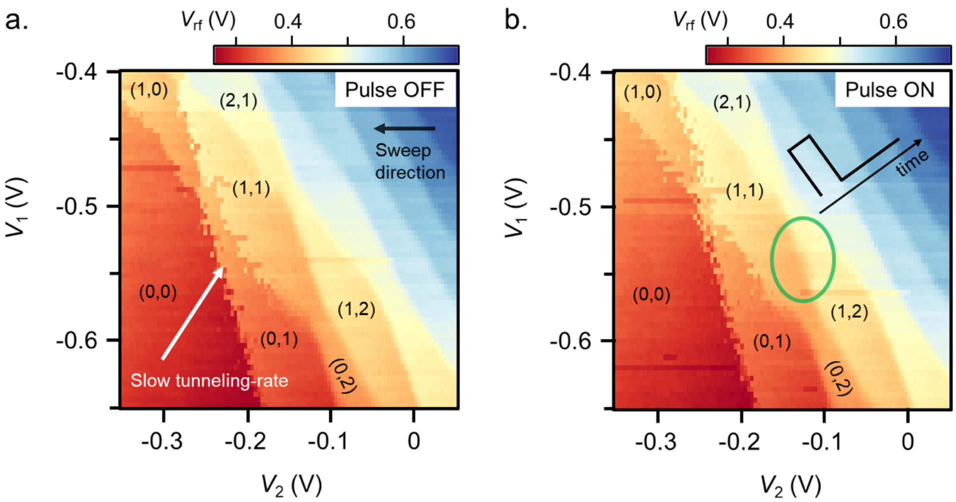

Fig. S5.1 Stability diagram measurement down to zero electron regime without (a.) and with (b.) the diabatic pulse superposed. a. Stability diagram measurement spanned by V_1 and V_2 gate voltages down to the zero electron regime confirms the three-electron occupation in the hybrid qubit readout and operation point within a double quantum dot. Due to the slow tunnel-rates in the single-electron regime charge latching behavior [1] is visible (white-arrow). **b**. Diabatic rectangular pulse of ~ 2 ns width with ~ 33 kHz repetition rate is superposed to the dc gate voltages when measuring the same stability diagram as in a. The diabatic excitation-induced readout window is visible in the (1,2) charge regime (green circle). The sensor gate bias is compensated depending on V_1, and V_2. The V_2 gate voltages are swept along the direction denoted in the black arrow in a.

Fig. S5.2 shows the stability diagrams spanned by V_1, and V_2 near the (2,0)-(1,1) (red box), and (1,1)-(0,2) (yellow box) charge configuration. Left inset to the red {yellow} box depicts the diagram recorded by the rf-charge sensor signal where the triangular pulses with the rise-in (-out) time of ~ 20 ns (~ 300ps) toward the (1,1) charge region are superposed to the dc-voltages at ~ 20 kHz repetition rate (yellow line schematic inside the left inset). The pulse adiabatically brings (2,0)S {(0,2)S} state across the S-T+ anticrossing to (1,1)T+ state, and non-adiabatically takes the (1,1)T+ back to the (2,0) {(0,2)} region which results significant triplet population hence the PSB. The right inset to the red {yellow} box is the pulse-synced boxcar integrated signal concurrently obtained with the left inset. The boxcar integrator effectively samples and averages ~ 1 μs signal window after the pulse non-adiabatically returns to the measurement point and reveals the PSB region as shown in the right inset to the yellow box. Note that the pulse also reveals the energy selective tunneling (EST) readout points of the ST_0 qubit and the hybrid qubit. In contrast, the boxcar integrated diagram near (2,0)-(1,1) charge transition does not exhibit the PSB which demonstrates the ST_0 splitting of the left dot is too small and PSB is lifted.

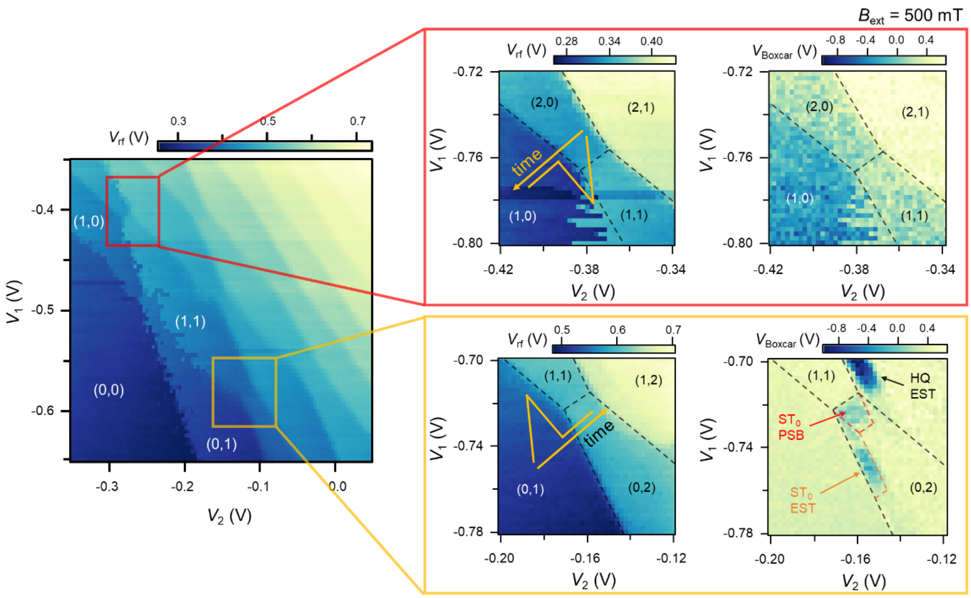

Fig. S5.2 Pauli spin-blockade (PSB) measurement of the singlet-triplet (ST_0) qubit at the (2,0), and (0,2) charge configuration. Red {yellow} box shows the stability diagrams near the (2,0)-(1,1) {(1,1)-(0,2)} charge configuration spanned by V_1, and V_2. Triangular pulse with the rise-in (-out) time of ~ 20 ns (~ 300 ps) is superposed to the dc-voltages at ~ 20 kHz repetition rate to yield the spin-blockaded (1,1) states within the (2,0) {(0,2)} charge region. Left (right) inset to both red and yellow boxes is the bare rf-charge sensor (boxcar integrated) signal. The boxcar integrator is synced to the pulse repetition rate and effectively samples ~ 1 μs window after the pulse returns to the measurement point to capture the short-lived excited state signal. The boxcar integrated signal reveals the typical PSB within the (0,2) region as well as the energy-selective tunneling readout points of the ST_0, and the hybrid qubits. In contrast, PSB is not visible in the (2,0) charge region. In-plane magnetic field, B_{ext} = 500 mT is applied.

S5.2. Exact-diagonalization, magneto spectroscopy, and the toy Hamiltonian

Exceptionally small singlet-triplet splitting in the left dot is unusual given that the typical size of the orbital splitting in the GaAs quantum dot (QD) is expected to be on the order of $10^1 \sim 10^2$ h·GHz [2–4]. The charge stability diagram shown in Fig. S5.1 confirms the double quantum dot structure, excluding the possibility of the energy modulation by the electrons from another QD. We conjecture that the electron-electron interaction which is usually not considered in the hybrid qubit (HQ) systems, is a possible reason for the extraordinary small splitting similar to recently reported works [5,6]. Likewise, here we show the preliminary calculation results derived by the full configuration interaction (FCI) method along with the electrostatic simulation and numerically demonstrate the energy splitting quenches from ~ 10^1 h·GHz to 10^0 h·GHz in the left dot.

The Hamiltonian of two electrons in a quantum dot can be written as,

$$H = -\frac{\hbar}{2m^*}(\nabla_1^2 + \nabla_2^2) - \mathrm{e}V(\mathbf{r_1}) - \mathrm{e}\,V(\mathbf{r_2}) + \frac{\mathrm{e}^2}{4\pi\varepsilon|\mathbf{r_1} - \mathbf{r_2}|} \tag{1}$$

where m^* is the effective mass of the electron in GaAs, $\mathbf{r_1}$ and $\mathbf{r_2}$ are position operators, ∇_1^2 and ∇_2^2 are the Laplacian operators, and the confinement potential V. The spatial potential distribution V near the double-QD site is obtained self-consistently (Fig. S5.3a-S5.3c), by iteratively solving the Poisson equation within the Thomas-Fermi approximation. The distribution is calculated with the finite element method using the COMSOL Multiphysics software using the real device geometry and parameters.

As the direct diagonalization of the given two-electron Hamiltonian calls for solving ~ 10^{10} x 10^{10} sized dense matrix, we here harness the FCI method to approximate the system [5,7]. In the FCI calculation, linear combinations of all possible Slater determinants, configuration state function (CSF), were used to estimate the energy eigenstates of the multi-electron system. The CSF derived from the combination of the single-electron eigenstates are classified by the number of excited electrons. The two-electron Hamiltonian is diagonalized in the basis constructed with the ground state CSF, singly-excited CSFs, and doubly-excited CSFs.

The single-electron Hamiltonian,

$$H_1 = -\frac{\hbar}{2m^*}\nabla^2 - \mathrm{eV}(\mathbf{r}) \tag{2}$$

can be discretized as a sparse matrix with five diagonals by adopting the five-point stencil method with the Dirichlet boundary condition. As in the harmonic potential case, we assume zero-valued wavefunctions at the boundary and calculate 100 eigenstates and eigenenergies from the discretized Hamiltonian with the Python package SciPy's '*eigsh*' method [8]. Because of the spin-degeneracy, 100 spatial eigenstates correspond to 200 spin eigenstates.

By combining the 200 spin eigenstates, one ground CSF, 396 singly excited CSFs, and 19503 doubly excited CSFs are derived. With these CSFs, the matrix elements of the Hamiltonian can be calculated with the Slater-Condon rule which connects FCI Hamiltonian matrix element with one-electron integrals and two-electron integrals for each CSF. The one-electron integral is N^2 sized matrix with the elements

$$\langle i|h|j\rangle = \delta_{s_i s_j} \int \psi_i^*(\mathbf{r}) H_1 \psi_j(\mathbf{r}) \mathrm{d}\mathbf{r} \tag{3}$$

where N is the number of spin basis, $\psi_i(\mathbf{r})$ and s_i are the spatial wavefunction of the i^{th} single electron eigenstate and spin quantum number respectively. Also, the two-electron integral, which represents the electron-electron interaction is an N^4 sized four-dimensional tensor whose elements are

$$\langle ij|V_{ee}|kl\rangle = \delta_{s_i s_k} \delta_{s_j s_l} \int \psi_i^*(\mathbf{r}_1) \psi_j^*(\mathbf{r}_2) \frac{e^2}{4\pi\varepsilon|\mathbf{r}_1 - \mathbf{r}_2|} \psi_k(\mathbf{r}_1) \psi_l(\mathbf{r}_2) \mathrm{d}\mathbf{r}_1 \mathrm{d}\mathbf{r}_2 \tag{4}$$

Computation of both one and two-electron integrals are accelerated with the graphics processing units (GPUs, NVIDIA RTX 3090) using the Python library CuPy [9].

Figure S5.3d shows the result of the numerical calculation. Energy levels without electron-electron interaction are obtained by assigning 0 to every two-electron integral term. Since calculated coefficients of the ground state and near-ground excited states are concentrated on CSF of small excited single wavefunctions, the calculation with the 100 spatial basis sets is reasonable. According to the calculation, when the electron-electron interaction is neglected the energy splitting between the ground and the first excited state is ~ 50 h·GHz (Fig. 5.2d, black lines) which well matches with the typical ST_0 splitting reported in the previous reports [2–4]. Also, ~ 50 h·GHz splitting is smaller than the ST_0 splitting of the right QD as can be expected from the physical size of the QD (Fig. S5.3b), also showing the validity of the calculation. When the electron-electron interaction is taken into account, the energy splitting quenches down to ~ 1.3 h·GHz (Fig. S5.3d, blue lines) which agrees with the experimental observation. Note that this calculation is rather preliminary as the current calculation considers only the single-dot energy levels (left dot) and does not yet consider the finite nuclear field effects nor the detuning dependence of the energy levels. We do not mean to precisely fit the exact value of experimentally observed singlet-triplet splitting in the left QD. Nevertheless, the initial numerical calculation shown here successfully explains the bulk part of the physics.

At this early stage, we believe significant ellipticity of the confinement potential found in the left dot (Fig. S5.3b) compared to the right dot as well as a rather shallow potential depth are critical to have the dominant effect of electron-electron interaction. Roughly the shallow potential leads to the Wigner parameter $R_W = (e^2/\kappa l_0)/\hbar\omega_0$ about 5 for the left dot showing that the left dot is in the strongly correlated regime, where κ is the dielectric constant of the GaAs, l_0 is the spatial extent of the 1s orbital, and ω_0 is the characteristic energy splitting when the confinement potential is approximated to be parabolic. In comparison, the more strongly confined right dot (see Fig. S5.3b) does not experimentally show significant excited-level quenching, and part of the reason is the sufficiently negative voltage applied to the rightmost gate to tune the right dot to reservoir tunnel rate slow enough to enable single-shot readout, which leads to a more circular and symmetric dot.

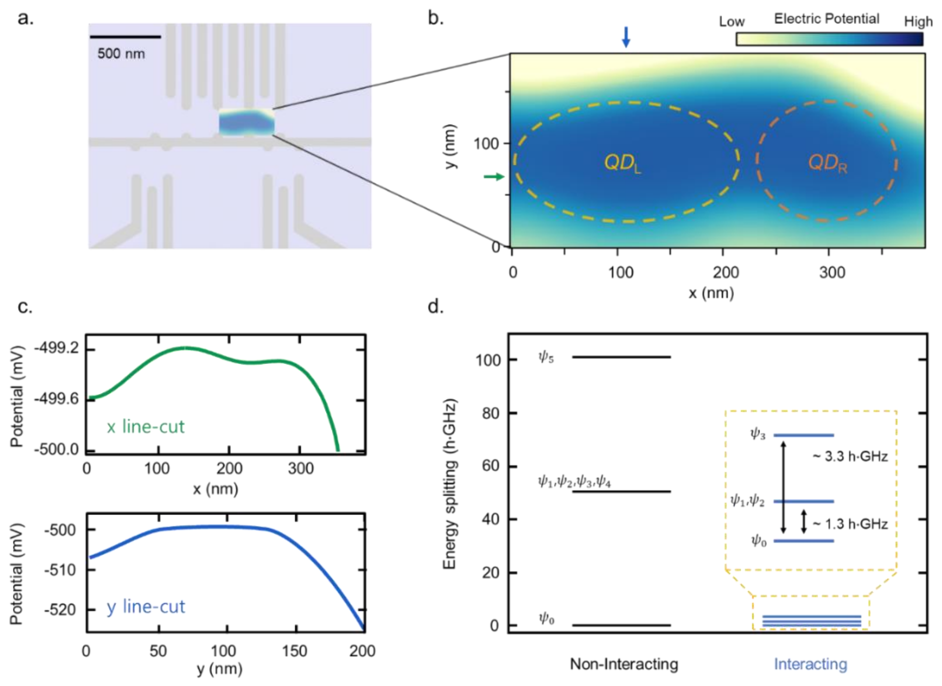

Fig. S5.3 Energy splitting calculation based on Full Configuration Interaction (FCI) method. a. Scaled gate geometry of the QD device used in this work for electrostatic simulation. Electric potential near the double-QD site is simulated by the COMSOL Multiphysics software with the dc-voltages used in the experiment. Semi-classical electron number inside the double quantum dot (integral of the Thomas-Fermi electron density over the quantum dot area) resultant from this gate voltage set was confirmed to be (2,1) **b.** Spatial distribution of the confinement potential near the QD sites. Dashed circles denote the expected position of the QDs where the left QD is expected to be distributed over an oval-shaped area. **c.** Line-cut of the potential along the x (y) direction along the green (blue) arrow in b. **d.** Diagram of the energy splitting with (blue lines) and without (black lines) the electron-electron interaction by the FCI calculation. When the electron-electron interaction is not considered, the energy difference between the ground and the first excited state is ~ 50 h·GHz. The electron-electron interaction quenches the spectrum, resulting in ~ 1.3 h·GHz difference between the ground and the first excited state.

To confirm that it is nevertheless reasonable to assume that the qubit levels behave as a QD hybrid qubit, we measured the magnetic field dependence of the energy splitting. By performing the ac-driven energy spectroscopy at a fixed detuning, we show that the energy splitting has no significant dependence on the magnetic field (Fig. S5.4). This implies the qubit states at the (2,1) configuration have the same S_z and S_{tot}. Based on the observation along with the adiabatic initialization process described in the main text, we interpret the qubit states at the operation regime as the HQ states with $\left|S_{tot}=1/2, S_z=-1/2\right\rangle$.

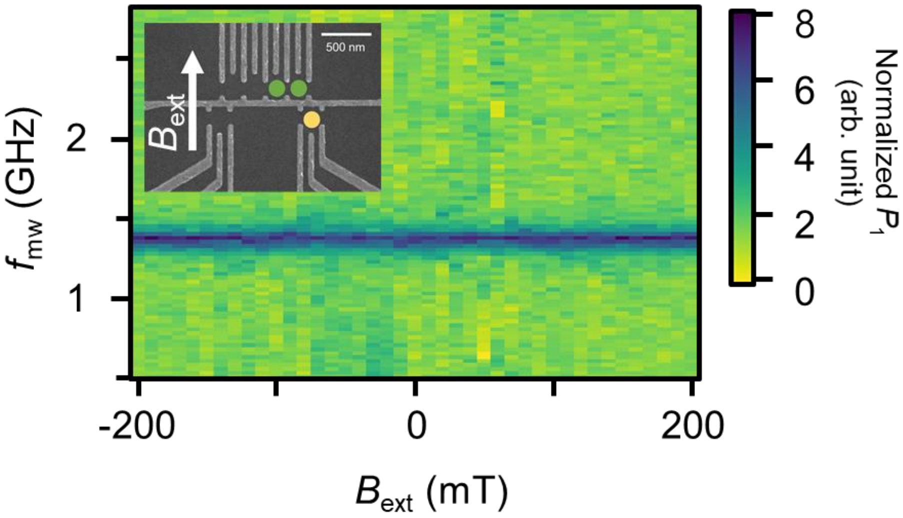

Fig. S5.4 Magnetic field dependence of the energy splitting. Microwave spectroscopy at the qubit frequency ~ 1.4 GHz is performed as a function of the external magnetic field strength, B_{ext}. The magnetic field is applied along the direction shown in the white arrow in the inset.

Following the HQ level spectroscopy demonstrated in Si/SiGe [10], we write the toy model Hamiltonian as,

$$H = \begin{pmatrix} \varepsilon/2 & 0 & t_1 & -t_2 \\ 0 & \varepsilon/2+\delta\mathrm{L} & -t_3 & t_4 \\ t_1 & -t_3 & -\varepsilon/2 & 0 \\ -t_2 & t_4 & 0 & -\varepsilon/2+\delta\mathrm{R} \end{pmatrix} \tag{5}$$

The basis set for the Hamiltonian is {(2,1)*g*, (2,1)*e*, (1,2)*g*, (1,2)*e*} where the *g* and *e* denote the ground and the excited state respectively at each charge configuration. The n (m) in the (n, m) notation indicates the number of electrons in the left (right) quantum dot and ε is the energy detuning between the dots. δL (δR) is the singlet-triplet energy splitting in the left (right) dot, and t_i (i = 1, 2, 3, 4) denotes the tunnel coupling between the different charge states. Figure. S5.5a shows the eigen-energy diagram as a function of ε calculated with the parameter values of $\delta L/h$ =3 GHz, $\delta R/h$ = 95.8 GHz, t_1/h = 1.8GHz, t_2/h = 7.1 GHz, t_3/h = 11.5 GHz, t_4/h = 6.3 GHz. These parameters are obtained by empirically fitting the theoretical spectrum to the experimentally observed energy dispersion (Fig. 5.1b) except $\delta R/h$ = 95.8 GHz, fixed by the measured value described in the main text.

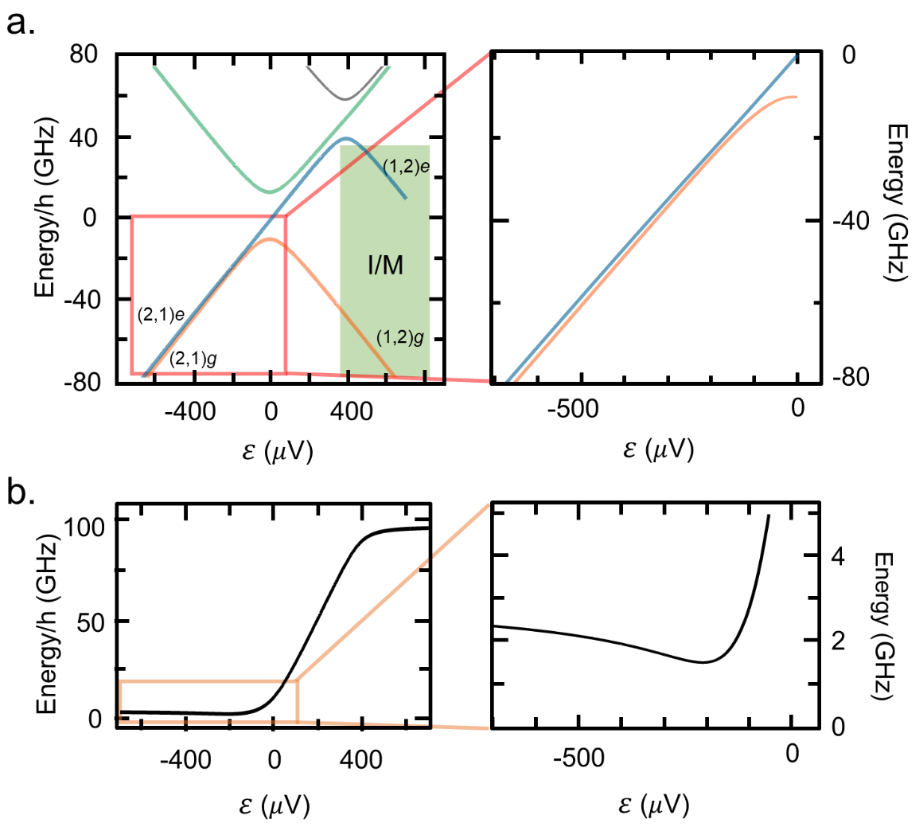

Fig. S5. Energy level simulation a. Eigen-energy levels of the hybrid qubit simulated with the Hamiltonian (5). The Green boxed region is the energy-selective tunneling position for qubit readout and initialization. **b.** Energy splitting between the lowest two energy levels as a function of ε. The right panel of **a.** (**b.**) shows the energy levels (splitting) near the operation point O of the hybrid qubit investigated in the main text.

S5.3. Experimental method

The bulk of the experimental setup utilized in this work is described in Ref. [3]. The lever-arm of both V_1, and V_2 gates in Fig. 1a is 0.028 which is determined from Coulomb diamond measurements. The electron temperature $T_e \approx$ 234 mK is estimated by fitting the Fermi-Dirac distribution curve to the V_2 electron transition line in the single electron regime (Fig. S6a).

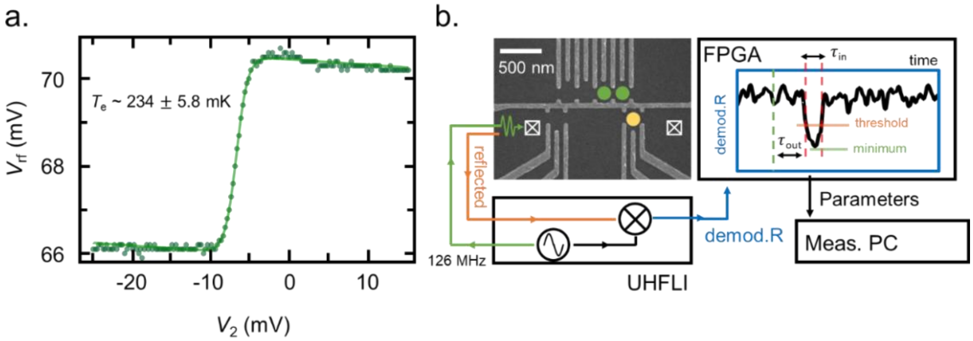

Fig. S6. Experimental methods a. Electron temperature measurement. By fitting the Fermi-Dirac distribution to the electron transition line, electron temperature $T_e \approx$ 234 mK is extracted. **b.** Experimental setup utilized for single-shot readout of the hybrid qubit. The magnitude of the reflected rf-signal is demodulated in a high-frequency lock-in amplifier and is directly put to the field-programmable gate array (FPGA) where the signal is thresholded to discriminate the different qubit states. The FPGA also performs time-tagging of the tunneling events enabling time-resolved tunneling time measurements.

For single-shot detection, as shown in Fig. S6b, the transient tunneling events for qubit state $|1\rangle$ are thresholded in real-time using a field-programmable gate array (FPGA, Digilent Zedboard). The FPGA samples input data with the sampling rate of 1 MSa/s, compares the preset threshold with the data in parallel, and records the bit 1 immediately when data below the threshold value is detected. The bit 0 is recorded when such events did not happen throughout the preset measurement period. The sequence is repeated 5000 times to estimate the probability of the state $|1\rangle$, P_1. The FPGA also tags time after the trigger for each detected tunneling event, and the statistics of the tunneling-out and -in times are gathered to build the histograms shown in Fig. 2 of the main text.

For generating the high-frequency signals at the room-temperature, a high-speed arbitrary waveform generator (AWG, Keysight technologies, M8195A) which supports up to 65 GSa/s sampling rate is utilized. To combine the high-frequency and dc-signals for the gate electrodes, commercial off-board bias-tees (Tektronix, PSPL 5546) which supports > 10 GHz ac-signals are used.

With the high-frequency setup shown above, we demonstrate the coherent charge qubit Larmor oscillation [11] to evaluate the actual signal delay at the gate electrodes. Fig. S7a depicts a scanning electron microscope image of a different GaAs quantum dot device used for the charge qubit measurement, which is placed in the same cryostat with the same high-frequency wiring and circuit board as used in this work. As shown in Fig. S7a, pulses with the opposite polarity, and with the fixed width of 60 ps are generated by two different channel outputs of the AWG to be applied to VP_1 and VP_2 gate electrodes respectively. Sweeping the pulse amplitudes at the AWG output as a function of the relative delay between the two outputs of the AWG reveals a V-shaped coherent oscillation pattern (Fig. S7b). This is because the maximum detuning modulation condition (Fig. S7b, dashed line) is sensitive to the actual delay at the gate electrodes on the order of ~ 20 ps, directly implying the rise-times as short as ~ 20 ps can be transferred to the gate electrodes without further distortion.

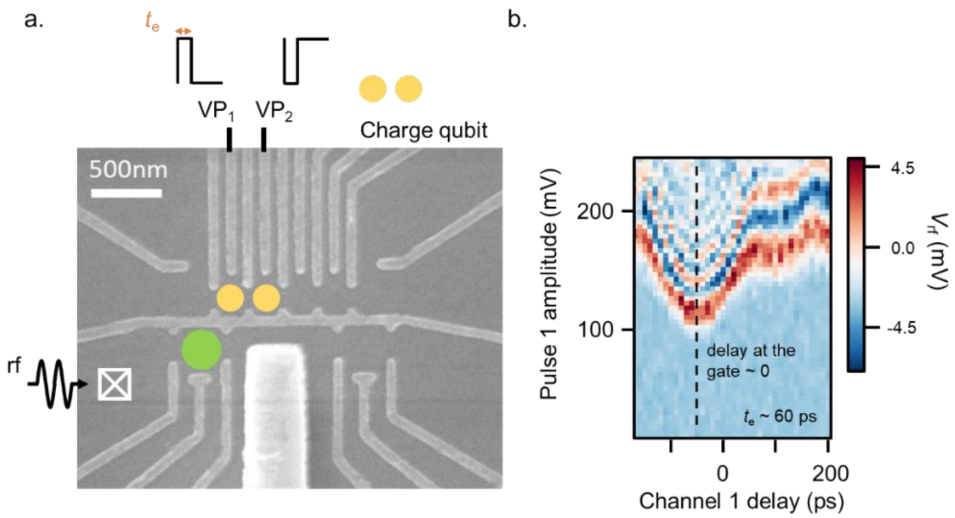

Fig. S7. High-frequency transmission line calibration. a. Scanning electron microscope image of the device used for the charge qubit measurement and cryostat transmission line calibration. Two square pulses of the width, t_e ~ 60 ps with the opposite polarity are applied to VP_1 and VP_2 gate electrodes respectively. The pulses are generated by two different channels in an arbitrary waveform generator (AWG). rf single-electron transistor (rf-set, green dot) detects the charge states of the double quantum dot (yellow dots). **b.** Sweeping the pulse amplitude versus the relative channel delay reveals a V-shaped oscillation pattern. At ~ -50 ps channel delay (dashed line) the delay at the gate electrodes vanishes, ensuring the full 60 ps evolution at the target detuning set by the pulses.

S5.4. Effects of the ramp-in and ramp-out pulse on the measurement fidelity

We discuss the T_1 relaxation time at the operation regime in (2,1) charge configuration, and the effect of the ramp pulse on the read-out visibility. Fig. S8a shows detuning dependent mapping of T_1 times measured with pulse sequence depicted in the inset to Fig. S8a. The minimum T_1 time of 20 ns occurs near the detuning amplitude ε_P ~ - 170 mV in the charge qubit regime, and the increasing T_1 time with respect to charge qubit energy splitting (ε_P > - 170 mV) is consistent with the typical trend observed both in GaAs [2] and Si charge qubits [12] dominated by charge noise-induced relaxation. In the HQ regime (ε_P < - 170 mV), T_1 more rapidly increase away from the anti-crossing showing reduced susceptibility to charge noise.

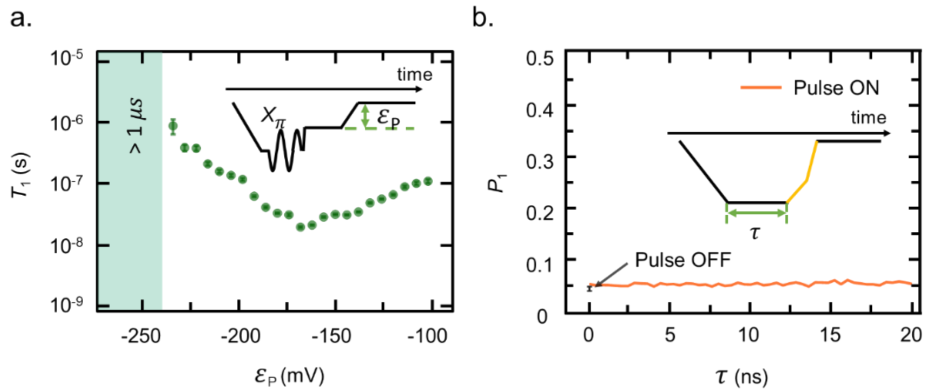

Fig. S8. Detuning dependent T_1 times and effects of ramp pulses. a. T_1 times measured in the qubit operation regime as a function of the detuning amplitude ε_P. Inset: Schematic pulse sequence used for the T_1 measurement. **b.** P_1 as a function of dwell time τ of the adiabatic ramp-only pulse depicted in the inset showing negligible change compared with the pulse turned-off. $P_1 \sim 0.04$ is due to thermal tunneling events by the state $|0\rangle$ within the 140 μs long measurement window.

The measured $T_1(\varepsilon)$ is used for investigating the effect of adiabatic ramps, during which probability leakage or energy relaxation can in principle lead to visibility loss. As shown in the inset to Fig. S8b, the two-stage ramp-out sequence is utilized to avoid the relaxation hot-spot in charge qubit regime but maintain the adiabaticity. By solving the master equation with the toy-model Hamiltonian (5) given in S2, we confirm that the leakage probability during the ramp-in stage is kept below 0.1 %. Accumulated state relaxation probability during the ramp-out near the relaxation hot-spot is $\approx 1\%$. Moreover, a relatively fast second ramp-out stage (rise time 2 ns) results in an unintentional Landau-Zener transition probability of less than ≈ 1 %.

Fig. S8b shows the experimentally observed P_1 as a function of dwell time τ of the adiabatic ramp-only pulse. Although independent measurement of the state leakage or non-adiabaticity probability is challenging, the result shows that readout errors due to unintended non-adiabatic state transition during ramp or state leakage out of computational qubit states are less than 2 % consistent with the calculation. Due to the thermal tunneling probability of the state $|0\rangle$ for the given measurement duration of 140 μs, about 4% offset is measured even when the pulse is turned off, and this effect is included in the measurement fidelity analysis in the main text and in S5. We expect that there is room for improvement to reduce the unwanted state $|0\rangle$ tunneling by applying adaptive adjustment of readout duration by further FPGA implementation and including fast initialization pulse sequence using, for example, the observed relaxation hot-spot in the charge qubit regime (Fig. S8a).

S5.5. Readout fidelity analysis

Following the Ref. [13] the single-shot traces are numerically generated with the experimentally obtained parameters. By randomly assigning the qubit states to traces according to a parameter p_1 which corresponds to the probability for qubit $|1\rangle$ state, 8,000 single-shot traces are generated. For the case of the $|1\rangle$ state if a random variable, p_r, in the range [0,1] is larger than the relaxation proability calculated from the T_1 relaxation time and the total measrement time, a rectangular tunneling peak which follows the statistics set by the tunneling-in / -out times (Fig.

2a) is generated. In case of the $|0\rangle$ state, if a random variable, p_t, in the range [0,1] is smaller than the thermal tunneling probability obatined in Fig. S8b, a tunneling peak is generated. For each $|0\rangle$ and $|1\rangle$ trace, random gaussian noise is added and the numerical low pass filter similar to the experiment is applied. By sampling the minimum value from each trace, the histogram of the minimum values can be obtained to be compared with the experimentally acquired histogram. After the filtering process, p_1 and the gaussian noise amplitude are optimized to fit the simulated histogram to the experimental curve.

Because the information on the spin state for each simulated trace is given in priori, separate histograms corresponding to $|0\rangle$ and $|1\rangle$ states can be acquired respectively. From the separate histograms, measurement fidelity for $|0\rangle$, $F_0(V_\mathrm{t}) = \int_{V_\mathrm{t}}^{\infty} n_0(V)\mathrm{d}V$ and $|1\rangle$, $F_1(V_\mathrm{t}) = \int_{-\infty}^{V_\mathrm{t}} n_1(V)\mathrm{d}V$ are evaluated along the threshold voltage V_t, where the n_0 (n_1) corresponds to the normalized histogram of the $|0\rangle$ ($|1\rangle$). By choosing the optimal threshold that maximizes the visibility, $v(V_\mathrm{t}) \equiv F_0(V_\mathrm{t}) + F_1(V_\mathrm{t}) - 1$ the $|0\rangle$ ($|1\rangle$) measurement fidelity 95.4 % (97.3 %), and the visibility 92.6 % are obtained.

Supplementary references

[1] C. H. Yang, A. Rossi, N. S. Lai, R. Leon, W. H. Lim, and A. S. Dzurak, Charge State Hysteresis in Semiconductor Quantum Dots, *Appl. Phys. Lett.* **105**, 183505 (2014).

[2] O. E. Dial, M. D. Shulman, S. P. Harvey, H. Bluhm, V. Umansky, and A. Yacoby, Charge Noise Spectroscopy Using Coherent Exchange Oscillations in a Singlet-Triplet Qubit, *Phys. Rev. Lett.* **110**, 146804 (2013).

[3] W. Jang, J. Kim, M.-K. Cho, H. Chung, S. Park, J. Eom, V. Umansky, Y. Chung, and D. Kim, Robust Energy-Selective Tunneling Readout of Singlet-Triplet Qubits under Large Magnetic Field Gradient, *npj Quant. Inf.* **6**, 64 (2020).

[4] B.-B. Chen, B.-C. Wang, G. Cao, H.-O. Li, M. Xiao, G.-C. Guo, H.-W. Jiang, X. Hu, and G.-P. Guo, Spin Blockade and Coherent Dynamics of High-Spin States in a Three-Electron Double Quantum Dot, *Phys. Rev. B* **95**, 035408 (2017).

[5] J. Corrigan, J. P. Dodson, H. E. Ercan, J. C. Abadillo-Uriel, B. Thorgrimsson, T. J. Knapp, N. Holman, T. McJunkin, S. F. Neyens, E. R. MacQuarrie, R. H. Foote, L. F. Edge, M. Friesen, S. N. Coppersmith, and M. A. Eriksson, Coherent Control and Spectroscopy of a Semiconductor Quantum Dot Wigner Molecule, *arXiv*:2009.13572 [Cond-Mat, Physics:Quant-Ph] (2020).

[6] S. Pecker, F. Kuemmeth, A. Secchi, M. Rontani, D. C. Ralph, P. L. McEuen, and S. Ilani, Observation and Spectroscopy of a Two-Electron Wigner Molecule in an Ultraclean Carbon Nanotube, *Nat. Phys.* **9**, 576 (2013).

[7] A. Szabo and N. S. Ostlund, Modern Quantum Chemistry: Introduction to Advanced Electronic Structure Theory, Reprint Edition (Dover Publications, Mineola, N.Y, 1996).

[8] SciPy 1.0 Contributors, P. Virtanen, R. Gommers, T. E. Oliphant, M. Haberland, T. Reddy, D. Cournapeau, E. Burovski, P. Peterson, W. Weckesser, J. Bright, S. J. van der Walt, M. Brett, J. Wilson, K. J. Millman, N. Mayorov, A. R. J. Nelson, E. Jones, R. Kern, E. Larson, C. J. Carey, İ. Polat, Y. Feng, E. W. Moore, J. VanderPlas, D. Laxalde, J. Perktold, R. Cimrman, I. Henriksen, E. A. Quintero, C. R. Harris, A. M. Archibald, A. H. Ribeiro, F. Pedregosa, and P. van Mulbregt, SciPy 1.0: Fundamental Algorithms for Scientific Computing in Python, *Nat Methods* **17**, 261 (2020).

[9] R. Okuta, Y. Unno, D. Nishino, S. Hido, and C. Loomis, *CuPy: A NumPy-Compatible Library for NVIDIA GPU Calculations*, 7 (n.d.).

[10] Z. Shi, C. B. Simmons, D. R. Ward, J. R. Prance, X. Wu, T. S. Koh, J. K. Gamble, D. E. Savage, M. G. Lagally, M. Friesen, S. N. Coppersmith, and M. A. Eriksson, Fast Coherent Manipulation of Three-Electron States in a Double Quantum Dot, *Nat. Commun.* **5**, 3020 (2014).

[11] K. D. Petersson, J. R. Petta, H. Lu, and A. C. Gossard, Quantum Coherence in a One-Electron Semiconductor Charge Qubit, *Phys. Rev. Lett.* **105**, 246804 (2010).

[12] D. Kim, D. R. Ward, C. B. Simmons, J. K. Gamble, R. Blume-Kohout, E. Nielsen, D. E. Savage, M. G. Lagally, M. Friesen, S. N. Coppersmith, and M. A. Eriksson, Microwave-Driven Coherent Operation of a Semiconductor Quantum Dot Charge Qubit, *Nat. Nanotechnol.* **10**, 243 (2015).

[13] A. Morello, J. J. Pla, F. A. Zwanenburg, K. W. Chan, K. Y. Tan, H. Huebl, M. Möttönen, C. D. Nugroho, C. Yang, J. A. van Donkelaar, A. D. C. Alves, D. N. Jamieson, C. C. Escott, L. C. L. Hollenberg, R. G. Clark, and A. S. Dzurak, Single-Shot Readout of an Electron Spin in Silicon, *Nature* **467**, 687 (2010).

Chapter 6. Wigner-molecularization-enabled dynamic nuclear field programming

Abstract

Multielectron semiconductor quantum dots (QDs) provide a novel platform to study the Coulomb interaction-driven, spatially localized electron states of Wigner molecules (WMs). Although Wigner-molecularization has been confirmed by real-space imaging and coherent spectroscopy, the open system dynamics of the strongly-correlated states with the environment are not yet well understood. Here, we demonstrate efficient control of spin transfer between an artificial three-electron WM and the nuclear environment in a GaAs double QD. A Landau–Zener sweep-based polarization sequence and low-lying anti-crossings of spin multiplet states enabled by Wigner-molecularization are utilized. Combined with coherent control of spin states, we achieve control of magnitude, polarity, and site dependence of the nuclear field. We demonstrate that the same level of control cannot be achieved in the non-interacting regime. Thus, we confirm the spin structure of a WM, paving the way for active control of correlated electron states for application in mesoscopic environment engineering.

This chapter is adapted from *arXiv:*2207.11655 (2022).

Semiconductor quantum dot (QD) systems facilitate investigations of the interaction between electron spins and nuclear environments, which is known as the central-spin problem [1,2]. Although the fluctuation of nuclear fields, which is quantified by the effective Overhauser field B_{nuc} [3,4], often acts as a magnetic-noise source for spin qubits [3], the hyperfine electron–nuclear spin interaction allows to achieve dynamic nuclear polarization (DNP) [5–8]. DNP is used for enhancing the signal-to-noise ratio in nuclear magnetic resonance [6] and prolonging coherence times in QD-based spin qubits [9,10]. Gate-defined semiconductor QDs have been used to achieve the fast probing of nuclear environments [8,11,12], bidirectional DNP [11], and active feedback control of nuclear fields [10].

Although DNP achieved by the pulsed-gate technique is more relevant for quantum information applications compared to spin-flip mediated transport with an applied bias [13,14], spin qubit control combined with DNP has been limited to two-electron singlet–triplet (ST_0) spin qubits [9–12,15]. Despite the versatility of gate-defined QD systems [16–19], the large singlet-triplet energy splitting E_{ST} (~10^2 h·GHz; h is Planck's constant) in particular in GaAs limits the access to higher spin states [20] in multielectron QDs at moderate external magnetic fields $B_0 < 1$ T or within a typical frequency bandwidth of experimental setups.

Coulomb-correlation-driven Wigner molecules (WMs) in confined systems [21–24] may provide new directions for expanding nuclear control to multielectron systems. Recent studies on QDs in various systems have shown clear evidence of WM formation [22,23,25–28]. It has been demonstrated that the E_{ST} can reach down to ~10^0 h·GHz upon the WM formation [25,27] because of strong electron-electron interactions confirmed by full-configuration interaction (FCI)-based theories [23,28,29]. However, most studies have focused on the spectroscopic confirmation of WM formation, and studies on the open system dynamics using correlated states have not been reported to date.

Here, we demonstrate the formation of a WM in semiconductor QDs, which helps achieving efficient spin environment control. We use a gate-defined QD in GaAs and exploit the quenched energy spectrum of the WM (E_{ST} ~ 0.9 h·GHz) to enable mixing between different S_z subspaces within $B_0 < 0.5$ T, where S_z denotes the spin projection to the quantization axis. Furthermore, we demonstrate DNP by pulsed-gate control of the electron spin states. Leakage spectroscopy and Landau–Zener–Stuckelberg (LZS) oscillations confirm a sizable bidirectional change in B_{nuc} ~ 80 mT and the spatial Overhauser field gradient ΔB_{nuc} ~ 35 mT due to the long nuclear spin diffusion time τ_N ~ 62 s. Further, we demonstrate on-demand control of B_{nuc} combined with coherent LZS oscillations, providing a new route for realizing programmable DNP using correlated electron states.

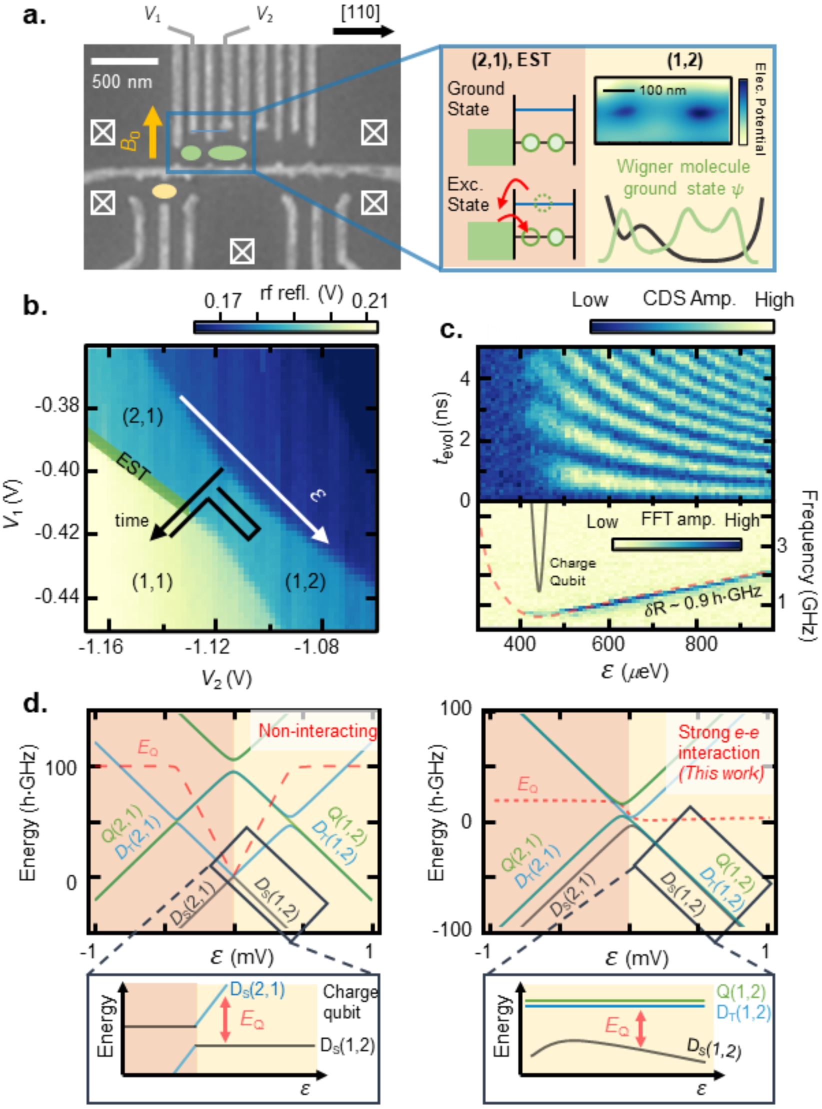

Figure 6.1. Wigner molecule formation in a GaAs double quantum dot. a. Scanning electron microscope image of a GaAs quantum dot (QD) device similar to the one used in the experiment. Green dots denote the double QD defined for Wigner molecule (WM) formation which is aligned along the [110] crystal axis (black arrow). The inner plunger gate V_2 is designed to have anisotropic confinement potential as shown in the right panel to facilitate the localization of the electronic ground state. Yellow circle: a radio-frequency (rf) single-electron transistor (rf-SET) charge sensor for rf-reflectometry. External magnetic field B_0 is applied along the direction denoted by the yellow arrow. **b.** Charge stability diagram of the double QD near the three-electron region spanned by V_1 and V_2 gate voltages. Green shaded region: the energy-selective tunneling (EST) position for the state readout and initialization. **c.**

Landau–Zener–Stückelberg (LZS) oscillation of the WM at B_0 = 0 T. The relative phase evolution between the excited doublet (D_T) and the ground doublet (D_S) results in the oscillation captured by the EST readout. Red-dashed curve in the fast Fourier transformed (FFT) map shows energy dispersion calculated from the toy-model Hamiltonian. The calculation yields quenched orbital energy spacing of the inner dot δR ~ 0.9 h·GHz. **d.** Left (Right) panel: Energy spectrum along the (2,1)–(1,2) charge configuration in the non-interacting (strongly interacting, this work) regime with δL ~ 100 h·GHz (δL ~ 19 h·GHz), and δR ~ 100 h·GHz (δR ~ 0.9 h·GHz).

Results

Figure 6.1a shows a gate-defined QD device fabricated on a GaAs/AlGaAs heterostructure, where a 2D electron gas (2DEG) is formed ~70 nm below the surface (see Methods). We focus on the left double QD (DQD) containing three electrons. We designed the V_2 gate to form an anisotropic potential, which is predicted to promote WM formation [22]. An electrostatic simulation of the electric potential at the QD site near V_2 shows an oval-shaped confinement potential with anisotropy exceeding 3 (Fig. 6.1a, right panel). This potential can be tuned by the gate voltage, allowing the controlled electron correlation and localization of the ground state wavefunction within the DQD [22,24,26,27]. The yellow dot in Fig. 6.1a. denotes a radio-frequency single-electron transistor (rf-SET) charge sensor utilized for quantum state readout [30–32]. The device was operated in a dilution refrigerator with a base temperature of ~40 mK, an electron temperature T_e ~150 mK (Supplementary Note 6.1), and a variable B_0 applied to the direction shown in Fig. 6.1a.

First, we show the spectroscopic evidence of the WM at B_0 = 0 T by probing E_{ST} in the right QD δR. Fig. 6.1b shows a charge stability diagram. The green-shaded region near the (2,1)–(1,1) charge transition is exploited for energy-selective tunneling (EST) readout and state initialization [27,33,34]. We tune the electron tunneling-in (-out) time τ_{in} (τ_{out}) of the left dot to 14 (7) μs. Starting from the initialized ground doublet state D_{S} in the (2,1) charge configuration, we apply non-adiabatic pulses (Fig. 6.1b) simultaneously to V_1 and V_2 with a rise time of ~500 ps and a repetition period of 51 μs $\gg$ τ_{in} to induce coherent LZS oscillation [35,36]. The oscillation reveals the relative phase evolution between the excited and ground doublet states (D_{T} and D_{S}), the frequency of which is governed by δR.

Fig.6.1c shows the resultant LZS oscillations as a function of evolution time t_{evol} and detuning ε. The E_{ST} in GaAs DQDs in the non-interacting regime is typically on the order of 10^2 h·GHz [20] (Fig. 6.1d). In a charge qubit regime, a steep rise in the LZS oscillation frequency f_{LZS} as a function of ε (Fig. 6.1c, black curve) and short coherence time T_2^* ~ 10 ps due to strong susceptibility to charge noise is expected [37]. However, we find a significantly smaller f_{LZS} in the (1,2) charge configuration and T_2^* ~ 10 ns because of the reduced dispersion of f_{LZS} versus ε. This is a reminiscent of a QD hybrid qubit [27,36,38], but the excited energy is suppressed owing to the electron–electron interaction. WM formation in our previous GaAs device has been recently confirmed by FCI calculation [27–29]. Although such calculation is needed to rigorously determine parameters, we roughly estimate δR ~ 0.9 h·GHz, by fitting the fast Fourier transformed (FFT) spectrum to the calculation result (Fig. 6.1c, red-dashed curve) derived from a toy-model Hamiltonian [33,35,36] (see Methods).

The full energy spectrum calculation of the three-electron states using the parameters obtained experimentally across the (2,1)–(1,2) configuration is illustrated in Fig. 6.1d (right panel). The suppressed E_{ST} of the left dot δL ~ 19 h·GHz is obtained by measuring the width of the EST region in the charge stability diagram with the lever arm of the gate V_1 ~ 0.03. Because of the small value of $\delta L/(k_B T_e)$ ~ 6, where k_B is Boltzmann's constant, thermal tunneling precludes high-fidelity single-shot readout. We obtain data by the time-averaged signal using the correlated-double sampling (CDS) method, which effectively yields the signal proportional to the excited state probability [33] (see Supplementary Note 6.2).

We confirm the WM spin structure via the strongly suppressed energy spectrum in the right QD with varying B_0. We focus on five low-lying energy levels among eight possible multiplet states. See Methods for notations used for labeling spin multiplets. Hereinafter, n (m) denotes the number of electrons in the left (right) dot by (n, m; S_z). As Fig. 6.2a (left panel), D_S(1,2;−1/2) (D_S(1,2;1/2)) becomes degenerate with D_T(1,2;1/2) or Q(1,2;1/2) (Q(1,2;3/2)) at a certain ε depending on the B_0 magnitude. The degeneracies are lifted by the transverse Overhauser field $B_{nuc}^{\perp}$ [8,11]. To detect such anti-crossings, we first initialize the state to either D_S(2,1;−1/2) or D_S(2,1;1/2) at the EST position. By pulsing the initialized D_S(2,1;−1/2) (D_S(2,1;1/2)) towards (1,2) and holding for ~100 ns ≫ T_2^*, mixing with (or leakage to) states Q(1,2;1/2) or D_T(1,2;1/2) (Q(1,2;3/2)) can occur if the pulse amplitude A_p coincides with the anti-crossing position (Fig. 6.2a, right panel). Upon pulsing back to the (2,1) charge configuration, the resultant excited states Q or the D_T probability can be detected via EST [27,33,34]. Fig. 6.2b shows the leakage spectrum versus A_P and B_0, mapping out the anti-crossing positions similar to "spin-funnel" measurements in two-electron ST_0 qubits reproducing the energy splittings between the ground and excited levels [8,16,39,40]. The black (red) dashed curves show the calculated splittings (Fig. 6.1d) between the D_S and D_T (Q) states at $B_0 = 0$ T, with the Lande g-factor $g^* \sim -0.4$ [41,42].

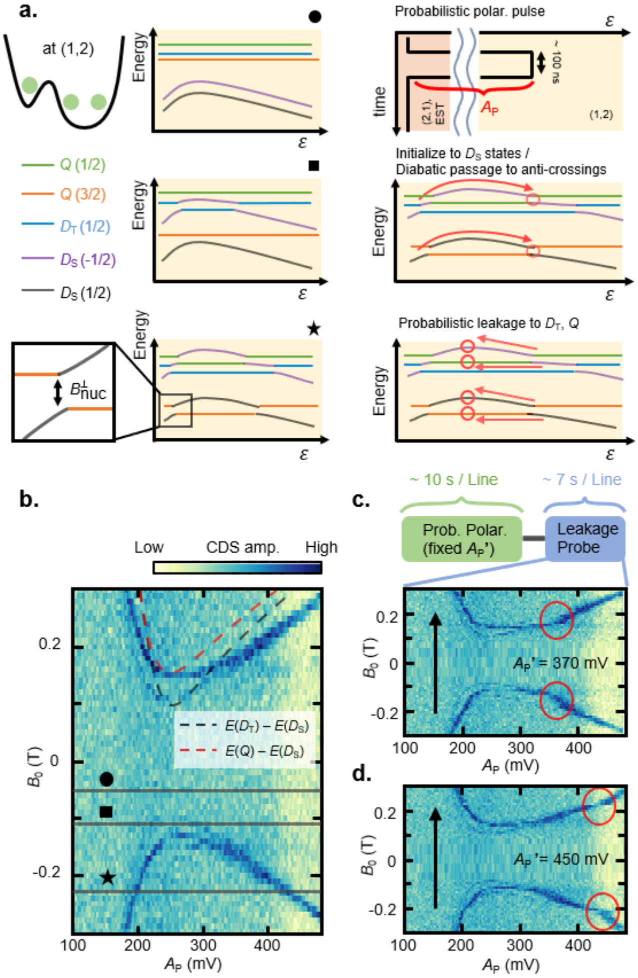

Figure 6.2. Leakage spectroscopy and probabilistic nuclear polarization with the Wigner molecule. a. Left panel: schematics of the energy levels for different external magnetic fields $B_0 > 0$ T. Crossings between different S_Z states become anti-crossings aided by the transverse nuclear Overhauser field. Right panel: schematic of the pulse sequence for leakage spectroscopy and probabilistic dynamic nuclear polarization (DNP). The pulse diabatically drives the initialized $D_S(2,1;1/2)$ ($D_S(2,1;-1/2)$) to (1,2), and hold ε for 100 ns $\gg$ T_2^*. Upon the coincidence of the pulse detuning and the anti-crossing, the state probabilistically evolves to $Q(1,2;3/2)$ ($Q(1,2;1/2)$) and flips the electron spin $\Delta m_S = +1$ which accompanies $\Delta m_N = -1$. **b.** Leakage spectroscopy of the Wigner molecule (WM) state as a function of B_0 and the pulse amplitude A_p. Black (Red) dotted curve shows the calculated energy splitting between D_T (Q) and D_S at B_0 = 0 T. Measurement-induced nuclear field shifts the dispersion opposite to the direction of B_0. **c. (d.)** Leakage measurement with an additional probabilistic polarization pulse with amplitude A_p' applied before

each line sweep. The A_p' is fixed to 370 (450) mV, and the additional distortion in the leakage spectrum is shown as red circles near a pulse amplitude of 370 (450) mV. Black arrows denote the magnetic field sweep direction.

Although the calculated curve qualitatively agrees with the experimental curve, the observed spectrum curvature as a function of A_P and B_0 is smaller because of the DNP induced by the pulse sequence used for leakage spectroscopy. To confirm this, before each line scan of A_p in Fig. 6.2c (2d), a similar step pulse with a fixed amplitude A_P' ~ 370 mV (450 mV) is applied for 10 s. Consequently, we observe distortions (red circles) in the spectrum occurring at A_P'. This is because, when A_P' matches with the anti-crossing position, the pulse probabilistically flips the electron spin with a change in the angular momentum $\Delta m_S = +1$ by the leakage process described above and accompanies flop $\Delta m_N = -1$ of the nuclear spin [8,11]. Unlike the electrons in GaAs, nuclei have positive *g*-factors [8,20] ; therefore, the pulse polarizes B_{nuc} toward the B_0 direction. This additionally drags the leakage spectrum opposite to the B_0 direction under a specific condition $A_p = A_P$'. These results indicate that leakages induced by hyperfine interaction between the WM and nuclear environment lead to an observable change in B_{nuc}. Despite the long measurement time per line scan (~7 s) owing to the communication latency between the measurement computer and the instruments, the polarization effect is still visible. Thus, $\tau_N > 10$ s, as discussed below. Moreover, as the anti-crossing position is a sensitive function of $B_{tot} = B_0 + B_{nuc}$ over 100 ~ 300 mT, it can be used to measure B_{nuc}.

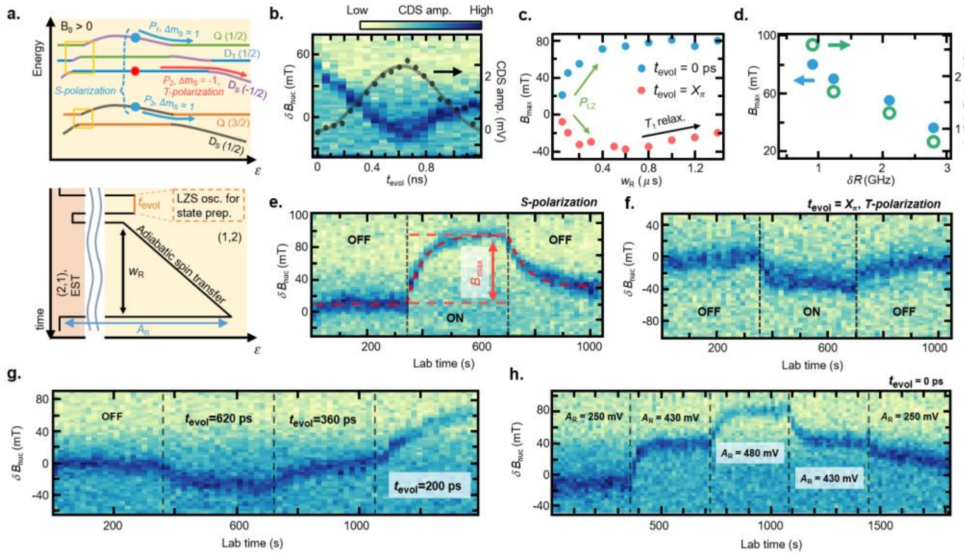

Figure 6.3. Bidirectional and programmable dynamic nuclear polarization enabled by Wigner molecularization. a. Top panel: Schematic of the anticrossings used for deterministic dynamic nuclear polarization (DNP). Bottom panel: pulse sequence used for S- and T-polarizations. For t_{evol} = 0 ns, the sequence corresponds to maximum S-polarization, which brings $D_S(1,2;1/2)$ ($D_S(1,2;-1/2)$ adiabatically across the anti-crossing to $Q(1,2;3/2)$ ($Q(1,2;1/2)$) flipping the electron spin with $\Delta m_S = +1$ and leading to $\Delta m_N = -1$ (blue arrow, S-polarization). For t_{evol} = 600 ns, the sequence corresponds to maximum T-polarization. Herein, the $D_T(1,2;1/2)$ prepared with a (Landau–Zener–Stückelberg) LZS-oscillation-induced π-pulse is adiabatically transferred to $D_S(1,2;1/2)$, resulting in $\Delta m_S = -1$ and $\Delta m_N = +1$ (red arrow, T-polarization), which has the opposite polarization effect compared to S-polarization. **b.** Change in the nuclear field δB_{nuc} as a function of t_{evol}. The gray curve shows the corresponding LZS oscillation measurement reflecting the D_T population. The δB_{nuc} oscillates out of phase to the LZS oscillation owing to the oscillation of the S- and T-polarization ratio. **c.** The magnitude of the maximum polarization B_{max} as a function of ramp time w_R. The B_{nuc} saturates to B_{max} when the polarization and the nuclear spin diffusion rate reach an equilibrium. For small w_R, the $|B_{max}|$ decreases because of the small Landau–Zener transition probability P_{LZ} for both S- (blue circle) and T-polarizations (red circle). In the case of T-polarization, $|B_{max}|$ decreases again for long w_R owing to the lattice relaxation of the excited population. **d.** B_{max} as a function of δR. The polarization gets more efficient for smaller δR indicating a strong dependence of the nuclear polarization efficiency on the Wigner parameter. **e. (f.)** Dynamic nuclear control with the S (T)-polarization sequence. The red dotted line is the numerical fit derived from the simple rate equation-based model. The fit yields the nuclear spin diffusion time τ_N ~ 62 s, with a polarization magnitude per spin flip

of ~2.58 $h \cdot \mathrm{kHz} \cdot (g^* \mu_B)^{-1}$. **g.** On-demand nuclear field programming via t_{evol}. **h.** Adiabatic ramp amplitude A_R with t_{evol} = 0 ns realizing self-limiting nuclear field programming.

We now show bidirectional DNP combined with coherent control of doublet states at B_0 = 230 mT. Fig. 6.3a (top panel) shows the three primary paths through the anti-crossings, which can flip the electron spins deterministically by adiabatic passage [2,8,11]. Paths P_1 and P_3 describe the S-polarization that flips the electron spin with Δm_S = +1. This is enabled by initializing the state to D_S(1,2;-1/2) (D_S(1,2;1/2)) at the EST position and then by non-adiabatically pulsing beyond the first anti-crossings near the (2,1) charge configuration (Fig. 6.3a, yellow boxes), followed by adiabatically driving the state through the anti-crossing to Q(1,2;1/2) (Q(1,2;3/2)), which accompanies $\Delta m_N = -1$ (Fig. 6.3a, blue arrows). The Q(1,2;1/2) (Q(1,2;3/2)) state is diabatically driven back to the EST position, and one electron quickly tunnels out to the reservoir. Reloading an electron from the reservoir reinitializes one of the Ds states completing the polarization cycle. Both the D_S(1,2;-1/2) and D_S(1,2;1/2) initial states contribute to the S-polarization. Path P_2 denotes the T-polarization ($\Delta m_S = -1$, $\Delta m_N = +1$), which is possible by driving D_T(1,2;1/2) adiabatically to D_S(1,2;-1/2) (Fig. 6.3a, red arrow). To prepare D_T(1,2;1/2), we apply a π-pulse to D_S(2,1;1/2) before the adiabatic passage (Fig. 6.3a, bottom panel). The T-polarization is possible only when the state is initialized to D_S(2,1;1/2) at the EST position.

Combining the S- and T-polarizations, we measure the change in B_{nuc} (δB_{nuc}), where the repeated polarization pulse sequence (Fig. 6.3a, bottom panel) with variable t_{evol} and a repetition rate of ~ 20 kHz is applied for 10 s before each line scan. For Fig. 6.3b, a waiting time ~10 min was added after each sweep to allow the polarized nuclei to diffuse and minimize the polarization effect in the next sweep. As shown in Fig. 6.3b, δB_{nuc} oscillates with t_{evol} , which is anti-correlated with the LZS oscillation that represents the population of $D_T(1,2;1/2)$. This confirms that the net polarization rates can be controlled by adjusting t_{evol}. Accordingly, we calibrate t_{evol} = 0 (0.62 ns) for S (T)-polarization. We also calibrate the duration of the adiabatic spin transfer w_R. Fig. 6.3c shows the maximum nuclear field change B_{max} reachable as a function of w_R, where both S- and T- polarizations are ineffective for short w_R because of negligible adiabatic transfer probability P_{LZ} [2,43]. $|B_{max}|$ reaches a maximum around w_R ~ 0.8 μs, after which the maximum efficiency is retained for the S-polarization sequence. In the case of T-polarization, however, for long w_R, $|B_{max}|$ decreases because of D_T relaxation during the adiabatic passage.

By tuning δR via the dc gate voltages and performing similar S-polarization experiments, we find that B_{max} decreases with increasing δR (Fig. 6.3d, see Extended Data Fig. 6.1). As is discussed subsequently, we find that the nuclear diffusion time scale exceeds 60 s regardless of δR, but the Overhauser field change per electron flip b_0 is strongly suppressed with increasing δR. Ultimately, the observation implies that the pulsed-gate-based nuclear control becomes inefficient in the non-interacting regime.

Returning to the condition δR ~ 0.9 h·GHz, we demonstrate on-demand nuclear field programming. Fig. 6.3e (3f) shows the result of optimized S (T)-polarization with t_{evol} = 0 ns, w_R = 1000 ns (t_{evol} = 0.62 ns, w_R = 600 ns). Although the local fluctuations of the nuclear spins lead to random drift of the anti-crossing positions without the polarization pulse, B_{nuc} builds toward (opposite to) the B_0 direction faster than the nuclear spin diffusion timescale when the polarization pulse is applied before each line scan. δB_{nuc} rises to B_{max} 80 mT (−40 mT) until a dynamic equilibrium is reached. Because only the S_Z = 1/2 states contribute to the T-polarization, $|B_{\mathrm{max}}|$ for the T-polarization is about half of that for the S-polarization, implying that the state initialize to both S_Z states with nearly equal probability at the EST position.

We also demonstrate bidirectional DNP by adjusting t_{evol} in Fig. 6.3g. Fig. 6.3h illustrates the programming of B_{nuc} by adjusting the adiabatic sweep amplitude A_R of the S-polarization sequence. Because B_{nuc} builds in the B_0 direction and drives the anti-crossing to deeper ε (more to (1,2) charge configuration) under the S-polarization, A_R serves as the limiting factor of B_{max}. Thus, a self-limiting DNP protocol can be realized.

Using a simple rate equation, we simulate the polarization-probe sequence (red-dashed curve in Fig. 6.3e, see Methods and Supplementary Note 6.3) and obtain $\tau_N \sim 62$ s and $b_0 \sim 2.58\ h\cdot\mathrm{kHz}\cdot(g^*\mu_B)^{-1}$ from the fit. In contrast, the DNP effect is negligible in our device with the two-electron ST_0 qubit [8] under the same repetition rate as in the WM regime (see Supplementary Note 6.4). Through optimization of the magnitude and direction of B_0, $b_0 \sim 3\ h\cdot\mathrm{kHz}\cdot(g^*\mu_B)^{-1}$ can be achieved with an ST_0 qubit in GaAs [2,8]. However, the obtained result shows that robust nuclear control can be achieved with WMs even in the regime where the same level of control cannot be achieved with an ST_0 qubit. In addition, residual polarization ~21.5 mT exists after turning off the polarization sequence (Fig. 6.3e), which diffuses within ~30 min. The large Knight shift gradient originating from the non-uniformly broadened WM wavefunction may be a possible cause of the long τ_N. However, the newly observed phenomena in this study, including the dependence of b_0 on the tuning condition, require further investigations [44,45].

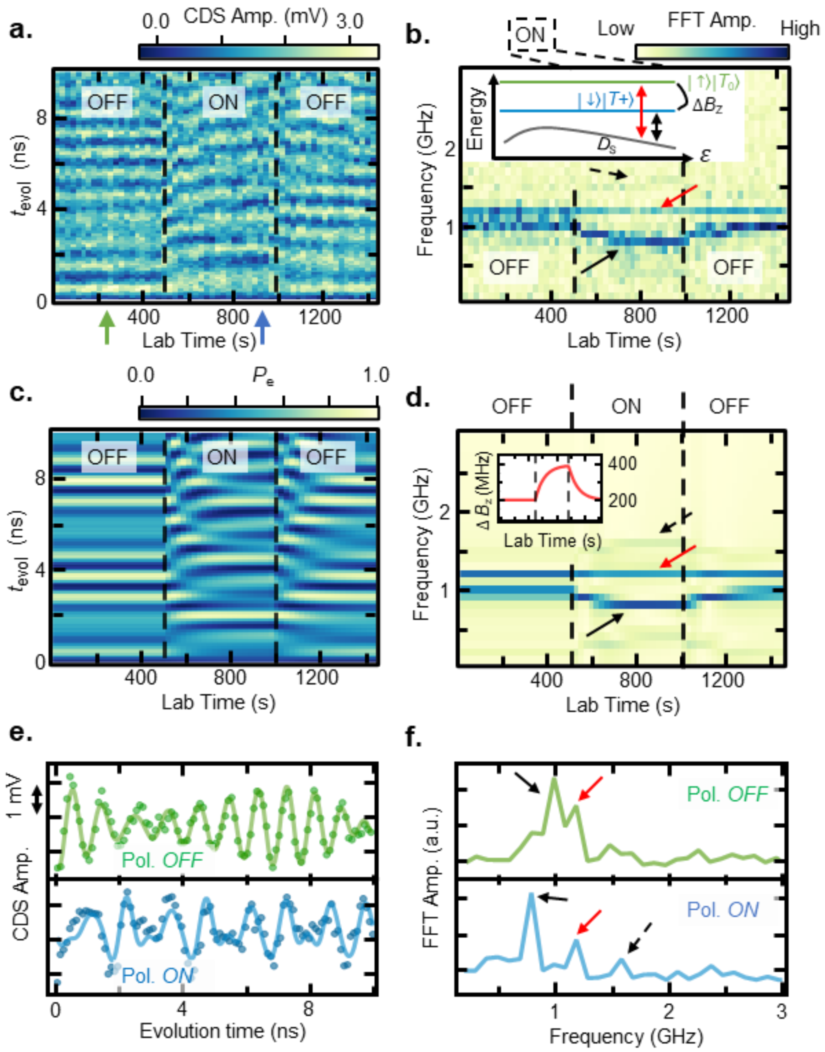

Figure 6.4. Field gradient control and measurement. Landau–Zener–Stückelberg (LZS) oscillation of the Wigner molecule (WM) states at B_0 = 230 mT in **a.** the time domain and **b.** the frequency domain with the S-polarization sequence. The oscillation reveals the relative phase oscillation of the $D_{T1} - D_S$ (black arrow, black dotted arrow) and $D_{T0} - D_S$ (red arrow) of both the $S_Z = 1/2$ and $S_Z = -1/2$ states. The $D_{T0} - D_S$ splitting is constant regardless of the magnetic field gradient ΔB_Z, whereas the $D_{T1} - D_S$ energy spacing is modulated by the ΔB_Z depending on the sign of ΔB_Z and S_Z. The resultant beating is visible in **e.** **(f.)** the time (frequency) domain line-cut when the polarization is on (green arrow in **a.**) and off (blue arrow in **a.**). The line cuts in the time domain are numerically fitted to the sum of three sine functions (solid lines in **e.**) with different amplitudes. Three separate peaks are visible in the frequency domain **(f.)** when the ΔB_Z is largely polarized in the bottom panel (blue line) in **f.** Simulated LZS oscillation in **c.** the time domain and **d.** the frequency

domain with the ΔB_Z in the inset of **(d.)**. The simulation in the frequency domain reproduces the branches shown in **(b.)**.

Furthermore, the WM's coherent LZS dynamics provide a novel approach to measure the spatial Overhauser field gradient ΔB_Z between QDs. When ΔB_Z is larger than the exchange splitting between $D_T(1,2;1/2)$ ($D_T(1,2;-1/2)$) and $Q(1,2;1/2)$ ($Q(1,2;-1/2)$), the eigenstates are expected to become $D_{T1}(1,2;1/2) = |\downarrow\rangle|T+\rangle$ ($D_{T1}(1,2;-1/2) = |\uparrow\rangle|T-\rangle$) and $D_{T0}(1,2;1/2) = |\uparrow\rangle|T_0\rangle$ ($D_{T0}(1,2;-1/2) = |\downarrow\rangle|T_0\rangle$) [46]. Because both states can tunnel-couple to $D_S(1,2;1/2)$ ($D_S(1,2;-1/2)$), the LZS oscillation reveals the $D_{T1} - D_S$ and $D_{T0} - D_S$ energy splittings. As can be inferred from the Hamiltonian (see Supplementary Note 6.5), although the $D_{T0} - D_S$ splitting is independent of the ΔB_Z and B_Z, the $D_{T1} - D_S$ splitting is modulated by ΔB_Z depending on the sign of ΔB_Z and S_Z, providing the direct measure of ΔB_Z. Because the states can initialize to both $D_S(1,2;1/2)$ and $D_S(1,2;-1/2)$ at the EST position, the LZS oscillation captures the dynamics of both $S_Z = 1/2$ and $S_Z = -1/2$ subspaces.

Fig. 6 .4a (4b) illustrates the LZS oscillation measurement of the WM multiplet states at B_0 = 230 mT in the time (frequency) domain with the S-polarization turned on and off at specific laboratory times. The FFT spectrum exhibits three different branches corresponding to the $D_{T0} - D_S$ (red arrow) and $D_{T1} - D_S$ (black and black-dashed arrows) where the beating patterns vary as the S-polarization induces changes in ΔB_z. Two different $D_{T1} - D_S$ branches correspond to different S_Z subspaces, where the sign of ΔB_z should be known to distinguish the S_Z for each branch. The $D_{T0} - D_S$ splitting is the same for both S_Z subspaces and is displayed as a single branch (red arrow). Fig. 6.4c (4d) shows the simulated time (frequency) domain signal of the same LZS oscillation, which agrees well with the experimental result (see Supplementary Note 6.6). As expected, the $D_{T0} - D_S$ splitting is constant regardless of ΔB_z, whereas the $D_{T1} - D_S$ splitting is modulated along the polarization sequence.

The $D_{T0} - D_{T1}$ splitting without the polarization sequence implies the built-in $\Delta B_z \sim 200\ h \cdot \mathrm{MHz} \cdot (g^* \mu_B)^{-1}$ (35 mT), which is also confirmed by the ST_0 oscillation (see Supplementary Note 6.4). ΔB_z increases to 400 $h \cdot \mathrm{MHz} \cdot (g^* \mu_B)^{-1}$ (70 mT) with the S-polarization and decreases to 200 $h \cdot \mathrm{MHz} \cdot (g^* \mu_B)^{-1}$ after turning the polarization off. Thus, we conclude that the S-polarization yields the asymmetric pumping effect ($\Delta B_{nuc} \sim 200\ h \cdot \mathrm{MHz} \cdot (g^* \mu_B)^{-1}$) about the QD sites, whereas the ΔB_{nuc} direction can be experimentally checked, for example, via single-spin electric-dipole spin resonances [42]. Furthermore, the $D_{T0} - D_S$ splitting comprises the decoherence-free subspace for the qubit operations resilient to magnetic noises, where the coherent microwave control combined with the large polarization may enable leakage-free and state-selective transitions.

Discussion

The present work uncovers the spin and energy structure of the WM states and explores the central-spin problem with strongly correlated WM states in semiconductor QDs. With the energy splitting of the WM ~ 0.9 h·GHz, we confirm the programmable DNP of B_{nuc} (ΔB_{nuc}) reaching (but not limited to) 80 mT (35 mT) via leakage spectroscopy and LZS oscillations. The τ_{N} exceeds 60 s, which, together with bidirectional polarizability, is beneficial for stabilizing the nuclear bath fluctuation and realizing long-lived nuclear polarization [10,15].

We anticipate several directions for further developments and applications of WM-enabled DNP. Similar experiments with a larger $\delta L/T_{\mathrm{e}}$ ratio can enable high-fidelity single-shot readout for a faster measurement of the dynamics of nuclear polarization. This would further enable feedback loop control [10] and tracking [12,47] of nuclear environments in multielectron QDs. The real-time Hamiltonian estimation also improves frequency resolution for measuring instantaneous ΔB_{nuc}, which may enable measurements of the degree of spatial localization within WMs. Furthermore, DNP becomes inefficient with increasing E_{ST} of the WM, as discovered herein. This implies that the pulsed-gated electron-nuclear flip-flop probability is a strong function of the Wigner parameter, the microscopic origin of which requires more rigorous investigations.

Methods

Device fabrication

A quadruple QD device was fabricated on a GaAs/AlGaAs heterostructure with a 2DEG formed ~70 nm below the surface. The transport property of the 2DEG showed mobility $\mu = 2.6\times10^{6}$ $cm^2(V\cdot s)^{-1}$ with electron density $n = 4.0\times10^{11}$ cm^{-2} at temperature T = 4 K. Electronic mesa around the QD site was defined by the wet etching technique, and thermal diffusion of a metallic stack of Ni/Ge/Au was used to form the ohmic contacts. The depletion gates were deposited on the surface using standard e-beam lithography and metal evaporation of 5 nm Ti/30 nm Au. The lithographical width of the inner QD along the QD axis direction was designed to be ~10% wider than the outer dot to facilitate WM formation. The QD array was aligned to the [110] crystal axis, as shown in Fig. 6.1a. Although the magnetic field B_0 was intended to be applied perpendicular to the [110] axis to minimize the effect of spin-orbit interaction [2], the angular deviation was not strictly calibrated.

Measurement

The device was placed on a ~ 40 mK plate in a commercial dilution refrigerator (Oxford instruments, Triton-500). Ultra-stable dc-voltages were generated by battery-powered dc-sources (Stanford Research Systems, SIM928). They were then combined with rapid voltage pulses from an arbitrary waveform generator (AWG, Keysight M8195A with a sample rate up to 65 GSa/s) via homemade wideband (10^1–10^{10} Hz) bias tees to be applied to the metallic gate electrodes. An LC-tank circuit with a resonant radio frequency (rf) of ~120 MHz was attached to the ohmic contact near the SET charge sensor to enable high-bandwidth

(f_{BW} > 1 MHz) charge detection [27,30–33]. The reflected rf-signal was first amplified by 50 dB using two-stage low-noise cryo-amplifiers (Caltech Microwave Research, CITLF2 ×2 in series) at a 4 K plate. Next, it was further amplified by 25 dB at room temperature using a homemade low-noise rf-amplifier. The signal was then demodulated by an ultra-high-frequency lock-in amplifier (Zurich Instruments, UHFLI), which was routed to the boxcar integrator built in the UHFLI. Trigger signals with a repetition period of 51 μs were generated by a field-programmable-gate array (FPGA, Digilent, Zedboard) to synchronize the timing of the AWG and the boxcar integrator for the CDS [33].

Eigenstates of three-electron spin states

Three-electron spin-multiplet structure consists of eight different eigenstates, which are four quadruplet states $Q(S_Z = 3/2)$, $Q(S_Z = 1/2)$, $Q(S_Z = -1/2)$, and $Q(S_Z = -3/2)$ and four doublet states $D_S(S_Z = 1/2)$, $D_T(S_Z = 1/2)$, $D_S(S_Z = -1/2)$, and $D_T(S_Z = -1/2)$, as shown in Table 6.1 [46,48,49].

Table 6.1. **Three-electron spin states**

State	Spin structure
$Q(S_Z = 3/2)$	$\lvert\uparrow\uparrow\uparrow\rangle$
$Q(S_Z = 1/2)$	$\frac{1}{\sqrt{3}}(\lvert\uparrow\uparrow\downarrow\rangle+\lvert\uparrow\downarrow\uparrow\rangle+\lvert\downarrow\uparrow\uparrow\rangle)$
$Q(S_Z = -1/2)$	$\frac{1}{\sqrt{3}}(\lvert\downarrow\downarrow\uparrow\rangle+\lvert\downarrow\uparrow\downarrow\rangle+\lvert\uparrow\downarrow\downarrow\rangle)$
$Q(S_Z = -3/2)$	$\lvert\downarrow\downarrow\downarrow\rangle$
$D_S(S_Z = 1/2)$	$\frac{1}{\sqrt{2}}(\lvert\uparrow\uparrow\downarrow\rangle-\lvert\uparrow\downarrow\uparrow\rangle)$
$D_T(S_Z = 1/2)$	$\frac{1}{\sqrt{6}}(\lvert\uparrow\uparrow\downarrow\rangle+\lvert\uparrow\downarrow\uparrow\rangle-2\lvert\downarrow\uparrow\uparrow\rangle)$
$D_S(S_Z = -1/2)$	$\frac{1}{\sqrt{2}}(\lvert\downarrow\downarrow\uparrow\rangle-\lvert\downarrow\uparrow\downarrow\rangle)$
$D_T(S_Z = -1/2)$	$\frac{1}{\sqrt{6}}(\lvert\downarrow\downarrow\uparrow\rangle+\lvert\downarrow\uparrow\downarrow\rangle-2\lvert\uparrow\downarrow\downarrow\rangle)$

When $B_0 = 0$ T, the D_S states, D_T states, and Q states are degenerate respectively, resulting in three different branches in the energy dispersion. We use a simple toy-model Hamiltonian adopted from the double QD hybrid qubit [35,36], which leads to a 6 × 6 Hamiltonian with the charge states considered as below. The ordered basis for the Hamiltonian is [$D_S(2,1)$, $D_T(2,1)$, $Q(2,1)$, $D_S(1,2)$, $D_T(1,2)$, $Q(1,2)$], where n (m) denotes the number of electrons in the left (right) QD by (n, m).

$$H_{\mathrm{elec}} = \begin{bmatrix} \varepsilon/2 & 0 & 0 & t_1 & -t_2 & 0 \\ 0 & \varepsilon/2+\delta\mathrm{L} & 0 & -t_3 & t_4 & 0 \\ 0 & 0 & \varepsilon/2+\delta\mathrm{L} & 0 & 0 & t_4 \\ t_1 & -t_3 & 0 & -\kappa\,\varepsilon/2+\delta\mathrm{R} & 0 & 0 \\ -t_2 & t_4 & 0 & 0 & -\varepsilon/2+\delta\mathrm{R} & 0 \\ 0 & 0 & t_4 & 0 & 0 & -\varepsilon/2+\delta\mathrm{R} \end{bmatrix} - \quad (1)$$

Here, ε is the energy detuning between the double QD, t_i is the tunnel coupling strength between different orbitals (i = 1, 2, 3, 4), and δL (δR) is the orbital energy splitting in the left (right) dot. Further, κ is a factor to account for the different lever-arms of the ground and excited states in the (1,2) WM states [50], recently shown to be the consequence of many-body effects [28,29]. The Hamiltonian is utilized to obtain the energy spectra shown in Fig. 6.1. As we discuss in detail in Supplementary Note 6.6, the LZS oscillation at non-zero B_0 is simulated by adding the hyperfine interaction terms [46,48] to the aforementioned Hamiltonian and by solving the time-dependent Schrodinger equation with the experimentally obtained parameters.

Rate equation

Nuclear spin polarization and the diffusion process were phenomenologically modeled using a rate equation:

$$\frac{\mathrm{d}B_{\mathrm{nuc}}}{\mathrm{d}t} = -B_{\mathrm{nuc}}/\tau_{\mathrm{N}} + b_0 P_{\mathrm{flip}}/T_{\mathrm{rep}}, \qquad (2)$$

where τ_N is the nuclear spin diffusion time, b_0 is the Overhauser field change per electron spin-flip, P_{flip} is the nuclear spin flop probability obtained from the Landau–Zener transition probability P_{LZ} and the false initialization probability (see Supplementary Note 6.3), and T_{rep} is the pulse repetition period. Using Eq. (2), we simulated the polarization–probe sequence shown in Fig. 6.3 with the experimental parameters including the time required for the amplitude sweep in the leakage probe step.

References

[1] E. A. Chekhovich *et al.* Nuclear spin effects in semiconductor quantum dots. *Nature Mater* **12**, 494–504 (2013).

[2] J. M. Nichol *et al.* Quenching of dynamic nuclear polarization by spin–orbit coupling in GaAs quantum dots. *Nat Commun.* **6**, 7682 (2015).

[3] J. R. Petta *et al.* Coherent manipulation of coupled electron spins in semiconductor quantum dots. *Science* **309**, 2180–2184 (2005).

[4] A. C. Johnson *et al.* Triplet–singlet spin relaxation via nuclei in a double quantum dot. *Nature* **435**, 925–928 (2005).

[5] A. I. Tartakovskii *et al.* Nuclear Spin Switch in Semiconductor Quantum Dots. *Phys. Rev. Lett.* **98**, 026806 (2007).

[6] J. H. Ardenkjær-Larsen *et al.* Increase in signal-to-noise ratio of > 10,000 times in liquid-state NMR. *Proc. Natl. Acad. Sci.* **100**, 10158–10163 (2003).

[7] S. Simmons *et al.* Entanglement in a solid-state spin ensemble. *Nature* **470**, 69–72 (2011).

[8] J. R. Petta *et al.* Dynamic nuclear polarization with single electron spins. *Phys. Rev. Lett.* **100**, 067601 (2008).

[9] D. J. Reilly *et al.* Suppressing Spin Qubit Dephasing by Nuclear State Preparation. *Science* **321**, 817–821 (2008).

[10] H. Bluhm, S. Foletti, D. Mahalu, V. Umansky, and A. Yacoby, Enhancing the coherence of a spin qubit by operating it as a feedback loop that controls its nuclear spin bath. *Phys. Rev. Lett.* **105**, 216803 (2010).

[11] S. Foletti, H. Bluhm, D. Mahalu, V. Umansky, and A. Yacoby, Universal

quantum control of two-electron spin quantum bits using dynamic nuclear polarization. *Nat. Phys.* **5**, 903–908 (2009).

[12] M. D. Shulman *et al.* Suppressing qubit dephasing using real-time Hamiltonian estimation. *Nat. Commun.* **5**, 5156 (2014).

[13] J. Baugh, Y. Kitamura, K. Ono, and S. Tarucha, Large Nuclear Overhauser Fields Detected in Vertically Coupled Double Quantum Dots. *Phys. Rev. Lett.* **99**, 096804 (2007).

[14] K. Ono, and S. Tarucha, Nuclear-Spin-Induced Oscillatory Current in Spin-Blockaded Quantum Dots. *Phys. Rev. Lett.* **92**, 256803 (2004).

[15] J. M. Nichol *et al.* High-fidelity entangling gate for double-quantum-dot spin qubits. *npj Quantum Inf.* **3**, 3 (2017).

[16] M. A. Fogarty *et al.* Integrated silicon qubit platform with single-spin addressability, exchange control and single-shot singlet-triplet readout. *Nat. Commun.* **9**, 4370 (2018).

[17] F. Martins *et al.* Negative spin exchange in a multielectron quantum dot. *Phys. Rev. Lett.* **119**, 227701 (2017).

[18] M. Pioro-Ladrière *et al.* Electrically driven single-electron spin resonance in a slanting Zeeman field. *Nat. Phys.* **4**, 776–779 (2008).

[19] E. A. Laird *et al.* Coherent spin manipulation in an exchange-only qubit. *Phys. Rev. B* **82**, 075403 (2010).

[20] R. Hanson, L. P. Kouwenhoven, J. R. Petta, S. Tarucha, and L. M. K. Vandersypen, Spins in few-electron quantum dots. *Rev. Mod. Phys.* **79**, 1217–1265 (2007).

[21] C. Yannouleas, and U. Landman, Spontaneous Symmetry Breaking in Single

and Molecular Quantum Dots. *Phys. Rev. Lett.* **82**, 5325–5328 (1999).

[22] J. C. Abadillo-Uriel, B. Martinez, M. Filippone, and Y.-M. Niquet, Two-body Wigner molecularization in asymmetric quantum dot spin qubits. *Phys. Rev. B* **104**, 195305 (2021).

[23] H. E. Ercan, S. N. Coppersmith, and M. Friesen, Strong electron-electron interactions in Si/SiGe quantum dots. *Phys. Rev. B* **104**, 235302 (2021).

[24] I. Shapir *et al.* Imaging the electronic Wigner crystal in one dimension. *Science* **364**, 870–875 (2019).

[25] J. Corrigan *et al.* Coherent Control and Spectroscopy of a Semiconductor Quantum Dot Wigner Molecule. *Phys. Rev. Lett.* **127**, 127701 (2021).

[26] S. Pecker *et al.* Observation and spectroscopy of a two-electron Wigner molecule in an ultraclean carbon nanotube. *Nature Phys* **9**, 576–581 (2013).

[27] W. Jang, *et al.* Single-Shot Readout of a Driven Hybrid Qubit in a GaAs Double Quantum Dot. *Nano Lett.* **21**, 4999–5005 (2021).

[28] C. Yannouleas, and U. Landman, Molecular formations and spectra due to electron correlations in three-electron hybrid double-well qubits. *Phys. Rev. B* **105**, 205302 (2022).

[29] C. Yannouleas, and U. Landman, Wigner molecules and hybrid qubits. *J. Phys.: Condens. Matter* **34**, 21LT01 (2022).

[30] D. J. Reilly, C. M. Marcus, M. P. Hanson, and A. C. Gossard, Fast single-charge sensing with a rf quantum point contact. *Appl. Phys. Lett.* **91**, 162101 (2007).

[31] C. Barthel *et al.* Fast sensing of double-dot charge arrangement and spin state with a radio-frequency sensor quantum dot. *Phys. Rev. B* **81**, 161308 (2010).

[32] A. Noiri *et al.* Radio-Frequency-Detected Fast Charge Sensing in Undoped

Silicon Quantum Dots. *Nano Lett.* **20**, 947–952 (2020).

[33] W. Jang *et al.* Robust energy-selective tunneling readout of singlet-triplet qubits under large magnetic field gradient. *npj Quantum Inf.* **6**, 64 (2020).

[34] T. Meunier *et al.* High fidelity measurement of singlet–triplet state in a quantum dot. *Phys. status solidi B* **243**, 3855–3858 (2006).

[35] Z. Shi *et al.* Fast coherent manipulation of three-electron states in a double quantum dot. *Nat. Commun.* **5**, 3020 (2014).

[36] D. Kim *et al.* Quantum control and process tomography of a semiconductor quantum dot hybrid qubit. *Nature* **511**, 70–74 (2014).

[37] K. D. Petersson, J. R. Petta, H. Lu, and A. C. Gossard, Quantum coherence in a one-electron semiconductor charge qubit. *Phys. Rev. Lett.* **105**, 246804 (2010).

[38] D. Kim *et al.* High-fidelity resonant gating of a silicon-based quantum dot hybrid qubit. *npj Quantum Inf.* **1**, 15004 (2015).

[39] D. Jirovec, *et al.* A singlet-triplet hole spin qubit in planar Ge. *Nat. Mater.* **20**, 1106–1112 (2021).

[40] F. K. Malinowski *et al.* Spin of a Multielectron Quantum Dot and Its Interaction with a Neighboring Electron. *Phys. Rev. X* **8**, 011045 (2018).

[41] R. Hanson *et al.* Zeeman Energy and Spin Relaxation in a One-Electron Quantum Dot. *Phys. Rev. Lett.* **91**, 196802 (2003).

[42] F. H. L. Koppens *et al.* Driven coherent oscillations of a single electron spin in a quantum dot. *Nature* **442**, 766–771 (2006).

[43] J. R. Petta, H. Lu, and A. C. Gossard, A Coherent Beam Splitter for Electronic Spin States. *Science* **327**, 669–672 (2010).

[44] C. Deng and X. Hu, Nuclear spin diffusion in quantum dots: Effects of

inhomogeneous hyperfine interaction. *Phys. Rev. B* **72**, 165333 (2005).

[45] D. J. Reilly *et al.* Exchange Control of Nuclear Spin Diffusion in a Double Quantum Dot. *Phys. Rev. Lett.* **104**, 236802 (2010).

[46] B.-B. Chen *et al.* Spin blockade and coherent dynamics of high-spin states in a three-electron double quantum dot. *Phys. Rev. B* **95**, 035408 (2017).

[47] T. Nakajima *et al.* Coherence of a Driven Electron Spin Qubit Actively Decoupled from Quasistatic Noise. *Phys. Rev. X* **10**, 011060 (2020).

[48] J.-T. Hung, J. Fei, M. Friesen, and X. Hu, Decoherence of an exchange qubit by hyperfine interaction. *Phys. Rev. B* **90**, 045308 (2014).

[49] Z. Shi *et al.* Fast Hybrid Silicon Double-Quantum-Dot Qubit. *Phys. Rev. Lett.* **108**, 140503 (2012).

[50] G. Cao *et al.* Tunable Hybrid Qubit in a GaAs Double Quantum Dot. *Phys. Rev. Lett.* **116**, 086801 (2016).

Extended Data

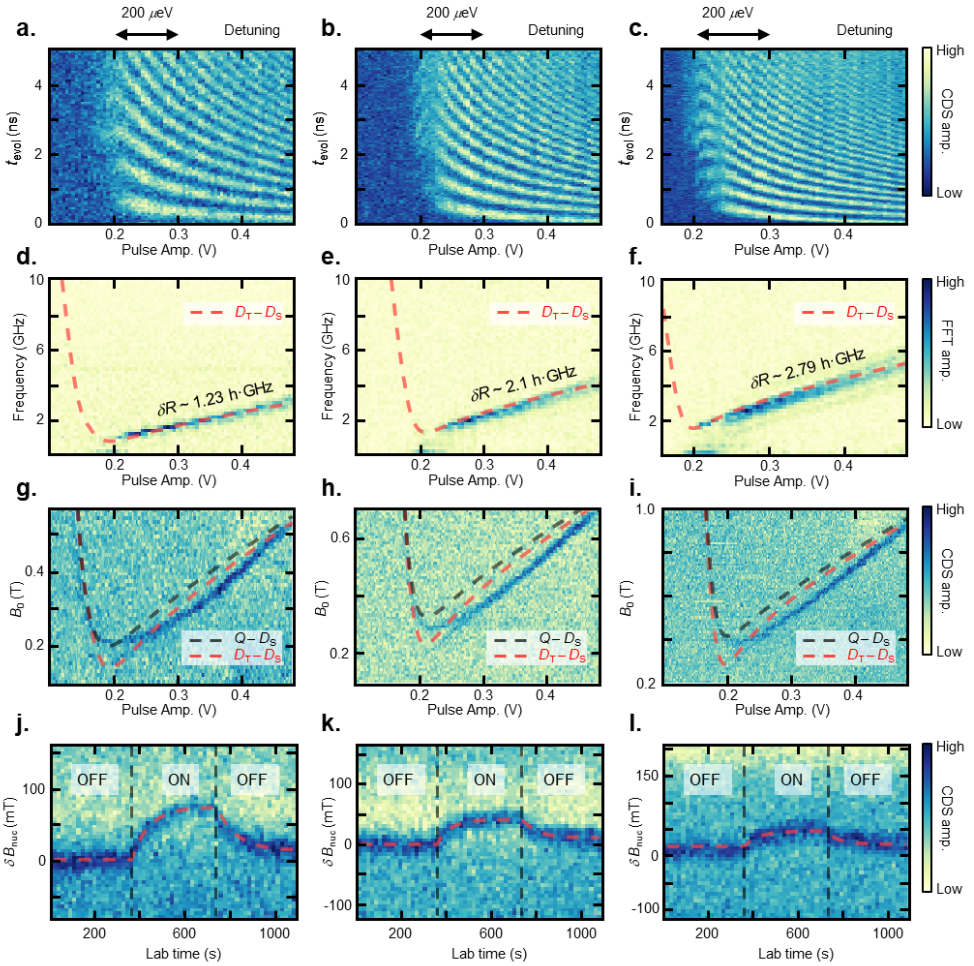

Extended Data Fig. 6.1. Dynamic nuclear polarization under different tunings of Wigner molecule energy spectrum. Time (frequency) domain Landau–Zener–Stuckelberg oscillation with the singlet-triplet splitting of the Wigner molecule (WM), δR of **a.** (**d.**) ~ 1.23 $h\cdot$GHz, **b.** (**e.**) 2.1 $h\cdot$GHz, and **c.** (**f.**) 2.79 $h\cdot$GHz. Red-dashed curves in the frequency domain signals (**d.**, **e.**, and **f.**) show the energy splitting between D_T and D_S states derived from the toy-model Hamiltonian (see Methods section), from which we extract the magnitude of δR.

The δR is tuned with the dc-gate-voltages. Leakage spectroscopy of the WM with δR of **g.** ~ 1.23 $h\cdot$GHz, **h.** 2.1 $h\cdot$GHz, and **i.** 2.79 $h\cdot$GHz. Red (black) dashed curves are the $D_T - D_S$ ($Q - D_S$) energy spacings calculated from the toy-model Hamiltonian with the Lande g-factor $g^* \sim -0.4$. δB_{nuc} measurement with the S-polarization turned on and off with δR of **j.** ~ 1.23 $h\cdot$GHz, **k.** 2.1 $h\cdot$GHz, and **l.** 2.79 $h\cdot$GHz. Although the nuclear spin diffusion time is $\tau_N \sim 60$ s for all tuning, the nuclear polarization strength per electron spin flip b_0 decreases with increasing δR, as shown in Fig. 6.3d in the main text, resulting in smaller B_{max} for larger δR (i.e., smaller Wigner parameter)

Supplementary Note 6.1. Electron temperature

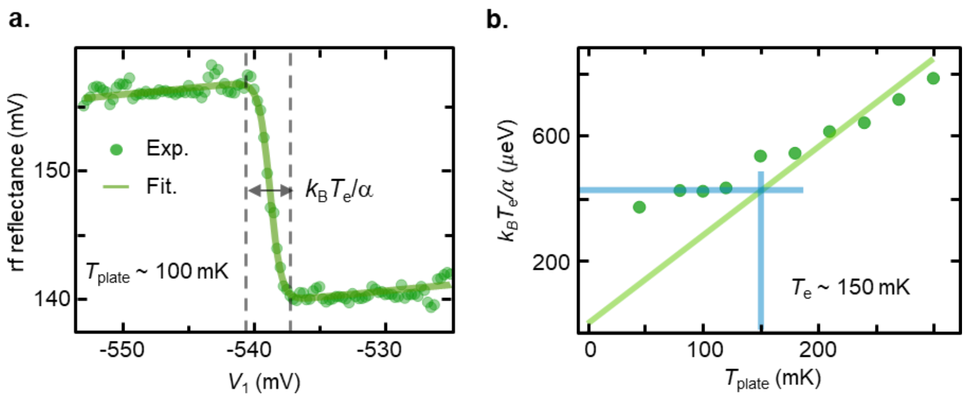

Supplementary Figure S6.3. Electron temperature measurement. a. Charge transition line broadening due to the finite electron temperature. The radio-frequency (rf)-single-electron transistor (rf-SET) charge sensing signal is recorded as a function of the gate voltage V_1 near the (2,1)–(1,1) charge transition at the mixing chamber plate temperature of the dilution refrigerator T_{plate} ~ 100 mK. The solid curve is a fit to the Fermi–Dirac distribution with a linear background slope, from which we obtain the thermal broadening $k_B T_e/\alpha$, where k_B is the Boltzmann constant, T_e is the electron temperature, and α is the lever arm of V_1. **b.** $k_B T_e/\alpha$ measured with varying T_{plate}. From the linear relationship for $T_{plate} > 200$ mK and plateau for $T_{mixing} < 100$ mK, we estimate T_e = 150 mK and α = 0.03, respectively.

Supplementary Note 6.2. Correlated double sampling (CDS)

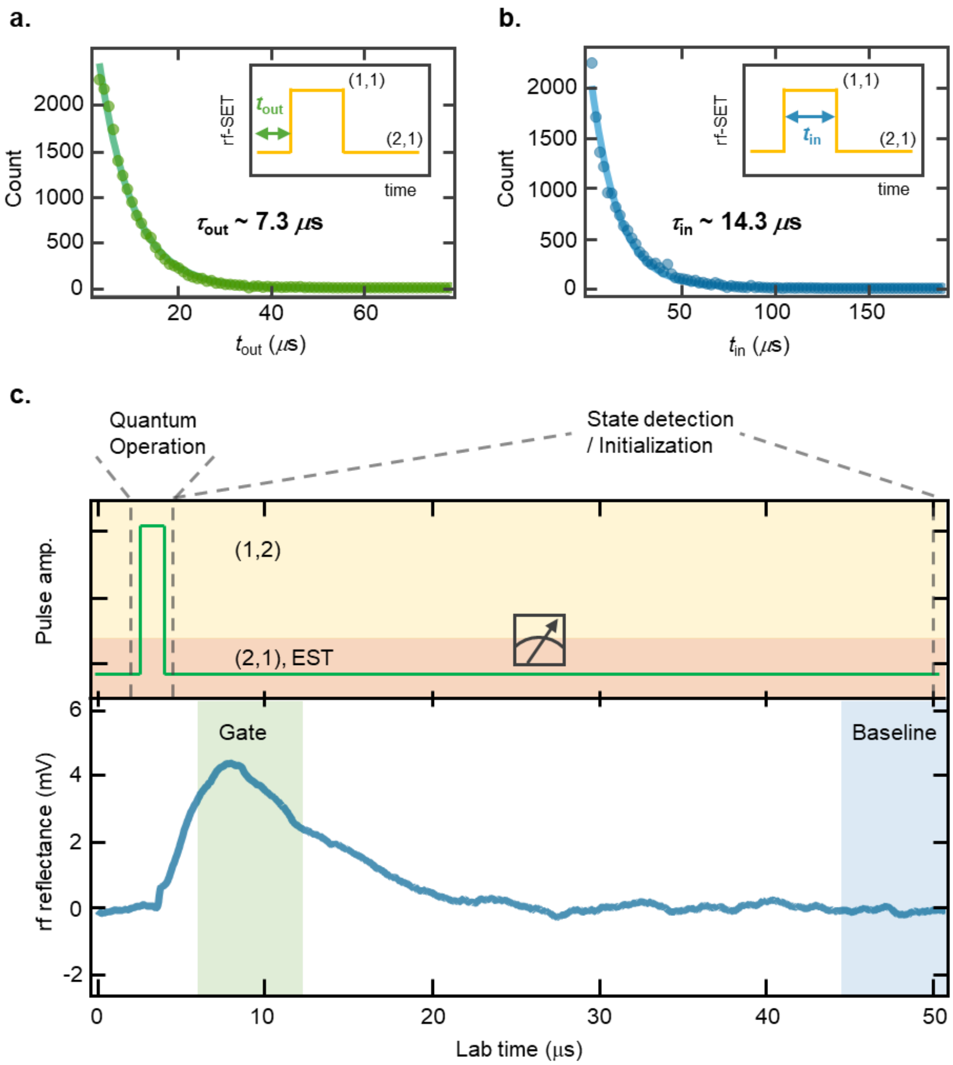

Supplementary Figure S6.4. Tunneling time scale and correlated double sampling (CDS). a. (b.) Tunneling-out (-in) statistics. The solid curve is a fit to an exponential decay yielding the tunneling-out (-in) time τ_{out} (τ_{in}) ~ 7 (14) μs. Inset in each figure shows a schematic of the charge sensor signal showing tunneling events in the (2,1) energy-selective tunneling (EST) region [1–4] recorded with the radio-frequency (rf)-single-electron transistor (rf-SET). **c.** Top panel: schematic of the quantum control sequence. The pulse brings the initialized state from (2,1) to the operation point in (1,2) and drives back to (2,1) for the EST readout and state initialization. Bottom panel: periodically averaged (~10^6 lines) ac-coupled rf-SET signal synchronized with the Landau–Zener–Stückelberg (LZS)-induced X_π pulse. The dc-offset-eliminated CDS amplitude is generated by subtracting the baseline signal (blue shaded box) from the gate signal (green shaded box) and averaging ~10^3 times via the boxcar integrator. As discussed in the main text, the boxcar integration and the control waveform generation is synchronized to a trigger signal with period of 51 μs.

Supplementary Note 6.3. Numerical simulation of the nuclear polarization sequence

The nuclear field B_{nuc} during the dynamic nuclear polarization (DNP) is numerically reproduced using the rate equation as follows:

$$\frac{\mathrm{d}B_{\mathrm{nuc}}}{\mathrm{d}t} = -B_{\mathrm{nuc}}\Big/\tau_{\mathrm{N}} + b_0 P_{\mathrm{flip}}\Big/T_{\mathrm{rep}} . \qquad \text{(SE1)}$$

As discussed in the Methods section, τ_{N} is the nuclear spin diffusion time, T_{rep} is the repetition period of the polarization pulse, b_0 is the change in the nuclear field per electron spin flip, and P_{flip} is the spin-flip probability obtained from the Landau–Zener transition probability P_{LZ} and the false initialization probabilities β.

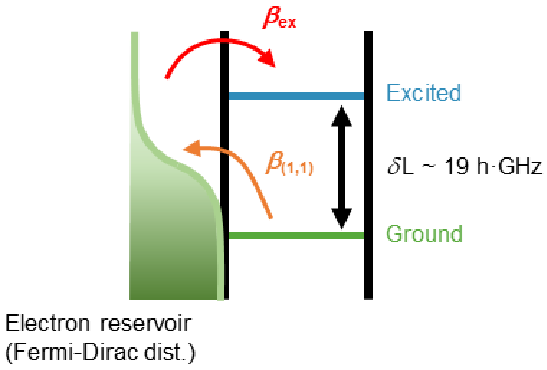

Supplementary Figure S6.5. Schematic of false initialization at energy-selective tunneling. False initialization to the (1,1) ($\beta_{(1,1)}$, orange arrow) or the excited orbitals (β_{ex}, red arrow) may occur owing to thermal tunneling.

We first analyze the spin-flip probability P_{flip} per adiabatic passage. Because of the small singlet-triplet splitting in the (2,1) EST region $\delta L \sim 19\ h\cdot$GHz, where h is Planck's constant, the false initialization probability to (1,1) at the start of the pulse is $\beta_{(1,1)} \sim 0.37$ (Fig. S6.3, orange arrow), which does not contribute to the polarization. We also estimate the probability of the false initialization to the excited orbitals β_{ex} from the Fermi–Dirac distribution with $T_e \sim 150$ mK, as described in Supplementary Note 6.1. With the Fermi level of the reservoir straddling in the middle of the $D_T - D_S$ splitting, we find $(\beta_{ex})^{-1} \sim Z = 1 + \exp(\delta L/2)/k_B T_e) = (0.049)^{-1}$, where Z is the partition function [5]. Because the falsely initialized state in the excited orbital contributes to the polarization in the opposite direction, we calculate $P_{flip} = P_{LZ}\cdot(1 - \beta_{(1,1)} - 2\beta_{ex})$. We estimate $P_{LZ} \sim 0.5$ for the given adiabatic ramp width w_R from Fig. 6.3, as the maximum efficiency is saturated for $w_R > 0.8\ \mu s$. The resultant P_{flip} is 0.26.

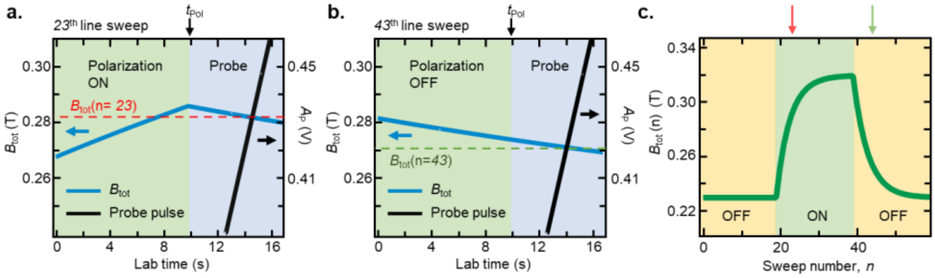

Supplementary Figure S6.6. a. Schematic of the net magnetic field $B_{tot} = B_0 + B_{nuc}$ during the polarization and the probe stages. During the polarization stage (green shaded area), B_{nuc} builds up and then decays at the probe stage (blue shaded area) owing to nuclear diffusion. The decaying B_{tot} is probed by the pulse amplitude sweep denoted by the black solid line. The crossing of B_{tot} and the pulse amplitude is recorded as the leakage point (red-dotted line in **a.**, red arrow in **c.**). **b.** B_{tot} with the polarization turned off. The crossing point (green-dotted line) is recorded as B_{tot} (n = 43) shown in **c.** (green arrow). **c.** Simulation of B_{tot} during the S-polarization sequence. When the polarization is turned on, B_{tot} builds in the direction of the B_0 and then decays back when the polarization is turned off.

To simulate the polarization sequence, we consider the duration of the polarization stage $t_{Pol} \sim 10$ s and the adiabatic ramp amplitude A_R by setting the P_{flip} to 0.26 only if the laboratory time $t_{lab} < t_{Pol}$ and $B_{tot} = B_0 + B_{nuc} < B_L(A_R)$; otherwise, we set $P_{flip} = 0$. Here, B_L is the one-to-one function between the pulse amplitude and the magnetic field strength obtained from the leakage spectrum in Fig. 6.2b. This reproduces the experimental situation where the polarization pulse is turned on for t_{Pol} only when the anti-crossing is reachable with the maximum pulse amplitude, as shown in the green-shaded area in Fig. S6.4a. We convert the number of polarized nuclei to B_{nuc} via b_0.

Based on the above-mentioned setting, we numerically mimic the leakage measurement shown in Fig. 6.3e. We check for the point where the crossing of the decaying B_{tot} and the probe pulse amplitude (black line in Fig. S6.4a, S6.4b) occurs at the probe stage (Fig. S6.4a, (S6.4b), red (green) dashed line) and denote it as $B_{\mathrm{tot}}(n)$ for the n^{th} leakage measurement line sweep. Fig. S6.4c shows a collection of crossing points $B_{\mathrm{tot}}(n)$ with the polarization turned on and off along n, which reflects the leakage measurement with the polarization sequence turned on and off, respectively. We fit $B_{\mathrm{tot}}(n)$ to the leakage measurement in Fig. 6.3e and obtain $b_0 \sim 2.58$ $h\cdot\mathrm{kHz}\cdot(g^*\mu_{\mathrm{B}})^{-1}$ and $\tau_{\mathrm{N}} \sim 62$ s.

Supplementary Note 6.4. Inefficient nuclear polarization in the two-electron singlet-triplet qubit regime

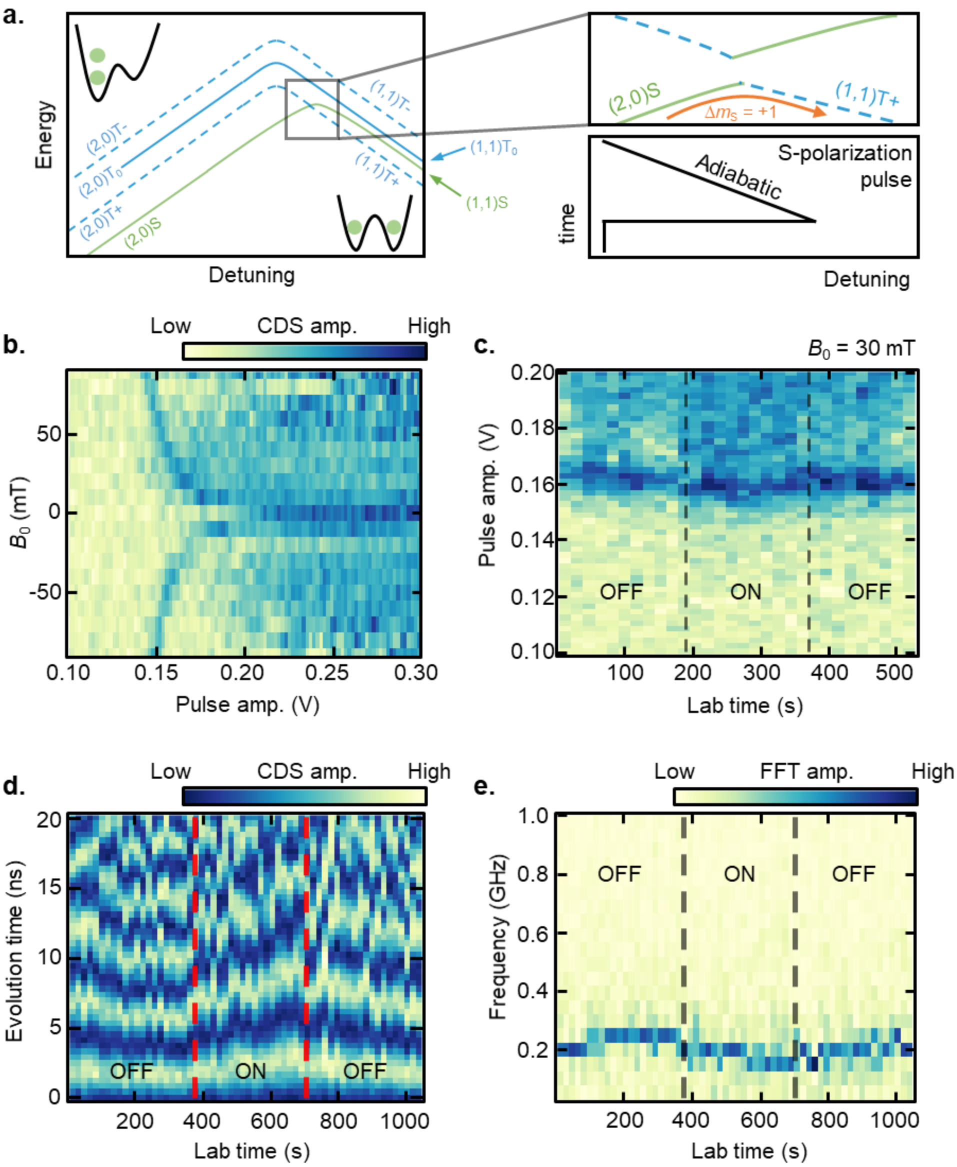

Supplementary Figure S6.7. a. Left panel: schematic of the singlet-triplet (ST_0) qubit energy levels in the two-electron regime. Zeeman-split T+ level crosses with the singlet branch (black rectangle) resulting in the Overhauser field-mediated anti-crossing. Right panel: magnified view of the anti-crossing with the pulse sequence shown below for the S-polarization ($\Delta m_S = +1$, $\Delta m_N = -1$) with the ST_0 qubit [6,7]. **b.** Leakage spectroscopy (spin-funnel) of the singlet-triplet (ST_0) qubit. The spectrum reveals the S–T+ anti-crossing points as a function of B_0. **c.** Leakage measurement at B_0 = 30 mT with the S-polarization turned on and off with a pulse repetition period of 51 μs. No significant signature of B_{nuc} exceeding the fluctuation was found. **d. (e.)** Time (frequency) domain signal of the ST_0 qubit Larmor oscillation at B_0 = 230 mT with the S-polarization turned on and off. A built-in $|\Delta B_Z| = |B_Z^L - B_Z^R| \sim 200\ h\cdot\mathrm{MHz}\cdot(g^*\mu_B)^{-1}$ exists, where the additional polarization effect is not significantly larger than the fluctuation.

In this section, we show the two-electron singlet-triplet (ST_0) spin qubit operation to compare the nuclear polarization effect in the same device. Fig. S6.5a shows typical two-electron energy levels in a double quantum dot (QD) [8]. The Zeeman-split T+ level crosses with the singlet branch, and the crossing becomes an anti-crossing aided by the finite transverse nuclear Overhauser field [6,7] (right panel in Fig. S6.5a).

Utilizing the EST readout in the (2,0) charge configuration [3], we first measure the leakage spectrum of the ST_0 qubit by probing the S–T+ anti-crossings as a function of B_0 (Fig. S6.5b). Because the leakage position is sensitive to the magnetic field only for $|B_0| < 50$ mT, we set B_0 = 30 mT and investigate the effect of S-polarization in Fig. S6.5c. We use the same $T_{rep} \sim 51$ μs as described in the main text and measure the anti-crossing position with the polarization pulse turned on and off with the same polarization-probe sequence shown in Fig. 6.3e. As a result, we find that the polarization effect is found to not be as significant as in the Wigner molecule (WM) case shown in Fig. 6.3. This is consistent with a previous report [6], where a sizable B_{nuc} is only observable for T_{rep} < 30 μs using ST_0 qubit.

The Larmor oscillation frequency of the ST_0 qubit corresponds to the size of the spatial magnetic field gradient ΔB_Z between the double QD (DQD) [8,9]. We also measure the ST_0 Larmor oscillation with the S-polarization turned on and off at B_0 = 230 mT, as shown in Fig. S6.5d, with the same sequence as in Fig. 6.4. We first note that there exists a built-in $\Delta B_Z \sim 200\ h\cdot\mathrm{MHz}\cdot(g^*\mu_B)^{-1}$ stemming from the nuclear Overhauser field, consistent with the energy splitting between the D_{T1} and D_{T0} energy levels without the polarization, as shown in Fig. 6.4b and 6.4d. In contrast to the WM case shown in the main text where the S-polarization yields a change of $|\Delta B_Z| = |B_L^Z - B_R^Z| \sim 200\ h\cdot\mathrm{MHz}\cdot(g^*\mu_B)^{-1}$, the S-polarization with the ST_0 qubit does not induce a polarization that is significantly larger than the nuclear field fluctuation with the same $T_{rep} \sim 51$ μs [6]. This indicates that a large Knight field shift aided by the non-uniform broadening of the WM wavefunction may suppress the nuclear spin diffusion and lead to sizable nuclear polarization despite the slow pulse repetition rate [10,11].

Supplementary Note 6.5. Magnetic Hamiltonian

We adopt the hyperfine Hamiltonian from the exchange-only qubit defined in a triple QD [12] as follows. The ordered basis for the Hamiltonian is [$D_S(1/2)$, $D_T(1/2)$, $Q(1/2)$, $Q(3/2)$, $D_S(-1/2)$, $D_T(-1/2)$, $Q(-1/2)$, $Q(-3/2)$].

$$H_{\mathrm{hf}} = \left[\begin{array}{cccc|cccc}
\frac{1}{2}B^{Z}_{100} & -\frac{1}{2\sqrt{3}}B^{Z}_{01\bar{1}} & -\frac{1}{\sqrt{6}}B^{Z}_{01\bar{1}} & \frac{1}{2\sqrt{2}}B^{+}_{01\bar{1}} & -\frac{1}{2}B^{-}_{100} & \frac{1}{2\sqrt{3}}B^{+}_{01\bar{1}} & -\frac{1}{2\sqrt{6}}B^{-}_{01\bar{1}} & 0 \\
-\frac{1}{2\sqrt{3}}B^{Z}_{01\bar{1}} & \frac{1}{6}B^{Z}_{\bar{1}22} & -\frac{1}{3\sqrt{2}}B^{Z}_{\bar{2}11} & \frac{1}{2\sqrt{6}}B^{+}_{\bar{2}11} & \frac{1}{2\sqrt{3}}B^{-}_{01\bar{1}} & \frac{1}{6}B^{-}_{\bar{1}22} & -\frac{1}{2\sqrt{6}}B^{-}_{\bar{2}11} & 0 \\
-\frac{1}{\sqrt{6}}B^{Z}_{01\bar{1}} & -\frac{1}{3\sqrt{2}}B^{Z}_{\bar{2}11} & \frac{1}{6}B^{Z}_{111} & \frac{1}{2\sqrt{3}}B^{+}_{111} & -\frac{1}{2\sqrt{6}}B^{+}_{01\bar{1}} & -\frac{1}{2\sqrt{6}}B^{+}_{\bar{2}11} & \frac{1}{3}B^{-}_{111} & 0 \\
\frac{1}{2\sqrt{2}}B^{-}_{01\bar{1}} & \frac{1}{2\sqrt{6}}B^{-}_{\bar{2}11} & \frac{1}{2\sqrt{3}}B^{-}_{111} & \frac{1}{2}B^{Z}_{111} & 0 & 0 & 0 & 0 \\
\hline
-\frac{1}{2}B^{+}_{100} & \frac{1}{2\sqrt{3}}B^{+}_{01\bar{1}} & -\frac{1}{2\sqrt{6}}B^{-}_{01\bar{1}} & 0 & -\frac{1}{2}B^{Z}_{100} & \frac{1}{2\sqrt{3}}B^{Z}_{01\bar{1}} & \frac{1}{\sqrt{6}}B^{Z}_{01\bar{1}} & \frac{1}{2\sqrt{2}}B^{-}_{01\bar{1}} \\
\frac{1}{2\sqrt{3}}B^{-}_{01\bar{1}} & \frac{1}{6}B^{+}_{\bar{1}22} & -\frac{1}{2\sqrt{6}}B^{-}_{\bar{2}11} & 0 & \frac{1}{2\sqrt{3}}B^{Z}_{01\bar{1}} & -\frac{1}{6}B^{Z}_{\bar{1}22} & \frac{1}{3\sqrt{2}}B^{Z}_{\bar{2}11} & \frac{1}{2\sqrt{6}}B^{-}_{\bar{2}11} \\
-\frac{1}{2\sqrt{6}}B^{+}_{01\bar{1}} & -\frac{1}{2\sqrt{6}}B^{+}_{\bar{2}11} & \frac{1}{3}B^{+}_{111} & 0 & \frac{1}{\sqrt{6}}B^{Z}_{01\bar{1}} & \frac{1}{3\sqrt{2}}B^{Z}_{\bar{2}11} & -\frac{1}{6}B^{Z}_{111} & \frac{1}{2\sqrt{3}}B^{-}_{111} \\
0 & 0 & 0 & 0 & \frac{1}{2\sqrt{2}}B^{+}_{01\bar{1}} & \frac{1}{2\sqrt{6}}B^{+}_{\bar{2}11} & \frac{1}{2\sqrt{3}}B^{+}_{111} & -\frac{1}{2}B^{Z}_{111}
\end{array}\right]$$

(SE2)

Here, $B^{r}_{abc} = aB^{r}_{1} + bB^{r}_{2} + cB^{r}_{3}$, where r = z, +, –, B_d denotes the magnetic field on the d^{th} electron, and $\bar{n} = -n$. The transverse magnetic field B^+ and B^- couple different S_Z subspaces with $|\Delta m_S| = 1$, where S_Z is the spin projection to the quantization axis. Note that the spin-flip terms corresponding to $|\Delta m_S| = 2$ are not present.

For the LZS oscillation simulation shown in Fig. 6.4c, 6.4d, we assume that 1) the transverse Overhauser field B^+ and B^- are negligibly small compared to B^Z, and 2) the spatial magnetic field gradient within a single QD is insignificant compared to that between the left and right QDs. In the (1,2) charge configuration in a DQD, we use $B_L = B_{d=1}$ to denote the magnetic field on the electron in the left QD and $B_R = B_{d=2} = B_{d=3}$ to denote the magnetic field experienced by the two electrons inside the right QD. Based on the notation and the two assumptions above, H_{hf} can be simplified as (SE3).

$$H_{\mathrm{hf}} = \left[\begin{array}{cccc|cccc}
\frac{1}{2}B_{\mathrm{L}}^{\mathrm{Z}} & 0 & 0 & 0 & 0 & 0 & 0 & 0 \\
0 & \frac{1}{6}(4B_{\mathrm{R}}^{\mathrm{Z}} - B_{\mathrm{L}}^{\mathrm{Z}}) & \frac{2}{3\sqrt{2}}\Delta B_{\mathrm{Z}} & 0 & 0 & 0 & 0 & 0 \\
0 & \frac{2}{3\sqrt{2}}\Delta B_{\mathrm{Z}} & \frac{1}{6}(B_{\mathrm{L}}^{\mathrm{Z}} + 2B_{\mathrm{R}}^{\mathrm{Z}}) & 0 & 0 & 0 & 0 & 0 \\
0 & 0 & 0 & \frac{1}{2}(B_{\mathrm{L}}^{\mathrm{Z}} + 2B_{\mathrm{R}}^{\mathrm{Z}}) & 0 & 0 & 0 & 0 \\
\hline
0 & 0 & 0 & 0 & -\frac{1}{2}B_{\mathrm{L}}^{\mathrm{Z}} & 0 & 0 & 0 \\
0 & 0 & 0 & 0 & 0 & -\frac{1}{6}(4B_{\mathrm{R}}^{\mathrm{Z}} - B_{\mathrm{L}}^{\mathrm{Z}}) & -\frac{2}{3\sqrt{2}}\Delta B_{\mathrm{Z}} & 0 \\
0 & 0 & 0 & 0 & 0 & -\frac{2}{3\sqrt{2}}\Delta B_{\mathrm{Z}} & -\frac{1}{6}(B_{\mathrm{L}}^{\mathrm{Z}} + 2B_{\mathrm{R}}^{\mathrm{Z}}) & 0 \\
0 & 0 & 0 & 0 & 0 & 0 & 0 & -\frac{1}{2}(B_{\mathrm{L}}^{\mathrm{Z}} + 2B_{\mathrm{R}}^{\mathrm{Z}})
\end{array}\right]$$

$$= \left[\begin{array}{c|c} H_{\mathrm{hf,P}} & 0 \\ \hline 0 & H_{\mathrm{hf,N}} \end{array}\right]$$

(SE3)

$H_{\mathrm{hf,P}}$ ($H_{\mathrm{hf,N}}$) is the Hamiltonian in the positive (negative) spin subspace, where $H_{\mathrm{hf,N}} = -H_{\mathrm{hf,P}}$ holds. Diagonalizing $H_{\mathrm{hf,P}}$ results in Eq. (SE4) as shown below with the ordered basis [D_{S}(1,2; 1/2), D_{T0}(1,2; 1/2), D_{T1}(1,2; 1/2), Q(1,2; 3/2)] [13]. Here, D_{T0}(1,2; 1/2) = $|\uparrow\rangle|T_0\rangle$ and D_{T1}(1,2; 1/2) = $|\downarrow\rangle|T_+\rangle$, as mentioned in the main text. Further, n (m) denotes the electron number inside the left (right) QD by (n, m; S_z).

$$H_{\mathrm{hf,P}} = \begin{bmatrix} \frac{1}{2}B_{\mathrm{L}}^{\mathrm{Z}} & 0 & 0 & 0 \\ 0 & \frac{1}{2}B_{\mathrm{L}}^{\mathrm{Z}} & 0 & 0 \\ 0 & 0 & \frac{1}{2}B_{\mathrm{L}}^{\mathrm{Z}} - \Delta B_{\mathrm{Z}} & 0 \\ 0 & 0 & 0 & \frac{1}{2}(B_{\mathrm{L}}^{\mathrm{Z}} + 2B_{\mathrm{R}}^{\mathrm{Z}}) \end{bmatrix} \quad \text{(SE4)}$$

$D_{\mathrm{T1}} - D_{\mathrm{T0}}$ splitting is governed by ΔB_{Z}, providing a direct measure of the size of the spatial magnetic field gradient, ΔB_{Z}. We emphasize that $D_{\mathrm{T0}} - D_{\mathrm{S}}$ splitting is now independent of the magnetic field strength, providing a decoherence-free subspace for high-fidelity qubit operations. However, we note that $D_{\mathrm{T0}} - D_{\mathrm{S}}$ splitting may still be disturbed by the magnetic field gradient noise within the right QD, which we assume to be negligible compared to ΔB_{Z}. After implementing the single-shot readout-based real-time Hamiltonian estimation technique [14], we anticipate that the investigation of the temporal dynamics of $D_{\mathrm{T0}} - D_{\mathrm{S}}$ splitting may enable the study of the magnetic field behavior within a single QD. This in turn would be helpful to reveal the spatial distribution of the WM wavefunction.

Supplementary Note 6.6. Simulation of the Landau–Zener–Stückelberg oscillation

As discussed in Supplementary Note 6.5, we neglect the transverse magnetic field contribution and do not consider the transition between different S_{Z} subspaces in the LZS oscillation simulation. This allows us to analyze the dynamics of the $S_{\mathrm{Z}} = 1/2$ and $S_{\mathrm{Z}} = -1/2$ subspaces separately and ignore the $|S_{\mathrm{Z}}| = 3/2$ subspace. We combine the reduced $S_{\mathrm{Z}} = 1/2$ ($S_{\mathrm{Z}} = -1/2$) hyperfine Hamiltonian with the electronic Hamiltonian shown in the Methods section to describe the dynamics in the $S_Z = 1/2$ ($S_Z = -1/2$) subspace. The hyperfine Hamiltonian in the $S_Z = 1/2$ subspace with the charge configurations is explicitly considered as follows. The ordered basis for the Hamiltonian is [$D_S(2,1;\ 1/2)$, $D_T(2,1;\ 1/2)$, $Q(2,1;\ 1/2)$, $D_S(1,2;\ 1/2)$, $D_T(1,2;\ 1/2)$, $Q(1,2;\ 1/2)$].

$$H_{\mathrm{hf},1/2} = \left[\begin{array}{ccc|ccc} \frac{1}{2}B_\mathrm{R}^\mathrm{Z} & 0 & 0 & 0 & 0 & 0 \\ 0 & \frac{1}{6}(4B_\mathrm{L}^\mathrm{Z} - B_\mathrm{R}^\mathrm{Z}) & -\frac{2}{3\sqrt{2}}\Delta B_\mathrm{Z} & 0 & 0 & 0 \\ 0 & -\frac{2}{3\sqrt{2}}\Delta B_\mathrm{Z} & \frac{1}{6}(B_\mathrm{R}^\mathrm{Z} + 2B_\mathrm{L}^\mathrm{Z}) & 0 & 0 & 0 \\ \hline 0 & 0 & 0 & \frac{1}{2}B_\mathrm{L}^\mathrm{Z} & 0 & 0 \\ 0 & 0 & 0 & 0 & \frac{1}{6}(4B_\mathrm{R}^\mathrm{Z} - B_\mathrm{L}^\mathrm{Z}) & \frac{2}{3\sqrt{2}}\Delta B_\mathrm{Z} \\ 0 & 0 & 0 & 0 & \frac{2}{3\sqrt{2}}\Delta B_\mathrm{Z} & \frac{1}{6}(B_\mathrm{L}^\mathrm{Z} + 2B_\mathrm{R}^\mathrm{Z}) \end{array}\right]$$

(SE 5)

For numerical reproduction of the LZS oscillation shown in Fig. 6.4c, we solve the time-dependent Schrödinger equation by varying the detuning parameter ε according to the pulse shape. As the state probabilistically initializes to either $D_S(2,1;\ 1/2)$ or $D_S(2,1;\ -1/2)$ at EST, we simulate the LZS oscillations of the $S_Z = 1/2$ and the $S_Z = -1/2$ cases separately. The simulated oscillations are then averaged assuming the equal initialization probability to $D_S(2,1;\ 1/2)$ and $D_S(1,2;\ -1/2)$.

Supplementary References

[1] J. M. Elzerman *et al.* Single-shot read-out of an individual electron spin in a quantum dot. *Nature* **430**, 431–435 (2004).

[2] A. Morello *et al.* Single-shot readout of an electron spin in silicon. *Nature* **467**, 687–691 (2010).

[3] W. Jang *et al.* Robust energy-selective tunneling readout of singlet-triplet qubits under large magnetic field gradient. *npj Quantum Inf.* **6**, 64 (2020).

[4] W. Jang *et al.* Single-Shot Readout of a Driven Hybrid Qubit in a GaAs Double Quantum Dot. *Nano Lett.* **21**, 4999–5005 (2021).

[5] J. Z. Blumoff *et al.* Fast and High-Fidelity State Preparation and Measurement in Triple-Quantum-Dot Spin Qubits. *PRX Quantum* **3**, 010352 (2022).

[6] J. R. Petta *et al.* Dynamic nuclear polarization with single electron spins. *Phys. Rev. Lett.* **100**, 067601 (2008).

[7] S. Foletti, H. Bluhm, D. Mahalu, V. Umansky, and A. Yacoby, Universal quantum control of two-electron spin quantum bits using dynamic nuclear polarization. *Nat. Phys.* **5**, 903–908 (2009).

[8] J. R. Petta *et al.* Coherent manipulation of coupled electron spins in semiconductor quantum dots. *Science* **309**, 2180–2184 (2005).

[9] W. Jang, *et al.* Individual two-axis control of three singlet-triplet qubits in a micromagnet integrated quantum dot array. *Appl. Phys. Lett.* **117**, 234001 (2020).

[10] C. Deng, and X. Hu, Nuclear spin diffusion in quantum dots: Effects of inhomogeneous hyperfine interaction. *Phys. Rev. B* **72**, 165333 (2005).

[11] D. J. Reilly *et al.* Exchange Control of Nuclear Spin Diffusion in a Double Quantum Dot. *Phys. Rev. Lett.* **104**, 236802 (2010).

[12] J.-T. Hung, J. Fei, M. Friesen, and X. Hu, Decoherence of an exchange qubit by hyperfine interaction. *Phys. Rev. B* **90**, 045308 (2014).

[13] B.-B. Chen *et al.* Spin blockade and coherent dynamics of high-spin states in a three-electron double quantum dot. *Phys. Rev. B* **95**, 035408 (2017).

[14] M. D. Shulman *et al.* Suppressing qubit dephasing using real-time Hamiltonian estimation. *Nat. Commun.* **5**, 5156 (2014).

Chapter 7. Conclusion

7.1 Summary and conclusion

This thesis presents the coherent control of the multi-electron and nuclear spins in GaAs, based on the single-shot quantum state detection. The EST single-shot detection of the two-electron ST_0 spin qubit allows the robust high-fidelity quantum state detection even when the large magnetic field gradient is present at the DQD site. Recalling that the large magnetic field gradient enables high-fidelity quantum control, and at the same time degrades the readout fidelity for the PSB based state detection schemes, compatibility of the EST with the large gradient is expected to offer a route toward high-fidelity quantum control of multiple ST_0 qubit array.

Such robust, and high-visibility EST readout can further enable efficient real-time Hamiltonian parameter estimation, which can significantly extend the dephasing time of the ST_0 qubit in GaAs. The real-time Hamiltonian estimation based feedback control effectively mitigates the magnetic field fluctuation in GaAs. The work confirms the overall qubit operation fidelity including initialization, control and readout approaching 99 %. Based on the versatility of the method, the technique can be directly applied to Si or Ge to further boost the quantum operation fidelity by mitigating the relatively slow charge noise or the residual nuclear spin noise.

The EST readout can also be utilized for the high-fidelity single-shot detection of the three-electron hybrid qubit. Aided by the quenched energy spectrum of the strongly-correlated Wigner molecule, the three-electron hybrid qubit operation is firstly shown in GaAs, along with the single-shot state detection. The Wigner molecularization offers a route toward coherent qubit operations within the typical experimental bandwidth even in the materials known to exhibit large orbital splitting. Moreover, recalling that the hybrid qubit is directly compatible with the superconducting circuits which can enable long-range qubit interactions [refs], such Wigner molecularization can allow the study of the ultra-strong coupling of the qubit with the superconducting circuits, and further enable long-range entanglement of the semiconductor qubits.

The Wigner molecule can also allow the bidirectional DNP with three-electrons in GaAs within a moderate magnetic field. While the rigorous study on the microscopic origin is needed, the DNP efficiency is shown to increase along the increasing Wigner parameter. Also, the nuclear spin diffusion time is shown to be longer than the typical two-electron cases. Along with the long nuclear spin diffusion time, and the large DNP efficiency sizable nuclear spin field is achieved with relatively slow polarization cycle. This is expected to further allow efficient environmental field control with the EST quantum state detection and initializations scheme.

To summarize, the works presented here offer routes for high-fidelity quantum operations based on the single-shot state detection. The EST allows the high-fidelity single-shot state readout of multi-electron spin qubits namely the ST_0 and hybrid qubit in a DQD. The high-fidelity quantum state detection scheme allows the real-time Hamiltonian parameter estimation which enable efficient environmental noise elimination. Also, using the quenched energy spectrum of the

Wigner molecule, coherent hybrid qubit control, and efficient control of the environmental nuclear field is enabled.

7.2 Outlook

The EST shown here is a versatile spin-to-charge conversion scheme that is applicable to any types of the host material. While the long readout time of the EST compared to other types of readout may limit the overall speed of the complex quantum computations in the semiconductor, it can certainly be beneficial at the aspect of the large signal contrast, and the robustness about the magnetic field gradient which inevitably exist in the typical QD chips.

Having demonstrated both the passive and active environmental field control by the real-time Hamiltonian estimation and the DNP, this work provides efficient routes toward the environmental noise cancellation. The bidirectional DNP with the three-electrons may allow the direct feedback control over the nuclear field for environmental field stabilization which can also contribute to the electron spin coherence extension. Moreover, the real-time Hamiltonian estimation in the Si or Ge where the nuclear spin effect is not as significant, can further reduce the charge noise and residual magnetic field noise for high-fidelity quantum operations.

As mentioned above, the hybrid qubit couples to the electric field without requiring the magnetic fields for the qubit operations. This allows the direct coupling to the superconducting circuits, where the high-kinetic inductance superconducting resonator is expected to provide ultra-strong coupling of the superconducting cavity with the qubit. The strong coupling of the hybrid qubit with the superconducting cavity would allow remote entanglement of the QD spin qubits which has been one of the goals to achieve large scale QD quantum computers.

요 약

양자 컴퓨터는 기존의 컴퓨터에 비해 특정 문제 해결들에 – 소인수분해, 외판원 문제, 검색 알고리즘 등 – 대하여 막대한 전산 속도 증대를 가져올 수 있다. 이러한 것이 가능한 이유는 양자 컴퓨터의 경우 기존 컴퓨터와 달리 완전히 양자 역학적인 성질을 갖는 큐비트 (qubit)가 그 기본 연산 단위이기 때문이다. 큐비트들은 고전계에는 존재하지 않는 양자 중첩 (superposition)과 양자 얽힘 (entanglement)을 통해 결과적으로 양자 병렬 연산을 가능케 한다. 대규모 양자 전산 시스템의 실현을 위해 초전도 회로, 이온 트랩, 그리고 반도체 양자점을 포함한 여러 구조물이 이론, 실험적으로 모두 연구되고 있다.

최근에는 초전도 큐비트를 이용한 양자 우월성 (quantum supremacy) 증명이 이루어지는 등, 양자 전산의 유망함이 보여지고 있는데, 반도체 양자점 스핀 큐비트 역시 대규모 양자 전산을 위해 활발히 연구되고 있다. 반도체 기반 스핀 큐비트의 장점은 긴 스핀 이완 (relaxation) 시간, 높은 집적도, 그리고 CMOS 공정 호환성 등을 포함한다. 이에 기반하여 최근에는 고정확 단일, 이중 큐비트 게이트 구현과 양자 에러 보정 등이 실증된 바 있고, 더 나아가, 1 K 가 넘는 온도에서의 고온 양자 제어 가능성은 반도체 양자점 스핀 큐비트의 확장성을 보여준다.

반도체 물질에 존재하는 핵 스핀의 요동은 반도체 양자점 전자 스핀 큐비트의 양자 결맞음 (coherence)에 큰 악영향을 끼친다. 하지만 그와 동시에, 핵스핀의 존재는 중심 스핀 문제 (central spin problem) 라고 불리는 단일 전자 스핀과 다수의 스핀 사이의 상호작용 탐구에 유용하게 사용될 수 있다. GaAs의 2차원 전자 층 (2DEG)은 높은 전하 이동도를 갖고, 또한 낮은 전자 유효질량을 가져 비교적 간단한 양자점 소자 공정이 가능하다고 알려져 있다. 그러나 Ga 과 As 핵들이 유한한 스핀을 가져 이러한 핵 스핀들의 요동이 전자의 스핀 결맞음을 제한 한

다는 단점이 있다. 이 학위 논문에서는 GaAs 에서의 다중 전자 스핀과 핵 스핀의 상태를 제어하는 방법에 대해 논하고, 핵 스핀 노이즈의 효과적인 제거를 통한 전자 스핀 큐비트의 결맞음 향상법을 제시한다.

챕터 1은 양자 전산의 기본과 GaAs 양자점 스핀 큐비트에 대해 간략히 소개한다. 또한 양자점 형성을 위한 dc 전하 수송 측정과 고주파 기반 실시간 전하 센싱 기법에 대하여 소개하고자 한다. 여기서 고주파 기반 실시간 전하 센싱 기법은 후술될 양자 상태의 실시간 단발 (single−shot) 측정에 필수적으로 사용되는 기술이다.

반도체 양자점은 다양한 종류의 스핀 큐비트를 연구할 수 있는 유연한 플랫폼이다. 챕터 2에서는 단일 전자 스핀 큐비트, 2개 전자 싱글렛−트리플렛 큐비트와 3개 전자 혼성 (hybrid) 큐비트를 소개한다. 각각의 큐비트의 연구 필요성과 장점들이 주로 다루어진다.

챕터 3은 에너지 의존 터널링 (Energy−selective tunneling, EST) 현상에 기반한 2개 전자 싱글렛−트리플렛 큐비트의 양자 제어에 대해 논한다. 에너지 의존 터널링은 높은 자기장 기울기 (> 85 mT) 상황에서도 고정확 (> 90%) 스핀 상태 측정을 가능케 한다. 높은 자기장 기울기는 고정확 양자 제어를 가능케 하지만, 기존의 파울리 스핀 봉쇄법 (Pauli Spin Blockade, PSB) 과는 호환되지 않는 다는 점에서 새로운 양자 상태 측정법의 개발은 더욱 정확한 양자 제어의 가능성을 열어준다. 더 나아가 챕터 4에서는 고정확 EST를 활용하여 단발 측정 기반 헤밀토니안 추정을 통한 실시간 피드백 양자 제어를 수행한다. 그 결과로 핵 스핀 노이즈가 존재하는 상황하에서 양자 결맞음이 증대될 수 있음을 보인다.

챕터 5와 챕터 6에서는 3개 전자 상태를 이용한 큐비트 제어와 핵스핀 제어법을 제시한다. 단일 양자점 내 전자간 강한 쿨롱 상호작용은 위그너 분자의 형성을 야기하며, 위그너 분자 형성의 중요한 결과 중 하나는 들뜬 상태의 에너지가 매우 작아진다는 점이다. 챕터 5 에서는 이러한 작은 에너지 차이 (바닥 상태 – 들뜬 상태 사이의)를 이용하면

통상적인 실험적 한계 내에서 3개 전자 혼성 큐비트 결맞음 제어를 할 수 있다는 것을 보이고, 해당 큐비트의 단발 측정을 수행할 수 있음을 보인다. 챕터 6 에서는 위그너 분자 상태를 이용하여 비교적 작은 자기장 조건 하에서 양방향 핵 스핀 분극 (dynamic nuclear polarization) 을 수행하여, 핵 스핀 상태를 효율적으로 제어할 수 있는 방법을 제시한다.

EST 기반의 다중 전자 스핀 과 핵 스핀 제어 방법은 GaAs 뿐만이 아니라 모든 반도체 기반 양자점 스핀 큐비트에서 사용될 수 있는 방법이다. 특히 핵 스핀의 영향이 비교적 적다고 알려진 Si 혹은 Ge 에서 해당 방법들을 적용할 경우 더욱 높은 정확도의 양자 제어가 가능할 것으로 예상 된다. 챕터 7에서는 주요 결과를 요약하고, 더욱 복잡한 양자 전산을 위해 해당 결과들이 어떻게 응용될 수 있는지 그 방향을 제시한다.